Institute of Low Temperature
and Structure Research

Polish Academy of Sciences

Study of Thermoelectric Properties of Half-Heusler Phases: *ab initio* and Machine Learning Analysis

Author:
M. Sc. Kaja Bilińska

Supervisor:
Dr. Habil. Eng. Maciej J. Winiarski

Doctoral dissertation

Wrocław Doctoral School of Institutes of Polish Academy of Sciences

Wrocław, June 2024

Acknowledgements

My heartfelt thanks to my supervisor, Maciej J. Winiarski, who supported me along the way. For years, Doctor Winiarski's profound expertise has continuously served as a great inspiration to me. I cannot envision my academic career without His presence.

I am especially grateful for the opportunity to perform calculations at Wroclaw Center for Networking and Supercomputing (Project No. 158).

I would also like to extend my appreciation to Professor Małgorzata Samsel-Czekała for her backing. Without the kindness and dedication of Professor Samsel-Czekała, the entire process of obtaining my doctorate would have been much more challenging.

I am also immensely grateful for the support and belief in me from my closest family: my Partner, Daughter, and Parents.

I dedicate this doctoral dissertation to Them.

Abstract

This doctoral dissertation is a continuation of past theoretical research related to the potential application of half-Heusler (hH) compounds as thermoelectric (TE) materials [1–3].

The high-throughput investigation with the use of Density Functional Theory (DFT) of over 150 hH phases with 18 valence electrons was performed, including two Exchange-Correlation (XC) functional parametrizations: Perdew-Burke-Ernzerhof (GGA) and modified Becke-Johnson GGA (MBJGGA) [4, 5]. Among the initial set of hH phases, over 120 systems were found to be semiconductors, whereas only 34 hH systems have been identified as novel and thermodynamically stable [6]. The detailed analysis of named systems (e.g., electronic structures) and their TE properties (including two XC functional approaches and two types of conductivity regimes) is undertaken in this doctoral dissertation.

The *ab initio* research has been supported through Machine Learning (ML) methods. The analysis and predictions were done for six different targets, including band gaps [7] and TE performance (TE Power Factor for GGA parametrization and p-type regime) [8]. The chemical trends and potential predictors in all the cases were examined in detail.

The overall findings from DFT and ML analysis conducted here on the hH phases infer novel hH phases as candidates for TE materials and some insights into the crucial predictors for their favorable TE performance.

Abstrakt

Niniejsza rozprawa doktorska stanowi kontynuację badań prowadzonych w przeszłości nad potencjalnym zastosowaniem związków typu pół-Heulser (hH) jako materiałów termoelektrycznych (TE) [1–3].

Przeprowadzone zostały badania dużej skali z wykorzystaniem Teorii Funkcjonału Gęstości (DFT) dla ponad 150 faz hH z 18 elektronami walencyjnymi; uwzględnione zostały dwie parametryzacje funkcjonału korelacyjno-wymiennego (XC): Perdew-Burke-Ernzerhof (GGA) oraz zmodyfikowany potencjał Becke-Johnson GGA (MBJGGA) [4, 5]. Spośród początkowego zbioru badanych związków hH, ponad 120 układów okazało się mieć charakter półprzewodnikowy, przy czym tylko 34 zostały zakwalifikowane jako nowe oraz termodynamicznie stabilne [6]. Szczegółowa analiza dla tych układów (np. struktury elektronowe) oraz ich właściwości TE (w tym uwzględniająca dwa funkcjonały XC oraz dwa reżimy przewodnictwa) została zrealizowana w niniejszej rozprawie doktorskiej.

Obliczenia ab initio zostały uzupełnione metodami Uczenia Maszynowego (ML). Analiza ML oraz predykcje zrealizowane zostały dla sześciu wielkości, w tym przerwy energetycznej [7] oraz wydajności TE (termoelektryczny współczynnik mocy PF dla parametryzacji GGA w reżimie typu p) [8]. Trendy chemiczne oraz potencjalne predyktory zostały rozpatrzone i szczegółowo zbadane.

Ogólne wyniki uzyskane w ramach analizy DFT i ML dla rozważanych faz hH wskazują nowych kandydatów na materiały TE, a ponadto umożliwiają wgląd w kluczowe predyktory determinujące korzystne właściwości TE.

Scientific Publications:

- Bilińska, K., Winiarski, M. J. Search for semiconducting materials among 18-electron half-Heusler alloys. *Solid State Commun.* **2023** *365*, 115133 [4];
- Bilińska, K., Winiarski, M. J. A theoretical investigation of 18-electron half-Heusler tellurides in terms of potential thermoelectric value. *EPJ B* **2023** *96(10)*, 131 [5];
- Bilińska, K., Winiarski, M. J. High-Throughput Exploration of Half-Heusler Phases for Thermoelectric Applications. *Crystals* **2023** *13(9)*, 1378 [6];
- Bilińska, K., Winiarski, M. J. Machine Learning-Based Predictions for Half-Heusler Phases. *Inorganics* **2023** *12(1)*, 5 [7];
- Bilińska, K., Winiarski, M. J. Machine Learning-Based Predictions of Power Factor for Half-Heusler Phases. *Crystals* **2024** *14(4)*, 354 [8].

Conference Posters:

- 49th International School and Conference on the Physics of Semiconductors "Jaszowiec 2021", online conference held 1-10 September 2021 in Szczyrk. *A search for potentially valuable thermoelectric materials over 18-electron half-Heusler alloys* Bilińska, K., Winiarski, M. J. - **poster K. Bilińska**;
- 51st International School and Conference on the Physics of Semiconductors "Jaszowiec 2023", conference held 17-23 June 2023 in Szczyrk. *Novel Te-bearing half-Heusler phases and their potential thermoelectric performance* Bilińska, K., Winiarski, M. J. - **poster K. Bilińska**;
- Advanced Technologies and Materials (ATAM) and Materials Science Conference on Advanced Functional Materials (MASCA) 2024, conference held 5-7 June 2024 in Wrocław. *Machine Learning for half-Heusler Phases: From Lattice Parameter to Thermoelectric Performance* Bilińska, K., Winiarski, M. J. - **poster K. Bilińska** (planned).

Abbreviations:

- BTE - Boltzmann Transport Equation
- CBM - Conduction Band Minimum
- DFT - Density Functional Theory
- DP - Deformation Potential
- FP-LAPW - Full-Potential Linearized Augmented Plane Wave
- GGA - Generalized Gradient Approximation
- hH - half-Heusler
- LOO - Leave One Out
- L(S)DA - Local (Spin) Density Approximation
- MBJ - modified Becke-Johnson (MBJGGA here)
- ML - Machine Learning
- PF - Power Factor
- RMSE - Root Mean Squared Error
- SVR - Support Vector Regression
- TE - Thermoelectric
- VBM - Valence Band Maximum
- VEC - Valence Electron Count
- XC - Exchange-Correlation
- ZT - Figure of Merit

Contents

Chapter 1

Theoretical Introduction

1.1 Subject of the study

1.1.1 Motivation and aim of the investigation

The research conducted for the purpose of this Ph.D. dissertation was to examine over 150 half-Heusler (hH) phases in order to provide potentially valuable thermoelectric (TE) materials. This idea arose from the TE properties of hH phases investigated in the past [1–3]. The whole process was complex, requiring various calculations, from *ab initio* to Machine Learning (ML). The aim of this investigation was to list the hH systems with the highest probability of being stable and potentially thermoelectrically valuable. This kind of theoretical investigation may encourage experimental research on the particular phases without the need to try to synthesize all over 150 hH compounds.

In order to provide the most reasonable results, multiple models and conditions were implemented and fulfilled, e.g., the stability criteria (Chapter 1.2.1), realistic relaxation time approximation (Chapter 1.4.2), and two different Exchange-Correlation Functionals (XCF) (Chapters 1.3.8, 2.2). Therefore, the final number of potentially valuable TE systems was drastically reduced. However, one shall find them the most promising, especially due to the accordance between the results and the existing experimental data (the particular examples are discussed in the following chapters).

Such a comprehensive approach resulted in a list of 34 stable systems (32 from the origin list and two additional Te-bearing phases) with TE properties investigated and even more systems with ML relations and predictions analyzed. Crucial results were summed up in the following papers:

- *Search for semiconducting materials among 18-electron half-Heusler alloys* [4];

- *A theoretical investigation of 18-electron half-Heusler tellurides in terms of potential thermoelectric value* [5];
- *High-throughput exploration of half-Heusler phases for thermoelectric applications* [6];
- *Machine Learning-Based Predictions for Half-Heusler Phases* [7];
- *Machine Learning-Based Predictions of Power Factor for Half-Heusler Phases* [8].

Calculations were performed in the Wroclaw Center for Networking and Supercomputing (Project No. 158).

1.1.2 Investigation process

The whole computational process (Figure 1.1) began with the proposal of the initial list of hH systems to be investigated (153 18-electron cubic hH phases). For all the systems, lattice parameters were predicted with the use of Support Vector Regression (SVR). Predicted lattice parameters were used as the input for the *ab initio* calculations. After optimalization of the unit cell volume, 153 hH systems with equilibrium lattice parameters were investigated. Elastic constants were calculated within the perturbation theory. For the calculations, two Exchange-Correlation (XC) parameterizations were used: Generalized Gradient Approximation (GGA) and modified Becke-Johnson, meta-GGA (MBJGGA). The electronic structures were analyzed, and the band gaps were revealed. Based on the band structures, the effective mass of the carriers in the vicinities of Valence Band Maximum (VBM), for p-type carriers, and Conduction Band Minimum (CBM), for n-type carriers, were calculated. Next, the Deformation Potential (DP) theory was used, which required additional calculations for the deformed unit cell. Based on the effective mass, DP, and elastic constants, the relaxation time of the carriers was approximated.

In order to carry out TE analysis of the systems considered, dense-sampled DFT output was required. This stage of the investigation, which was highly time- and resource-consuming, was performed only on a limited subset of hH systems. The criterion limiting the origin set of hH compounds was mechanical and thermodynamical stability (Chapter 1.2.1).

After thermoelectric calculations leading the TE Power Factor (PF) results, the lattice thermal conductivity κ_L was calculated. Combining PF and κ_L resulted in the Figure of Merit (ZT).

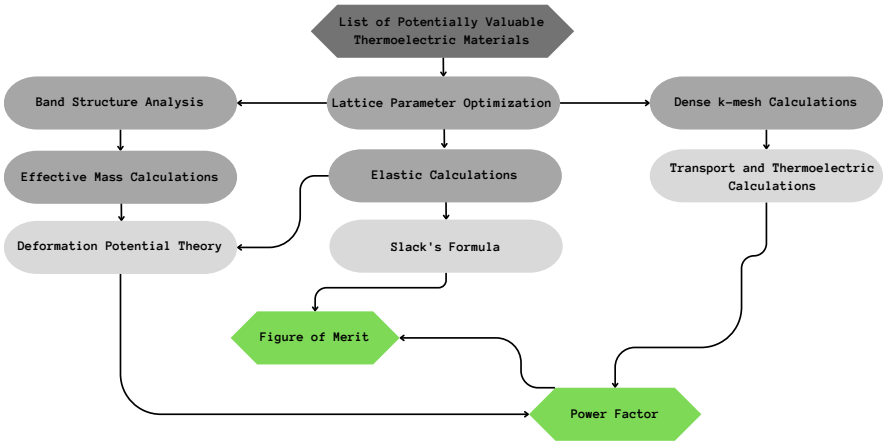

FIGURE 1.1: Flow chart with the investigation process, excluding ML analysis.

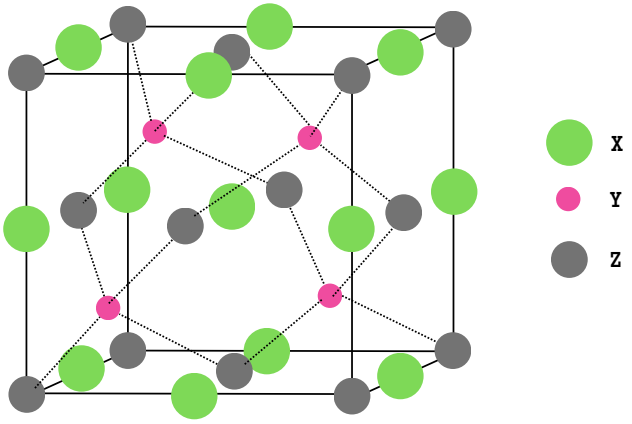

FIGURE 1.2: The hH structure with X, Y, and Z ions marked [9].

All the parameters were investigated for both electrons and holes, but also for two different types of XC functionals.

1.2 Half-Heusler Phases

Heusler compounds were discovered and reported by Friedrich Heusler in 1903. In general, this type of system is formed by three ions: X, Y, Z, where X, Y are the transition metals and Z is a main group element. Originally, these phases would crystallize in the face-centered cubic (FCC) symmetry; however, there are numerous Heusler systems with lower symmetry (e.g., orthorhombic).

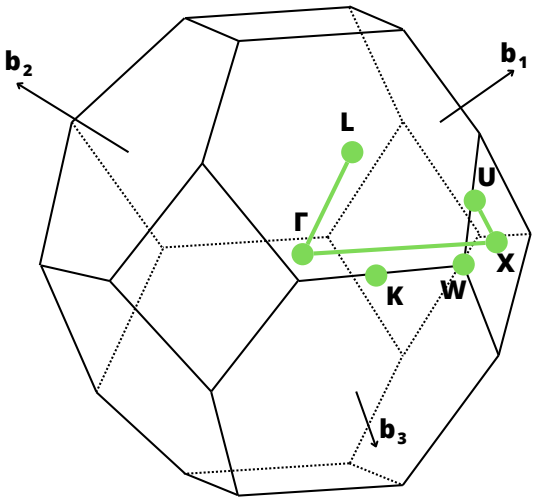

FIGURE 1.3: The first Brillouin zone for FCC systems [13].

Depending on the stoichiometry of the phase, different members of the Heusler family shall be distinguished, e.g., full-Heusler (X_2YZ), half-Heusler (XYZ) (Figure 1.2), or double half-Heusler ($X_2YY'Z_2$). The diversity of the elemental components and the space distribution of ions provide multiple possible systems with various properties. In fact, the unwavering interest in the Heusler phases is determined by the variety of possibilities of application, from optoelectronics [10, 11] to ferromagnets [12].

In this work, the area of interest is limited to the half-Heusler (hH) systems only. The high symmetry of the space group $F\bar{4}3m$ adopted by hH phases results in relatively low cost of the calculations. The occupation of Wyckoff positions ($X(0,\ 0,\ 0)$, $Y(1/4,\ 1/4,\ 1/4)$, and $Z(1/2,\ 1/2,\ 1/2)$) are determined by the electronegativity, whereas Z is the less electropositive (anion). The hH $F\bar{4}3m$ structure is presented in Figure 1.2.

In order to provide the highest probability of the synthesizability of the systems investigated, the comprehensive stability analysis was performed (Chapter 1.2.1).

The First Brillouin Zone (IBZ) of the FCC hH systems regarded has the form presented in Figure 1.3. The band structure analysis of the hH systems considered in this research was performed in the $L\Gamma XU$ directions.

1.2.1 Stability

Multiple possibilities of the hH ternary systems regarded are limited by the stability and, therefore, synthesizability expected. In order to provide the most probable stable phases

only, the criteria presented below were applied.

1.2.1.1 18 valence electrons

The stability issue for hH phases is often considered based on the Valence Electron Count (VEC), which is the number of valence electrons in the phases. It is expected that due to the hybridization of d bands resulting in the stabilization of the electronic system, hH systems with particular VEC values are more stable than similar systems with different VEC values [14]. Compounds with a VEC different from 18 provide systems with antibonding states unfilled. In the literature, one can found homogeneous systems with VEC equals 18 [14–18] but also heterogeneous systems with two different VEC values, 17 and 19 [19]. Also, some 19-electron systems were investigated [20]. However, in general, the 18-electron systems with all-bounding electronic states (a fully filled valence shell for a transition metal) are expected to be stable.

1.2.1.2 Born mechanical stability

The elemental condition of the mechanical stability of the systems was considered according to the Born's stability criterion for the cubic systems [21, 22]:

$$C_{11} + 2C_{12} > 0, \quad C_{11} - C_{12} > 0, \quad C_{44} > 0$$

where C_{11}, C_{12}, C_{44} are the elastic constants from the elasticity tensor in the particular directions in the crystal.

All the systems considered in this research were found to be mechanically stable due to this criterion.

1.2.1.3 Thermodynamic stability

In order to determine the stability of the phase regarded, the *Open Quantum Material Database* (OQMD) was employed [23, 24]. The criterion of the so-called hull distance E_{HD} was chosen as the determinant of the system's stability (Figure 1.4). E_{HD} is an energy difference between the formation energies for the convex hull among the different concentration ratios of the elements constituent. If the phase regarded lies on the convex hull, it is stable; if it is off the convex hull, it is unstable. In Figure 1.4, the comparison of the stable phase P and unstable phase P' are presented. In case of the stable phase P, it lies on the convex hull (A-P1-P-B) what determines stability equals 0 eV/atom. On

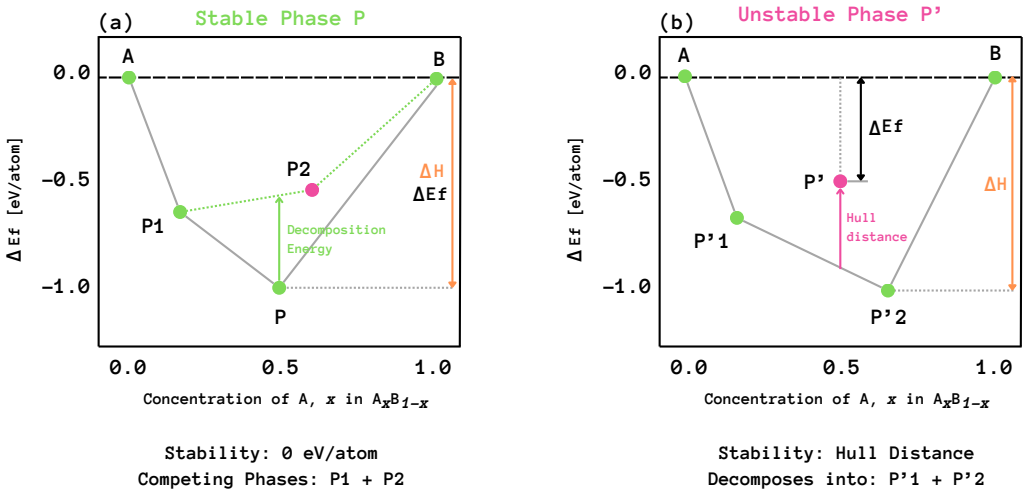

FIGURE 1.4: The OQMD-based diagrams of the hull distance interpretation as the mechanical stability determinant, where: ΔE_f is formation energy (eV/atom) and ΔH - hull energy (eV/atom). In (a), the stable phase P is presented (lies on convex hull A-P1-P-B) [25].

contrary, the unstable phase P' is off the convex hull; the distance from the convex hull (E_{HD} defined as the difference between the formation energy ΔE_f of the phase P' and hull energy ΔH at this composition) describes the of the stability.

The OQMD as the phase stability determinant is widely implemented in different fields of science, including ML support for the discovery of novel compounds [26, 27].

However, the possibility of synthesis of some phases that are in the vicinity of the convex hull but not directly on it was proved [28]. There are some reports of incongruent OQMD unstable predictions opposite to experimental reports on synthesis. OQMD, as every powerful and enormous tool, has its accuracy and limitations [29]. Therefore, based on the conclusions by Aykol *et al.*, the expected range of the hull distance for highly likely stable systems was extended to 0.1 eV (Chapter 4).

Finally, for the purpose of this work, it was postulated that the limitation of VEC to eighteen, fulfillment of the Born's stability criterion and E_{HD} determinant would be sufficient for the stability assumption of the particular phase.

The lattice dynamics of the systems were not studied.

1.3 Ab initio methods

Ab initio methods are the process of theoretical investigation of atomic systems. For hydrogen molecule one can solve the non-relativistic Schrödinger Equation (SE), however, for more complex atomic models, more sophisticated methods are required.

1.3.1 Single atom model

The single-atom model (hydrogen atom: one ion with one orbiting electron) is an introduction to the solid-state theory, whereas it is still possible to be solved exactly [30]. The SE of the single particle in the spheric potential of the ion is as follows:

$$\left[-\frac{\hbar^2}{2m}\nabla^2 + V(\mathbf{r})\right]\Psi(\mathbf{r}) = E\Psi(\mathbf{r}) \tag{1.1}$$

where V is an ion potential, m is a particle mass. Using the polar coordinates, Hamiltonian regarded can be written as:

$$H = -\frac{\hbar^2}{2m}\frac{1}{r^2}\left[\frac{\partial}{\partial r}r^2\frac{\partial}{\partial r} - \frac{\mathbf{M}^2}{\hbar^2}\right] \tag{1.2}$$

where $\mathbf{M}$ is the ion mass. Finally, Equation 1.1 can be written down as follows:

$$\left[-\frac{\hbar^2}{2m}\frac{1}{r^2}\left(\frac{\partial}{\partial r}r^2\,\frac{\partial}{\partial r} - \frac{\mathbf{M}^2}{\hbar^2}\right) + V(\mathbf{r}) - E\right]\Psi(\mathbf{r},\theta,\phi) = 0 \tag{1.3}$$

1.3.2 Multiple atom model

The more elements of the system are considered, the more complex the quantum approach becomes. At some point, the solution of SE is impossible, and different methods are required.

For the many-body system, the Hamiltonian is given as follows:

$$H = \sum_\alpha \frac{P_\alpha^2}{2M_\alpha} + \sum_i \frac{p_i^2}{2m} + \frac{1}{2}\sum_{i,j}\frac{1}{|\mathbf{r}_i - \mathbf{r}_j|} - \sum_{i,\alpha}\frac{Z_\alpha}{|\mathbf{r}_i - \mathbf{R}_\alpha|} + \frac{1}{2}\sum_{\alpha,\beta}\frac{Z_\alpha, Z_\beta}{|\mathbf{R}_\alpha - \mathbf{R}_\beta|} \tag{1.4}$$

where: Z - atomic number, $\mathbf{r}$ - distance between the electrons and ions, $\mathbf{R}$ - distance between the ions.

1.3.2.1 Adiabatic Born-Oppenheimer approximation

For the description of condensed matter systems, the Born-Oppenheimer approximation is applied [30]. This adiabatic statement postulates the significant difference between masses and mobilities of the carriers and ions. Therefore, the approximation of steady ions (potential constant as a function of time) and moving carriers is proposed. This approach excludes the phonons, however, in low temperatures, when the phonon vibrations are small, this approximation is adequate. The higher the temperature, the greater the deviation from the actual expected behavior of the crystal lattice.

After the implementation of the adiabatic Born-Oppenheimer approximation, Equation 1.4 of the N element system is given as follows:

$$H = \sum_i \left[-\frac{\hbar^2}{2m}\Delta_{r_i} + \sum_\alpha V_{ej}(\mathbf{r}_i, \mathbf{R}_\alpha) \right] + \frac{1}{2}\sum_i \sum_{j \neq i} \frac{e^2}{|\mathbf{r}_i - \mathbf{r}_j|} \tag{1.5}$$

Still, more approximations and models are required for an effective multiple-body system description.

1.3.3 Density Functional Theory

The basic postulate about the solid state is the simplified model of the realistic alloy. The ions are located periodically in the space, with free electrons distributed between them. The amount of ionic cores and electrons in the typical crystal requires more complex than the previously presented methods for small systems.

In the 1960s, in order to provide the accurate, but at the same time calculable solid-state model, the Density Functional Theory (DFT) was created. The main idea behind DFT is abandoning the single carrier analysis approach and developing the density of the carriers distributed between the atomic cores instead.

In Figure 1.5 there is the intuition behind DFT depicted [31]. As one can perceive, DFT modifies the typical interpretation of the system to be solved with the use of SE. In quantum mechanics, the interactions between electrons within the external, periodic potential determined by the core atoms are considered. In the formally equivalent Kohn-Sham system, the interactions of the particles are neglected *per se*. However, the realization of the lattice potential changes into the so-called effective potential, which does regard the neglected interaction part between particles. If the function describes the effective potential in which non-interactive Kohn-Sham particles are, this model is equivalent to the classical Schrödinger system with interacting particles in the external potential.

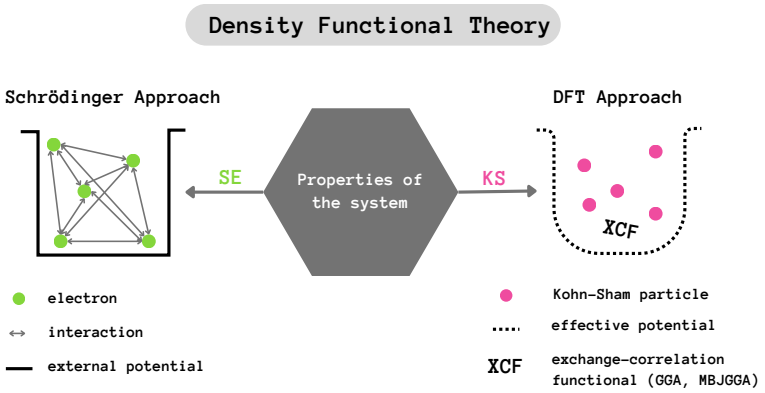

FIGURE 1.5: The illustration of the idea behind Density Functional Theory [31].

In the DFT methods, the N-element system is described through the particle density:

$$\rho(\mathbf{r}) = N \int d^3r_2 \int d^3r_3 ... \int d^3r_N \Psi * (\mathbf{r}, \mathbf{r}_2, ..., \mathbf{r}_N)\Psi(\mathbf{r}, \mathbf{r}_2, ..., \mathbf{r}_N), \tag{1.6}$$

which is normalized to the number of particles: $\int d^3\rho(\mathbf{r}) = N$. When the $\rho(\mathbf{r})$ is known, the explicit norm of the wave function $\Psi(\mathbf{r}, \mathbf{r}_2, ..., \mathbf{r}_N)$ can be calculated. In the DFT approach, all the state operators are the functionals of charge density. Therefore, instead of the single-electron ground state calculation, the ground state of the electron density (as a function of the 3D space vector) is provided [32].

Due to the invertibility of Equation 1.6, the Self-Consistent Field method can be applied (more: Chapter 1.3.6).

The essential component of the Kohn-Sham DFT model is an Exchange-Correlation (XC) functional, participating in the final effective potential form. The role of XC functional and the different postulates it formulates are discussed in Chapter 1.3.7.

1.3.3.1 Hohenberg-Kohn Theorems

DFT derives its essence from the underlying two theorems, revealed by Hohenberg and Kohn in 1964 [33]. Hohenberg and Kohn provided the insight that the ground states of the multiple-body systems in the external potential can be interpreted as the charge density functionals.

The first Hohenberg-Kohn Theorem

For a non-degenerate ground state, the energy of the system

is uniquely determined by its electron density.

The first theorem does not provide the exact formula for the electron density functional but only postulates its existence. The different interpretations of this theory reflect the direct relationship between the external potential and the electron density. This theorem can be extended to the degenerated states in the system.

The apagogic proof of the first theorem is presented below.

Let us postulate that by the same density of the ground state (ρ) the two different external potentials (V_1, V_2) and corresponding Hamiltonians ($\hat{H}_1$, $\hat{H}_2$) and wave functions (Ψ_1, Ψ_2) are described.

With the use of the variation principle [34], the $\epsilon[\Psi]$ (where Ψ is normalized and depends on the same variables as the wave function of the system characterized by $\hat{H}$) can be defined as:

$$\epsilon[\Psi] = \frac{\langle\Psi|\hat{H}|\Psi\rangle}{\langle\Psi|\Psi\rangle} \tag{1.7}$$

and does realize the following conditions:

- $\epsilon \geq E_0$, where E_0, where E_0 is the smallest $\hat{H}$ value (energy of the ground state);
- $\epsilon = E_0$ if and only if Ψ is a wave function of the ground state.

From the above variation principle, there is a resulting relationship:

$$E_1 < \langle\Psi_2|\hat{H}_1|\Psi_2\rangle = \langle\Psi_2|\hat{H}_2|\Psi_2\rangle + \langle\Psi_2|\hat{H}_1 - \hat{H}_2|\Psi_2\rangle = E_2 + \int \left(V_1(\mathbf{r}) - V_2(\mathbf{r})\right)\rho(\mathbf{r})d^3r$$

Analogically:

$$E_2 < \langle\Psi_1|\hat{H}_2|\Psi_1\rangle = E_1 + \int \left(V_2(\mathbf{r}) - V_1(\mathbf{r})\right)\rho(\mathbf{r})d^3r$$

The juxtaposition of the above equations leads to a contradiction:

$$E_1 + E_2 < E_1 + E_2$$

which proves the falsehood of the initial statement and, therefore, demonstrates the correctness of the first Hohenberg-Kohn theorem. Q.E.D.

The second Hohenberg-Kohn Theorem

The ground state of the system is a state for which the energy functional is minimized.

1.3.3.2 Kohn-Sham Method

The Kohn and Sham method [35] is the most common practical realization of the Hohenberg-Kohn methods.

Following the Kohn-Sham model (Figure 1.5), the Hamiltonian of the system can be described as:

$$H_{KS} = -\frac{1}{2}\sum_{i}^{N}\nabla_i^2 + V_{KS}(\mathbf{r}), \tag{1.8}$$

where V_{KS} is an effective potential for Kohn-Sham particles. The carrier density $\rho(\mathbf{r})$ calculations is done for the independent N^σ Kohn-Sham orbitals ψ^σ:

$$\rho(\mathbf{r}) = \sum_{\sigma}\rho(\mathbf{r},\sigma) = \sum_{\sigma}\sum_{i=1}^{N_\sigma}|\psi_i^\sigma(\mathbf{r})|^2 \tag{1.9}$$

The complete energy of the systems consisting of N^σ Kohn-Sham orbitals is the sum of the following components:

- kinetic energy of the particles;
- potential energy of the ions;
- energy of the Coulomb interaction between particles (Hartree energy for correlations between electrons);
- XC energy of the particles.

The final form of the total energy is as follows:

$$E_{KS}[\rho] = \frac{1}{2}\sum_{\sigma}\sum_{i=1}^{N}|\nabla\psi_i|^2 + \int d^3V(\mathbf{r})\rho(\mathbf{r}) + \frac{1}{2}\int d^3r d^3r' \frac{\rho(\mathbf{r})\rho(\mathbf{r'})}{\mathbf{r}-\mathbf{r'}} + E_{XC}[\rho] \tag{1.10}$$

With the use of calculus of variation, the Kohn-Sham total energy functional (Equation 1.10) can be transformed to the Kohn-Sham equations:

$$\left[-\frac{1}{2}\nabla^2 + V(\mathbf{r}) + V_{Hartree}(\mathbf{r}) + V_{XC}^{\sigma}(\mathbf{r}) - \epsilon_i^{\sigma}\right]\psi_i^{\sigma}(\mathbf{r}) = 0. \tag{1.11}$$

Finally, in order to provide a description of the multiple particle quantum model, the Self-Consistent Field (SCF) (Chapter 1.3.6) method for Kohn-Sham equations (Equations 1.11) is implemented.

1.3.4 Full-Potential Linearized Augmented Plane Wave

As another approximation in the many body systems, the Full-Potential Linearized Augmented Plane Wave method (FP-LAPW) is applied [36, 37]. Following it, the space in the crystal is divided into two parts: the vicinity of the ion (MT - Muffin-Tin) and the region between ions (IR - Interstitial Region). Carriers in the first region, limited by so-called *cut-off energy*, are described with the spherical harmonics. Carriers outside the nearest vicinities of the ions are described with plane waves. This kind of approximation greatly decreases the complexity of the calculations to be performed. The visualization of this methodology is presented in Figure 1.6.

This approximation is reasonable due to the assumption that the only valence electron part takes part in the creation of the chemical bonds between ions in the periodic solid-state structure. Therefore, in the Muffin-Tin (MT) region, Figure 1.6 (b), there are only the core electrons, while the IR region is characterized by the presence of only the valence electrons [38].

Let us mark the radius of the MT sphere with R_t, where t is an index of the sfere in the periodic potential. The wave function describing the state of the system is given as the linear combination of the radial functions and the spherical harmonics, which can be written as shown:

$$\phi_{\mathbf{k}_n} = \sum_{l,k}\left[A_{lm,\mathbf{k}_n}u_l(r,E_l) + B_{lm,\mathbf{k}_n}\dot{\mathbf{u}}_l(r,E_l)\right]Y_{lm}(\hat{\mathbf{r}}), \tag{1.12}$$

where: $u_l(r,E_l)$ is a general radial SE solution for energy E_l; $\dot{\mathbf{u}}_l(r,E_l)$ is the derivative of the energy of u_l (at the same energy E_l). $u_l(r,E_l)$ and $\dot{u}_l(r,E_l)$ are obtained by the numerical integration of SE on the radial mesh inside the t MT sphere. Due to the linear combination of $u_l(r,E_l)$ and $\dot{\mathbf{u}}_l(r,E_l)$, the energy dependence of the radial function is

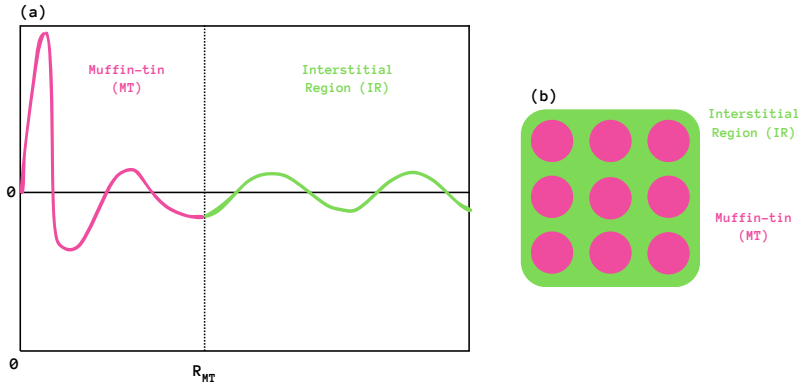

FIGURE 1.6: The visualization of the full-potential method for the nearest vicinity of the ions and the Interstitial Region (IR). In (a), there are wave functions describing the particular region depicted, while in (b), the schematical muffin-tin region organization is depicted [38].

also linear. The coefficients A_{lm} and B_{lm} are the functions of k_n and are required by the matching of the basis functions in the IR [39].

The implementation of this approach findings the Linearized Augmented Plane Wave (LAPW) method and allows very accurate numerical calculation of the electronic functions in the plane wave base with the use of Bloch theory for the periodic crystal lattice.

Bloch theory allows the presentation of the wave functions of the carriers in the periodical potential as:

$$\psi_k(\mathbf{r}) = u_k(\mathbf{r})e^{ik\mathbf{r}} \tag{1.13}$$

where k is a wave vector, $u_k(\mathbf{r})$ characterizes the periodicity of the lattice structure: $u_k(\mathbf{r}) = u_k(\mathbf{r} + \mathbf{R})$, where $\mathbf{R}$ is a crystal lattice vector.

The different interpretation of Bloch theory postulates that every degenerated solution for the wave function in the periodic solid-state system can be transformed into the linear combination of the solutions connected to the same energy (with the same conditions given) but with possible different $\mathbf{k}$ [40].

1.3.5 Projector Augmented Wave

Within VASP software, the implementation of the Projector Augmented Wave (PAW) is carried out. PAW is one of various techniques used in *ab initio* calculations, characterized by relatively low computational cost compared to, e.g., FP-LAPW. The reason for the

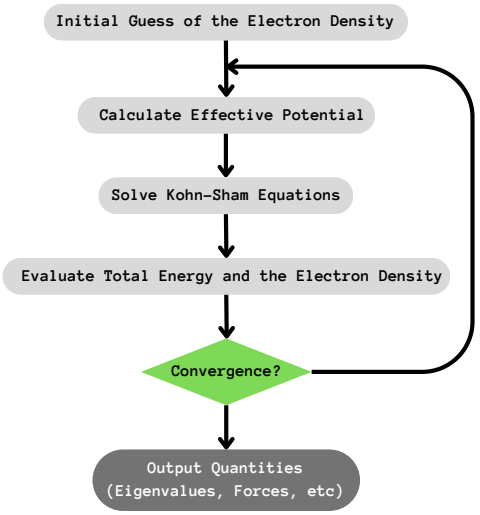

FIGURE 1.7: Flow chart of the Self Consistent Field method [42].

relatively greater efficiency of PAW is due to the used approximation of the complex system, i.e., the rapidly oscillating wavefunctions of the core electrons. The smoothing of wavefunctions in the MT region (core electrons are 'frozen') enables the description of the wavefunctions in the IR region with fewer Fourier modes used. This approximation is reasonable and computationally convenient [41].

1.3.6 Self Consistent Field Method

The solution of Kohn-Sham equations (Equations 1.11) requires the self-consistent iterative method of the calculations, i.e., SCF method. This approach results from the lack of complete input data to solve Kohn-Sham equations; both electron density and the effective potential formula (external potential from ions and XC potential) are unknown. Only the repetitive procedure of postulating the density value and investigating the convergence of the model in the next iterative steps may be effective in this case. What is worth mentioning here is the fact that Hohenberg, Kohn, and Sham theory, even though created in 1960., had to wait for the machine support solution due to the iterative procedure of the method.

The convergence in SCF is understood as the minimalization until the *epsilon* the difference of selected parameters in the following iterative steps. Parameters determining the convergence of the system may be e.g., the energy and charge of the whole system considered.

The practical implementation of the SCF method essentially amounts to the initial electron density guess and, after this, further calculations of the XC potential. With the

postulated formula of the XC functional, Kohn-Sham equations are calculated, and the evaluation of the electron density (or charge, depending on the software used) and total energy is performed. In fact, it is the difference in a particular parameter (e.g., total energy or electron density) in the next iterative steps that determines the convergence of the model. If the difference of the verifying parameters in the next iterative steps is small enough (arbitrary chosen *epsilon*), the SCF procedure finishes successfully, returning the final parameters of the system converged (e.g., eigenvalues, forces) [42].

The whole SCF method for Kohn-Sham equations is depicted in Figure 1.7.

1.3.7 Exchange and Correlation

A crucial element of the Kohn-Sham model is an exchange-correlation (XC) hole. The phenomenon of the XC hole is attributed to the interplay of the phenomena of Coulomb repulsion and the Pauli exclusion principle. XC holes can be modeled in various ways, e.g., Hood *et al.* provided the realization of this issue with the Monte Carlo methods combined with DFT [43]; the results are very satisfying and encouraging.

In order to provide a mathematical description of the exchange-correlation holes neglected in the Kohn-Sham model, the XC functionals are implemented. Depending on the XC functional used, the electronic structure, and therefore all the further analysis, may strongly vary. This fact is due to the different approximations and postulates employed.

1.3.8 Exchange-Correlation Functionals

- **Local (Spin) Density Approximation**

  The Local Density Approximation (LDA) and Local Spin Density Approximation (LSDA) depend on the electron density value at a particular point in the space. Such a model is simple in comparison to the more sophisticated XC functionals; however, it still, in some circumstances, provides good results for realistic systems [44]. The XC energy formula for LDA is given as follows:

  $$E_{XC}^{LDA}[\rho] = \int \epsilon_{XC}(\rho(\mathbf{r}))\rho(\mathbf{r})d\mathbf{r}$$

  where ϵ_{XC} is the XC energy per particle for the homogenous electron gas, and by ρ the corresponding electron density is given.

  While taking into consideration spin, the XC energy formula of the Local Spin Density Approximation (LSDA) has the following form:

$$E_{XC}^{LSDA}[\rho_\alpha, \rho_\beta] = \int \epsilon_{XC}(\rho_\alpha, \rho_\beta)\rho(\mathbf{r})d\mathbf{r}$$

whereas ρ_α and ρ_β are densities for two spins regarded with the sum of the densities conserved: $\rho_\alpha + \rho_\beta = \rho$ [45].

- **Generalized Gradient Approximation**

  The Generalized Gradient Approximation (GGA) [46] is defined as XC functional regarding the gradient differences of the carrier density. The XC energy taking into consideration spin is given as follows:

$$E_{XC}^{GGA}[\rho_\alpha, \rho_\beta] = \int \epsilon_{XC}(\rho_\alpha, \rho_\beta, \nabla\rho_\alpha, \nabla\rho_\beta)\rho(\mathbf{r})d\mathbf{r}$$

  This XC functional was chosen as the base for all calculations for this research.

- **Modified Becke-Johnson Potential**

  The second XC functional used in this work was based on the modified Becke-Johnson potential (MBJ), meta-GGA approach of Tran and Blaha (MBJGGA) [47]. It is combined with the correlation term from LDA/GGA.

  The reason for this functional choice was the undervaluation of the band gap by GGA. MBJ (MBJGGA) functional is preferred for the semiconducting materials due to the more realistic results of electronic structure. The form of potential is given as follows:

$$V_{x,\sigma}^{MBJ}(\mathbf{r}) = cV_{x,\sigma}^{BR}(\mathbf{r}) + (3c-2)\frac{1}{\pi}\frac{\sqrt{5}}{12}\frac{\sqrt{2t_\sigma(\mathbf{r})}}{\sigma_\sigma(\mathbf{r})}$$

  where $V_{x,\sigma}^{MBJ}$ is a Becke-Roussel potential [48], t_σ is the kinetic energy density, and σ_σ is the carrier density. The constant c is defined as the α and β [49] functions:

$$c = \alpha + \left(\beta\frac{1}{V_{cell}}\int\frac{|\nabla\sigma(\mathbf{r})|}{\sigma(\mathbf{r})}d\mathbf{r}\right)^{1/2}$$

  where the α and β are arbitrary parameters.

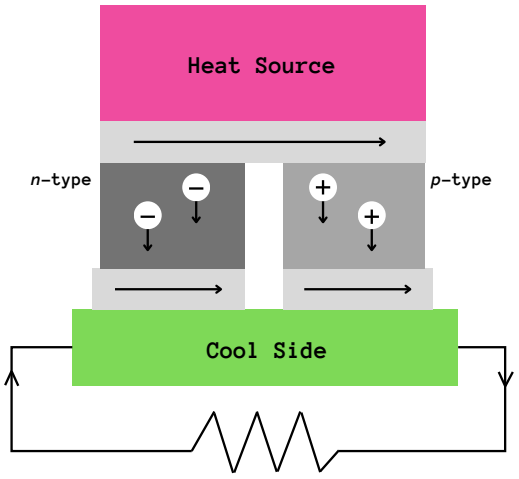

FIGURE 1.8: Ilustrative flow of the charge among the Thermoelectric Material when temperature gradient applied [125].

1.4 Thermoelectric Materials

Today, thermoelectric (TE) materials are of high interest due to the various ways of their implementation in agreement with ecological and heat-pollution philosophies. The idea behind TE materials is to convert the heat to be wasted into electrical current, which can be reused [125]. Graphics presenting the flow of the charge with the gradient temperature applied are presented in Figure 1.8.

In order to provide a quantitative value of the TE material, the TE Power Factor (PF):

$$PF = S^2\sigma$$

or Figure of Merit (ZT) are used:

$$ZT = \frac{PF}{\kappa_e + \kappa_l}T,$$

where: S - Seebeck coefficient, σ - electrical conductivity, κ_e - electronic thermal conductivity, and κ_l - lattice thermal conductivity.

Seebeck effect *If there is a gradient of temperature in the conducting material and at the same time there is no electric current applied to the material, then there is a*

constant electrostatic potential between low- and high-temperature regions of the material.

The justification of the Seebeck effect is due to the fact that after the creation of the temperature gradient through the material, electrons from the warmer part gain velocity in the direction of the lower temperature. The quantitative Seebeck coefficient is also determined by the band structure and the Density of States (DOS) - the more bands, the more carriers to potentially participate in Seebeck effect. The movement of electrons and carriers results in the generation of electric potential and electric current.

The respective *electric pole*, directed opposite to the temperature gradient, can be described as shown below:

$$\mathbf{E} = Q\nabla T, \tag{1.14}$$

where Q is a thermoelectric power connected with the Seebeck coefficient [50].

The application of the Seebeck effect provides insight into reusing the heat to be generated and transforming it into an electrical current. Such an approach results in lower heat losses and, therefore, lower energy losses. An example of the use of the natural temperature gradient can be implants, smart glasses or watches, conducting polymers, TE modules in hybrid car engines and many more [51]. Such a TE implementation is especially useful if the heat losses are great and inevitable, e.g., in power plants.

However, one shall note that the difficulty in obtaining the high TE performance results from the fact that low σ is in general connected with high S and low κ in simple semiconductors.

1.4.1 Boltzmann Theory

Boltzmann theory is a model to describe macroscopic parameters of the system (electrical conductivity, Seebeck coefficient, mobility of the carriers) with the use of the microscopic parameters [52, 53].

1.4.1.1 Drude Model

Boltzmann theory is built upon the groundwork laid by Drude in 1900, which is a model of conductivity in a crystal. In the Drude model, the classical kinetic gas theory is applied

to the model of the free electrons. This model can also be used for the description of electron or hole-like carriers in semiconductors.

The fundamental assumptions of the Drude model are:

- electrons are the identical stiff balls, which move in a straight-line motion between the negligibly short collisions;
- during collisions, the only forces acting on the particles are those resulting from the collision;
- all the interactions electron-ion and electron-electron, but the very fast collisions are neglected;
- scattering of the electrons on the electrons is much less significant compared to the electron scattering on ions;
- electrons do collide with the atomic cores with the probability given by the revised value of the relaxation time per unit of time. It is assumed that the relaxation time does not depend on the initial velocity or location of the particle in the crystal;
- After a collision, the electron moves from the collision place in a random direction, with the speed determined only by the temperature of the region in which the collision did happen [50].

1.4.1.2 Classical Boltzmann Transport Equation

In the Drude model, the electron distribution is given by the Fermi-Dirac distribution:

$$f_{FD}(\epsilon, T) = \frac{1}{1 + exp((\epsilon - \epsilon_F)/k_B T)} \tag{1.15}$$

The Equation 1.15 describes the ideal electron gas with no external impact. However, in the classic Boltzmann Transport Equation (BTE), scattering, external forces, and diffusion are considered:

$$\frac{df(\mathbf{k}, T, t)}{dt} = \left(\frac{\partial f(\mathbf{k}, T, t)}{\partial t}\right)_s - \frac{dk}{dt}\nabla_k f(\mathbf{k}, T, t) - v(k)\nabla_r f(\mathbf{k}, T, t), \tag{1.16}$$

where $f(\mathbf{k}, T, t)$ is a distribution function of the wave vector $\mathbf{k}$ in the particular temperature T and in the t moment. By $v(\mathbf{k})$ the group velocity is given: $v(\mathbf{k}) = \nabla_k \epsilon(\mathbf{k})/\hbar$.

1.4.2 Deformation Potential Theory and Relaxation Time

In general, the values of relaxation time τ, so the time between collisions of the carriers and the periodic lattice, are not constant. The mobility of the carriers, and therefore the τ, in the unpolarized crystal are relevant to their dispersion on the acoustic phonons and, in an ideal system, to the impurities in the lattice.

In order to provide the exact τ value for the particular direction β in the crystal, the Deformation Potential (DP) theory is employed [54]. The idea behind this theory is to postulate the difference in electronic structure due to the mechanical deformation of the crystal. The DP as the parameter is understood as the difference in VBM/CBM position as the result of the mechanical stress put into the structure of the system. In this work, the modification of the lattice parameter for the DP calculations was plus 0.1 Å.

There is a strong correlation between relaxation time and temperature, as shown by the following formula:

$$\tau_\beta = \frac{2\sqrt{2\pi}C_\beta \hbar^4}{3(k_B T m_{eff})^{3/2} E_\beta^2}$$

where β is a direction in the crystal for which the particular parameter is mentioned, C_β is an elastic constant, m_{eff} is an effective mass, and E_β is the DP defined as the difference of the energy E (in VBM or CBM, depending on the type of carriers regarded) under the influence of the mechanical deformation: $E_\beta = \frac{\partial E_{VBM/CBM}}{\partial(\Delta l/l_0)}$; Δl and l_0 are the difference of the length due to the deformation and the origin length, i.e., lattice parameter.

1.5 Machine Learning

Nowadays, Machine Learning (ML) methods are commonly used in physics and also in the Heusler phases investigation. Parameters to be targets of the ML predictions vary from atomic site preferences [55], lattice parameters [56] and stability of the system [57], through band structures including band gaps [58, 59], to spin polarization [60] or thermal conductivity [61–63].

In general, ML is to provide external predictions based on the input data (*train subset*) taking under consideration the crucial features determining trend among the model. This idea determines the limited abilities of the ML model; it can only be as good and precise as the data it was *fed* with. At the very first stage, all the ML methods proceed the same: there is a feature space with *predictors* and *targets* required. *Predictors* are the

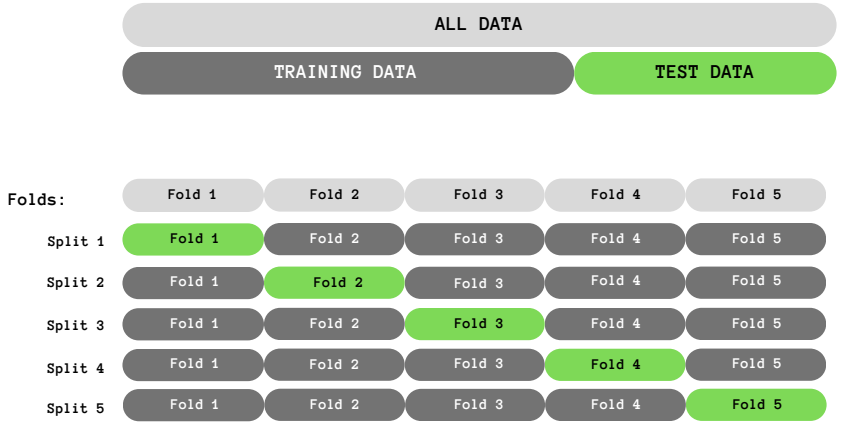

FIGURE 1.9: A schematic five-fold cross-validation train-test split method [64].

features used as the parameter values, which are used for calculating the expected value of the *target*. Among the data provided, there are the *train* and *test subset* defined; the *train subset* is used for the model to learn about the trends between *predictors* and *targets*, while the *test subset* is used to verify how accurate the trend analysis was by the comparison between the predicted and fact *target* values, not used for learning (Figure 1.9). The separation of the *train* and *test data* is crucial as it reduces the risk of overfitting the model (i.e., the ML model is too well fitted to the particular set of data and, even though it provides predictions close to the fact values, it is too limited to provide reasonable *target* values for the external, unknown data). The comparison of the actual *target* and the value predicted based on the *train subset* allows to determine if the model is proper and the *train data* is sufficient to provide good predictions of *targets*.

There are different methods of providing, so-called, *train-test split* among the initial feature space. In Figure 1.9 there is a *five-fold cross-validation* shown, but further discussion on the *cross-validation methods* is carried out in Chapter 1.5.1.2.

Also, there are multiple preferences for ML methods of prediction, depending on the type and size of the feature space and the character of the relations between predictors and targets. First of all, the difference between classificators and regressors is considered. In order to reveal the participation of the system in a particular subset, the classificators are implemented. For example, Huo *et al.* [65] employed the latent Dirichlet allocation (semi-supervised ML method) to classify inorganic material synthesis procedures.

The alternative approach is regression, which, contrary to the classificators providing the discrete class labels, delivers the continuous quantity predictions. The same as in the classificators case, the regression models also vary depending on the methodology used.

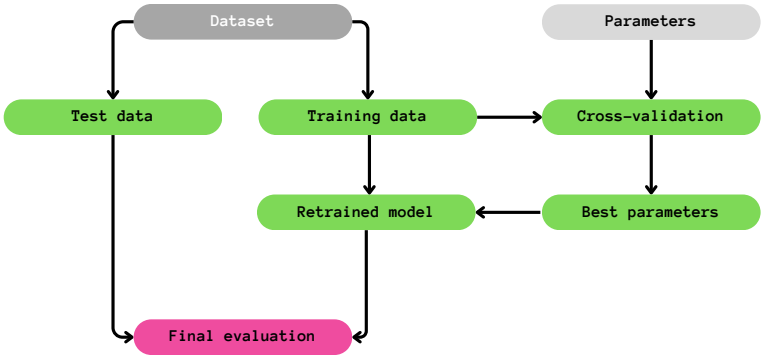

FIGURE 1.10: A flow chart of the evaluation of Machine Learning model [66].

Commonly used are "tree-like" models, e.g., Random Forest Regression [61] or Boosted Decision Tree Regression [62]. However, the particular regression method shall be chosen depending on the type of data and the expected trends among the *feature space*.

In order to reveal the best ML model possible for the provided data and *targets* desired, multiple versions of this model are investigated. First, it is determining the optimum subset of predictors; some out-of-the origin set of predictors may cause discrepancies in the patterns and provide worse results. Also, some crucial hyper-parameters, depending on the ML methodology used, must be tuned up. Only then, with the best predictors and the best hyper-parameters, it is possible to provide the predictions to be evaluated. This process is presented in Figure 1.10.

1.5.1 Support Vector Regression

Support Vector Regression (SVR) is a member of the Support Vector Machine family. Among this family, various methods, depending on the desired result, are implemented: regression, outlier detection, and classification. The major disadvantage of SVR is that it does not directly provide an estimation of probability, and expensive cross-validations are required. The advantages of SVR methods are as follows:

- effective if the number of dimensions is greater than the number of samples (requires the proper kernel function, Chapter 1.5.1.1);
- effective in high-dimensional spaces;
- memory efficient (uses a subset of training points in the decision function);
- versatile due to the different kernels available (Chapter 1.5.1.1) [67, 68].

The insight behind the SVR methodology is the hyperplane analysis (in the multidimensional feature space), which maximizes the number of records lying inside the strictly determined boundaries (decision boundary line) [69]. Such an approach creates the model that best fits the greatest part of the data provided.

Smola *et al.* [70] provided a complex analysis of the SVR methodology; below, a brief summary is presented.

Let us discuss the issue for the given input train data $\{(x_1, y_1), ..., (x_l, y_l)\} \subset \mathcal{X} \times \mathbb{R}$, where $\mathcal{X}$ is a space of the input patterns. Here considered and shown will be the linear function; however, the methodology can be applied to the various relations. The postulated form of the linear function is given as follows:

$$f(x) = \langle w, x \rangle + b, \tag{1.17}$$

where $w \in \mathcal{X}, b \in \mathbb{R}$ and $\langle \cdot, \cdot \rangle$ denotes to the *dot product* $\subset \mathcal{X}$. Let us make the assumption that such a f function does exist and approximates all (x_i, y_i) pairwise with precision given by ϵ ("convex optimization problem is *feasible*"). In order to investigate the *flatness* of Equation 1.17, small values of w are desired. It can be done by the norm minimalization, $\|w\|^2 = \langle w, w \rangle$, and the optimization issue about minimizing $\frac{1}{2}\|w\|^2$:

$$subject\ to \begin{cases} y_i - \langle w, x_i \rangle - b \leq \epsilon, \\ \langle w, x_i \rangle + b - y_i \leq \epsilon. \end{cases} \tag{1.18}$$

The assumption about *feasible* of the linear function is however non-realistic, and the possibility of error among the approximating results must be considered. In order to provide this *soft margin*, Vapnik [71] proposed the following formulas for minimizing $\frac{1}{2}\|w\|^2 + C\sum_{i=1}^{l}(\xi_i + \xi_i^*)$:

$$subject\ to \begin{cases} y_i - \langle w, x_i \rangle - b \leq \epsilon + \xi_i, \\ \langle w, x_i \rangle + b - y_i \leq \epsilon + \xi_i^*, \\ \xi, \xi^* \geq 0. \end{cases} \tag{1.19}$$

The constant $C > 0$ denotes the trade-off between the tolerated deviation larger than ϵ and the flatness of f. The deviation larger than ϵ, but still tolerated is described by the ϵ-intensive loss function $|\xi|_\epsilon$:

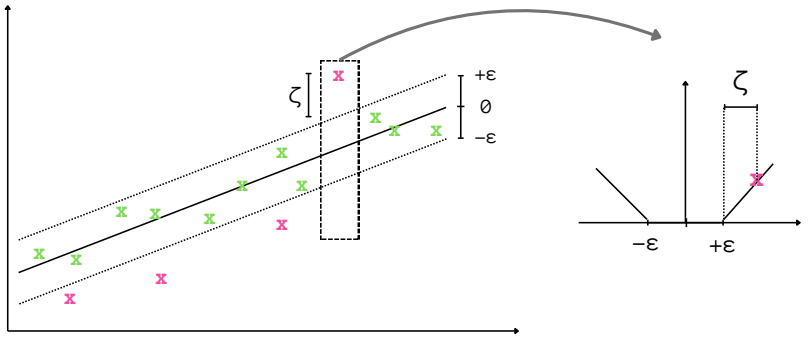

FIGURE 1.11: A visualization of soft margin loss for the linear kernel in the SVR model [70].

$$|\xi|_\epsilon = \begin{cases} 0 & if\ |\xi| \leq \epsilon, \\ |\xi| - \epsilon & otherwise. \end{cases} \tag{1.20}$$

In Figure 1.11 the illustration of the provided model is shown. As Smola *et al.* summed it up - the cost is determined solely by the points laying outside the *soft-margin* region (deviations are penalized linearly).

The analog intuition is applied to different types of functions and multi-dimensional feature spaces.

In order to determine the model with the best fit, different kernel functions are implemented (further discussion on the SVR kernels in Chapter 1.5.1.1).

Finally, the decision on SVR chosen for this investigation was determined by the character of the relations between predictors and targets, but this model was also reported to be reasonable and efficient for similar cases [72].

1.5.1.1 Tuning the hyper-parameters

- Kernel Functions

  A very big advantage of SVR models is the possibility of providing different kernel functions for the best fit, depending on the patterns among the data considered [73]. With, so-called, *the kernel trick*, the non-linear formulation variants of algorithms for Support Vector Machine can be applied to calculate dot products in the high-dimensional *feature space* [74].

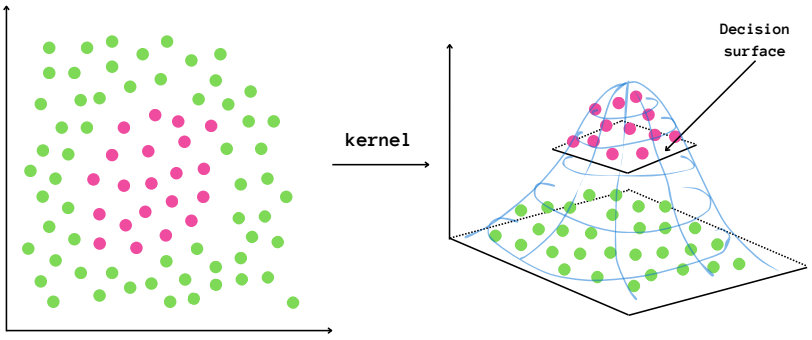

FIGURE 1.12: The Gaussian Radial Basis Function depicted for the classification issue [68].

The simplest kernel function is linear and given by the following formula: $\phi(r) = cr$. Only linear correlations between *predictors* and *targets* can be successfully described by such a simple function. The most universal and recommended kernel function for non-linear patterns is the Gaussian Radial Basis Function (RBF) defined as: $\phi(r) = e^{-cr^2}$ [75]. In Figure 1.12 there is a crucial idea behind the RBF for the classification issue presented.

Finally, depending on the kernel function used, the predicted values may differ strongly.

- C and γ parameters

  In order to deal with the trade-off between regularization and fitting the *training data*, the C parameter in SVR is implemented. At the same time, γ parameter is responsible for the flexibility of the model. C and γ can be determined by *grid-search* among the probable values, with a heat map determining the best combinations. Another option is to follow the default values implemented by Pedregosa *et. al* [67]: $C = 1$ and $\gamma = 1/(n * X_{VAR})$, where X_{VAR} is a variation in the predictors subset and n is the number of features.

1.5.1.2 Cross-validation

The issue of *leaking* the data from the *train* into the *test subset* is a crucial aspect of preparing a good ML model. It could be avoided by proposing an additional subset of the data to verify if there is no overfitting among the model's *validation set* (i.e., splitting the initial data into *train*, *test*, and *validation subset*). This approach, however, drastically reduces the number of samples in the *train subset* and therefore increases

the probable differences of the predictions due to the too small amounts of the *train data*. A solution proposed instead is so-called cross-validation (CV). The methodology beyond this approach is to provide more than one option of splitting the feature space into *train* and *test subsets*. Predictions are performed for all the options considered and combined. This method is more time- and resource-consuming, but it saves on the number of samples provided [66].

- k-fold

  The most common example of k-fold CV for $k = 5$ is depicted in Figure 1.9. In this approach, a model is trained with the use of $k - 1$, so-called *folds* as the *train data*. For every fold, the different subset of the initial data is regarded as the *test subset*, and the rest is a *train subset*.

- Leave One Out (LOO)

  This approach is an extreme version of the k-fold CV: only one sample is treated as the *test subset*, and the rest of the samples is used for *training* a model. The LOO approach is proposed as a very good CV option, especially for the Support Vector Machine family [76, 77].

1.5.1.3 Learning curves

In order to determine if the regarded *train subset* is sufficient to provide good predictions, the function of the quantitative verification and the number of *train samples* are considered (i.e., the *learning curve*). Learning curves can also be a useful guide on how much data must be added to the model to provide good enough predictions.

The accuracy of the ML model can be determined based on the different quantitative, e.g., the Root Mean Squared Error (RMSE) defined as:

$$\sqrt{\frac{1}{n}\sum_{i=1}^{n}(a_i^{calculated} - a_i^{predicted})^2},$$

where a is a studied quantity.

In general, it is expected that the accuracy of the model for small *train subset* is poor, and while extending the *training data*, the validation shall improve. If the plateau is observed, one may expect the amount of *training data* to be sufficient.

Chapter 2

Electronic Structure

2.1 Introduction

This chapter describes the initial stage of the investigation, focused mainly on the high-throughput calculations of numerous hH cubic systems in order to provide a limited list of potentially valuable TE materials. At this stage of the research, over 150 hH phases with 18 valence electrons were examined theoretically. Two different XC functionals were used to provide the most reasonable results. Among all investigated compounds, more than 120 proved to be semiconductors according to at least one XC functional. During the search for potentially valuable TE semiconductors, also some phases expected to be topological insulators were disclosed (e.g., LuPdAs).

Finally, 52 hH systems were investigated in terms of the potential TE performance [4, 6, 8]. In the set of 52 hH phases discussed here, 34 are defined as stable ($E_{HD} = 0$ eV) and 18 are likely to be stable (0 eV $< E_{HD} \leq 0.1$ eV) [23, 24, 28].

In this chapter, the analysis of electronic structure and elemental properties (e.g., equilibrium lattice parameter, band gap) of mentioned 52 hH systems is carried out. Final insights shall encourage further theoretical and experimental analysis for the listed phases, especially in the TE field.

2.2 Computational details

All the DFT calculations were performed with the use of the Vienna Ab initio Simulation Package (VASP) [78–81] with a **k**-point mesh of 262 points. The spin-orbit coupling (SOC) was included. The cut-off energy for the plane wave basis was 500 eV.

The XC functionals used were Generalized Gradient Approximation (GGA) [46] and modified Becke-Johnson GGA, i.e., the meta-GGA approach of Tran and Blaha (MBJGGA) [47], while the lattice parameter optimization was GGA-derived. The use of MBJGGA functional shall be justified by generally more reasonable results for semiconducting phases compared to GGA-derived calculations. However, the GGA approach also shall not be underestimated, as it was shown that it may offer the proper results in some cases of the limitations of the MBJ application [82]; finally, only the comparison of the results from two XC functionals may be considered sufficient and facilitates a discussion on electronic structure of intermetallics.

In order to determine the mechanical and thermodynamical stability of the systems investigated, the Born conditions for cubic systems were applied (Chapter 1.2.1) and the OQDM-derived stability was verified [23, 24, 28].

During the DFT examination of over 150 hH phases, 121 appeared to be semiconductors, according to at least one XC functional (Appendix A, Table A.1). Up to the date of the research and preparation of the *Search for semiconducting materials among 18-electron half-Heusler alloys* manuscript (i.e., Q2 2021), 49 alloys were neither experimentally nor theoretically investigated. Based only on the percentage of not-examined systems among all the semiconductors considered, this shall encourage further investigation, not only focused on the TE properties.

In further research, only the stable (E_{HD} = 0 eV) or likely stable ($0 < E_{HD} \leq 0.1$ eV) hH phases are considered. Mentioned 52 hH systems (34 stable and 18 likely stable) are gathered in Table, whereas the complete version of this table (including unstable hH phases) is available in Appendix A, Table A.2.

Comp.	ΔH	E_{HD}	Comp.	ΔH	E_{HD}
HfPdGe	-0.832	0.100	TiPdGe	-0.723	0.088
HfPtGe	-0.983	0	TiPdPb	-0.379	0.065
HfCoAs	-0.828	0	TiPtGe	-0.884	0
HfCoBi	-0.365	0	TiPtSn	-0.871	0
HfRhAs	-0.989	0.017	TiCoAs	-0.863	0
HfNiSn	-0.665	0	TiCoBi	-0.321	0
HfPdSn	-0.752	0	TiRhAs	-0.912	0
HfIrSb	-0.924	0	TiRhBi	-0.531	0
LuNiAs	-1.030	0.073	TiIrSb	-0.815	0
NbCoGe	-0.511	0	VCoGe	-0.391	0
NbIrGe	-0.598	0	VRhGe	-0.456	0.045
NbFeAs	-0.514	0	VIrGe	-0.451	0

NbRuAs	-0.493	0.018	VFeAs	-0.468	0
NbRuBi	-0.149	0.083	VFeSb	-0.211	0
NbIrSn	-0.558	0	VRuSb	-0.285	0.063
NbRuSb	-0.421	0	ZrNiGe	-0.792	0.016
ScPdAs	-1.125	0.084	ZrPdSn	-0.817	0
ScPdBi	-0.836	0	ZrPtGe	-0.996	0
TaCoGe	-0.494	0	ZrPtPb	-0.724	0
TaCoSn	-0.317	0	ZrCoAs	-0.880	0.019
TaRhGe	-0.551	0.008	ZrRhAs	-1.070	0.063
TaFeAs	-0.467	0	TiFeTe	-0.539	0
TaFeSb	-0.304	0	TiRuTe	-0.654	0.052
TaRuAs	-0.431	0	ZrFeTe	-0.600	0.059
TiNiGe	-0.701	0	ZrRuTe	-0.702	0
TiNiPb	-0.278	0.043	HfRuTe	-0.696	0.061

TABLE 2.1: Summary of the composition analysis, where: ΔH (eV/atom) - hull energy and E_{HD} (eV/atom) - distance from the convex hull, i.e., hull distance.

2.3 Defining and limiting the half-Heusler subset

The first stage of investigation was concerned with the *ab initio* calculations for 153 hH cubic systems with eighteen valence electrons in order to narrow down the initial set to semiconducting, stable (or likely stable), and novel (i.e., not investigated in terms of the potential TE application or investigated partially, with one basic XC functional used, e.g., GGA or LDA) compounds. Phases investigated were of the following formulas according to the periodic groups of elements:

- `III-X-XV` (e.g., ScNiSb),
- `IV-X-XIV` (e.g., HfNiSn),
- `IV-IX-XV` (e.g., HfCoSb),
- `V-IX-XIV` (e.g., NbCoSn),
- `V-VIII-XV` (e.g., NbFeSb).

The elements of the particular periodic groups were selected as given:

- `III` (Sc, Y, La, Ga, In),

- `IV` (Ti, Zr, Hf),
- `V` (V, Nb, Ta),
- `VIII` (Fe, Ru, Os),
- `X` (Ni, Pd, Pt),
- `XIV` (Ge, Sn, Pb),
- `XV` (As, Sb, Bi).

All the possible 18-electron combinations of hH phases were considered. The *ab initio* calculations were performed with the use of DFT with GGA and MBJGGA parametrizations. The use of the GGA approach is commonly described in the literature [1–3, 83–107, 112], also for NbFeSb systems [108], whereas one in general shall expect more reasonable results provided by MBJGGA parametrization in the case of semiconducting phases. Nevertheless, all the results considered here were provided and discussed for both XC functionals.

The initial values of the lattice parameter (input for *ab initio* calculations) were delivered with the ML support (see more in Chapter 4), providing non-equilibrium lattice parameters for all the 153 hH systems with a very good effectivity (only one system required manual modification of the initial a to allow the fast structural relaxation). Examinations of all the possible combinations allowed for pointing out the semiconducting phases, which is a requirement for the thermoelectric material.

In general, the hH phases with a VEC of 18 are expected to be stable [14–18]. However, it is not common for such a stable phases to adopt an investigated here symmetric Face Centered Cubic (FCC) lattice (XYZ) with a $F\bar{4}3m$ space group [4]. The Wyckoff positions for X, Y, and Z are as follows: (0, 0, 0), (1/4, 1/4, 1/4), and (1/2, 1/2, 1/2). Nevertheless, numerous systems of this type have not yet been examined, neither experimentally nor theoretically. The decision on systems provided in this work was inspired by both the novelty of systems and OQMD-derived stability determinant, while the '10 k_BT rule' proposed by Mahan *et al.* [109] for nominating the TE candidates was found to consider only narrow band gap systems (e.g., ZrNiSn, whose band gap reported 0.05 eV (experiment [83]) and 0.18 eV (theory [91]), but at the same time to neglect TE valuable phases with wide band gaps (e.g., ZrRhBi E_g = 1.02 eV [110]). Therefore, the OQMD-derived stability criterion was applied to distinguish 34 stable hH phases [6] and 18 likely stable hH phases [8]. Additionally, Te-bearing hH alloys (two stable: ZrRuTe and TiFeTe; three likely to be stable: TiRuTe, ZrFeTe, and HfRuTe),

not included in the initial set of the systems, were also investigated in therms of the potential TE applications [5].

The detailed results of *ab initio* examination of the electronic structures and the elemental properties are described in the subsections focused on 34 stable hH phases and 15 likely stable hH phases (excluding three Te-bearing systems), separately. The very last part of this chapter is devoted to the discussion on six hH phases revealed here as possessing the band structure which suggests the Topological Insulator (TI) character.

2.4 Stable hH phases

The first stage of the research, after determining the final hH subset to be considered, was a careful analysis of the electronic structures. In all the cases, band structures were analyzed in the $L-\Gamma-X-U$ directions in the IBZ of the FCC system (Chapter 1.2). With black and red lines the GGA- and MBJGGA-derived results are marked. The horizontal dashed line (0 eV) is set at the Fermi level of the particular system. In Figure 2.1, the band structures of the 34 stable hH phases regarded here are presented. The order of the hH phases is due to the weight of the X, Y and Z ions. This kind of sorting could be found to be the most comfortable for comparison of the similar systems (e.g., VCoGe vs. VIrGe).

The general features of electronic structures of the 34 semiconducting hH phases considered here are consistent with the literature data for similar hH systems. One shall perceive characteristic shapes of the band structure and types of band gaps revealed.

First of all, there is a distinction between GGA and MBJGGA-derived results; the first XC functional in the majority of cases provides the underestimated values compared to the MBJGGA approach. The only systems with wider E_{GGA} than E_{MBJ} were: HfNiSn (E_{GGA} = 0.32 eV, E_{MBJ} = 0.27 eV), HfPdSn (E_{GGA} = 0.38 eV, E_{MBJ} = 0.33 eV), ZrPdSn (E_{GGA} = 0.44 eV, E_{MBJ} = 0.42 eV), TiNiGe (E_{GGA} = 0.63 eV, E_{MBJ} = 0.58 eV), TiCoBi (E_{GGA} = 0.88 eV, E_{MBJ} = 0.78 eV), HfCoBi (E_{GGA} = 0.98 eV, E_{MBJ} = 0.92 eV), and TiCoAs (E_{GGA} = 1.30 eV, E_{MBJ} = 1.24 eV).

Comp.	a	C_{11}	C_{12}	C_{44}	E_g^{GGA}	E_g^{MBJ}
ScPdBi	6.525	124.19	65.93	42.11	0.07	0.12
HfNiSn	6.111	243.62	73.72	73.85	0.32	0.27
HfPdSn	6.360	186.38	93.09	67.71	0.38	0.33
ZrPdSn	6.396	178.99	86.55	63.05	0.44	0.42
NbRuSb	6.187	261.71	125.22	64.32	0.35	0.48

TiNiGe	5.668	234.41	95.40	92.68	0.63	0.58
VIrGe	5.818	269.95	169.88	75.76	0.27	0.64
VFeSb	5.788	280.55	98.83	46.43	0.34	0.66
NbFeAs	5.689	314.37	115.02	89.24	0.57	0.67
NbIrGe	6.010	274.14	156.94	89.76	0.60	0.72
ZrPtPb	6.508	184.52	90.27	58.71	0.67	0.73
NbIrSn	6.230	266.14	132.14	74.60	0.63	0.73
HfIrSb	6.333	244.23	112.19	75.01	0.66	0.75
TiCoBi	6.033	220.70	75.00	44.51	0.88	0.78
TaRuAs	5.972	264.62	158.49	73.04	0.37	0.78
TiPtSn	6.231	200.50	108.25	65.16	0.67	0.81
TiRhBi	6.280	179.09	93.95	38.19	0.66	0.81
VFeAs	5.496	304.34	126.62	88.41	0.36	0.86
TaFeSb	5.960	321.09	98.45	74.52	0.81	0.87
TiPtGe	5.991	205.37	126.35	77.47	0.72	0.91
HfCoBi	6.188	235.70	65.63	53.29	0.98	0.92
TiRhAs	5.889	205.21	128.96	69.07	0.77	0.96
TiIrSb	6.165	235.91	119.58	67.56	0.68	0.97
TaFeAs	5.692	328.70	128.43	93.13	0.88	0.98
VCoGe	5.512	284.29	121.07	90.82	0.68	0.99
HfPtGe	6.171	213.48	124.52	77.25	0.93	1.02
TaCoSn	5.962	300.97	96.36	76.20	1.01	1.03
ZrPtGe	6.200	210.95	119.11	73.74	1.01	1.08
NbCoGe	5.698	308.47	116.33	98.41	1.09	1.13
TiFeTe	5.864	278.92	84.13	66.19	0.98	1.18
TaCoGe	5.715	314.53	125.23	104.10	1.16	1.19
TiCoAs	5.605	267.42	104.92	92.32	1.30	1.24
ZrRuTe	6.298	237.25	100.41	63.43	0.93	1.25
HfCoAs	5.783	275.77	99.48	79.76	1.29	1.36

TABLE 2.2: Table of selected systems with the following parameters revealed: equilibrium lattice parameter a (Å), elastic constants C_{11}, C_{12}, and C_{44} (GPa), band gaps from GGA E_g^{GGA} (eV) and MBJGGA E_g^{MBJ} (eV) approaches.

The reason for this behavior may be due to the specific electronic structure; HfNiSn, HfPdSn, ZrPdSn, and TiNiGe are characterized by: 1) the $\Gamma - X$ indirect transition type; 2) relatively low position of valence bands at the L point; and 3) a U-like conduction band shape in the CBM vicinity. The remaining three hH systems with GGA-derived band gap larger than obtained with MBJGGA are: TiCoBi, HfCoBi, and TiCoAs. In

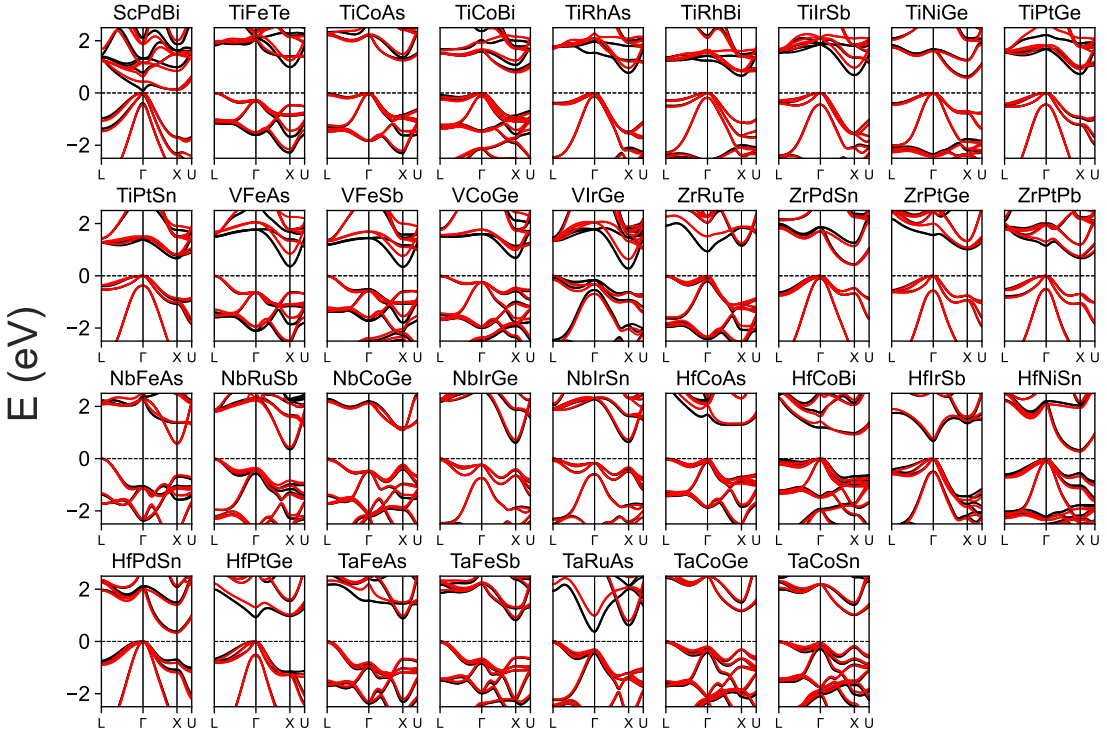

FIGURE 2.1: Band structures of hH alloys obtained with GGA and MBJGGA, marked with black and red colors, respectively.

this case, the band structures of Co-bearing systems are different from those of HfNiSn (band structures similar to those of NbFeSb with higher energy values of the valence band in the vicinity of the L point and flat valence bands in the $L - \Gamma$ direction). What is common for almost all systems is the CBM located at the X point with a relatively small discrepancy between the GGA and MBJGGA-derived conduction bands. Also, for the valence bands, the difference between the results of the GGA and MBJGGA parametrizations is negligible.

The rest of the systems analyzed in this part of the research are characterized by the E_{MBJ} exceeding E_{GGA}, which is in agreement with the expectations [47] and previous results for similar hH phases [1–3].

The tendency to narrow the band gap when a single element is replaced with a heavier one was observed for some phases (e.g., VCoGe and VIrGe, TiCoAs and TiCoBi). This trend was also revealed in the previous research on similar hH phases [1–3]. More examples of such a behavior (for a single and more elements replaced) are observed in the following cases:

- TiRhAs ($E_{GGA} = 0.77$ eV, $E_{MBJ} = 0.96$ eV) and TiRhBi ($E_{GGA} = 0.66$ eV, $E_{MBJ} = 0.81$ eV);

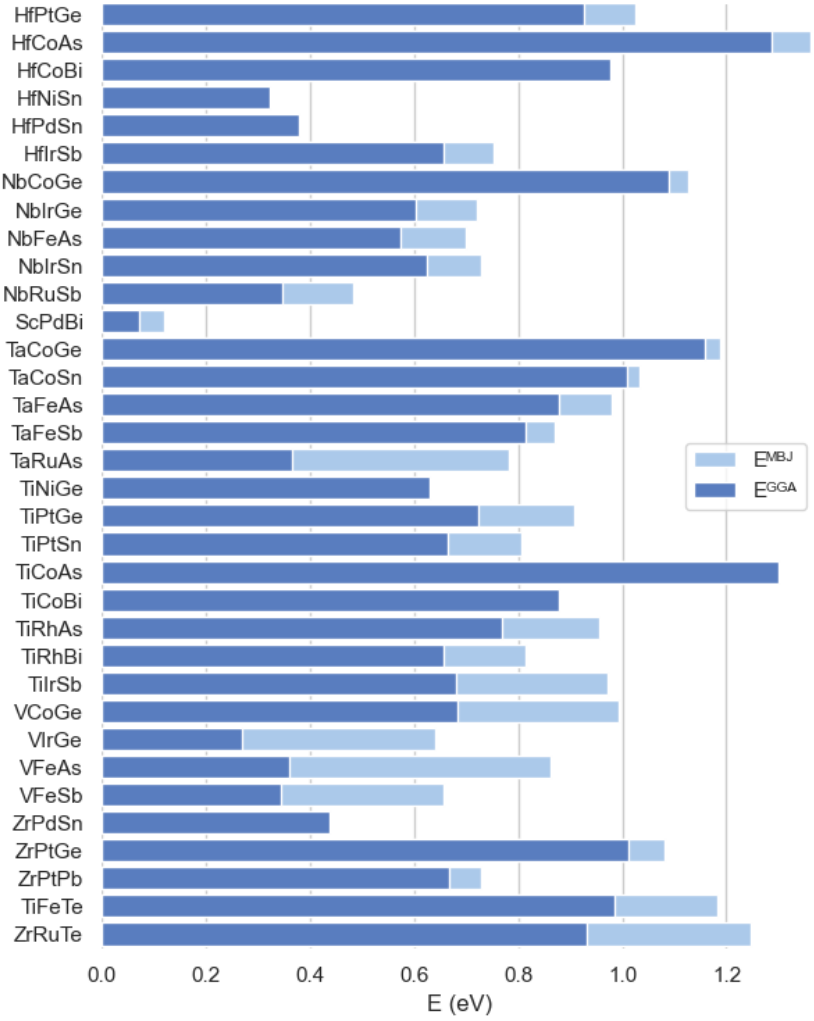

FIGURE 2.2: A bar plot of GGA and MBJGGA-derived band gaps for selected systems.

- TiNiGe (E_{GGA} = 0.63 eV, E_{MBJ} = 0.58 eV) and TiPtGe (E_{GGA} = 0.72 eV, E_{MBJ} = 0.91 eV);
- VCoGe (E_{GGA} = 0.68 eV, E_{MBJ} = 0.99 eV) and VFeSb (E_{GGA} = 0.34 eV, E_{MBJ} = 0.66 eV).

The opposite phenomenon was disclosed for the following phases: VFeAs (E_{GGA} = 0.36 eV), NbFeAs (E_{GGA} = 0.57 eV), and TaFeAs (E_{GGA} = 0.88 eV). The lighter the X ion, the narrower the GGA-derived band gap. The MBJGGA-derived results for VFeAs, NbFeAs, and TaFeAs do not exhibit the observed widening of the band gap for the heavier elements constituent. Also, pairs: NbIrGe (E_{GGA} = 0.60 eV, E_{MBJ} = 0.72 eV) and NbIrSn (E_{GGA} = 0.63 eV, E_{MBJ} = 0.73 eV); NbIrGe (E_{GGA} = 0.60 eV, 0.72 eV) and NbIrSn (E_{GGA} = 0.63 eV, 0.73 eV) fulfill the behavior of the wider band gap for the heavier elements constituent.

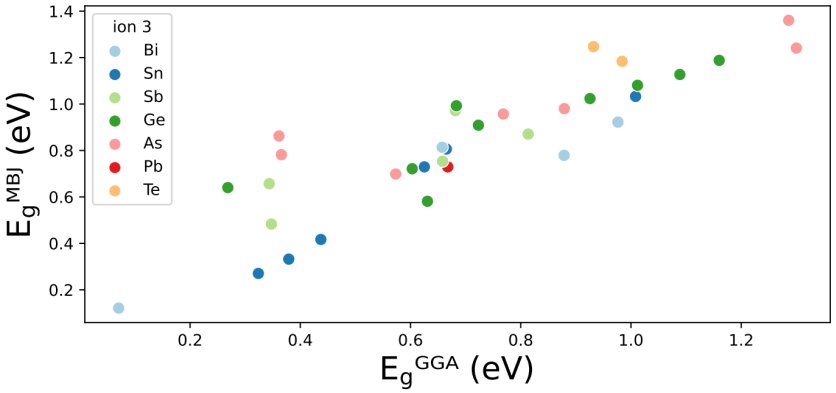

FIGURE 2.3: The relation between GGA- and MBJGGA-derived band gaps for selected systems, whereas Y ions are marked with different colors.

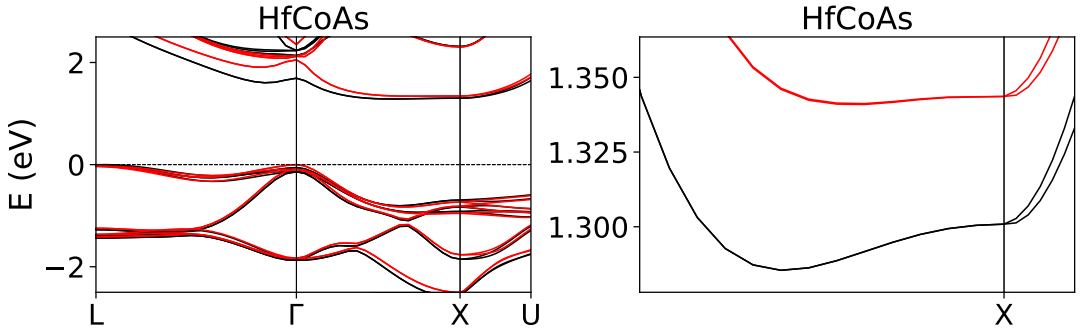

FIGURE 2.4: The detailed band structure of HfCoAs is shown (on the right) with the conduction bands in the vicinity of the CBM.

One shall imply that the relation between the width of the band gap and the weight of the constituent elements is not obvious and should be analyzed separately for each system or, at least, for each type of system bearing the particular elements. The reason for the widening or narrowing of the band gap for heavier elements is due to multiple factors. It is expected for the heavier elements to be characterized by greater ionic radii compared to the lighter elements in the same group. This tendency also affects the distances between ions and, therefore, the lattice parameter. Another factor important for this issue may be the electronegativity, in particular higher for lighter elements, i.e., lighter elements tend to attract electrons stronger than heavier elements. The electronegativity of the particular elements, especially in the case of replacing only a single ion, may influence the character of the electronic structure. In the end, it is the overlap of the orbitals that determines the final electronic structure. Lighter elements are characterized by different orbitals, and, therefore, the hybridization may vary depending on the particular orbitals of the constituent elements. In general, one may expect the heavier ions to provide the narrower band gaps(e.g., GGA- and MBJGGA-derived NbCoGe and NbIrGe); however, some exceptions were noted (e.g., GGA-derived HfNiSn and HfPdSn).

In Figure 2.2, the comparison of E_{GGG} and E_{MBJ} is depicted. One shall perceive the consequent exceeding of GGA-derived results over the MBJGGA approach. This observation is consistent with previously discussed expectations of an underestimation of band gaps by GGA.

For some systems investigated here, the difference between E_{GGA} and E_{MBJ} is enormous, e.g., VFeAs, VIrGe, and TaRuAs. The phases listed are characterized by different band structures: VFeAs has NbFeSb-like (VBM at the L point, CBM at the X point but with simultaneous higher energy values of the valence bands in the vicinity of the X point) [112], VIrGe has NbRuBi-like [4], while VFeAs has NbOsBi-like [4].

Some of the systems are characterized by good accordance between E_{GGA} and E_{MBJ}: NbCoGe, TaCoGe, TaFeSb, ZrPtGe, and ZrPtPb. NbCoGe, TaCoGe, ZrPtGe, and ZrPtPb have very similar electronic structures; also, the band structure of TaFeSb is alike, but with a significant downshift of conduction bands, located above the CBM in the rest of the systems discussed. Also, some of the phases considered unexpectedly provided a wider GGA-derived band gap than MBJGGA-derived (discussed above). Additionally, in Figure 2.3, the correlation between E_{GGA} and E_{MBJ} with Z ions marked with colors is depicted. The discrepancies between GGA and MBJGGA-derived band gaps are visible, in particular for As, Ge, and Sb-based hH systems.

As a highly unique electronic structure, HfCoAs band structure and CBM is disclosed (Figure 2.4). This example is the only one among the systems considered here to reveal CBM neither at the Γ nor the X point, but in between them, and moreover, for both XC functionals applied.

2.5 Likely stable hH phases

In Table 2.3 additional 15 hH phases (excluding tellurides due to the lack of tellurides in the target subset) with selected elemental parameters are gathered [8].

Mentioned hH systems are characterized by hull distance E_{HD} following range: 0 eV $<$ $E_{HD} \leq$ 0.1 eV (detailed values are presented in Table A.2) [23, 24]. In Figure 2.5 the distribution of E_{HD} and formation energy ΔH is presented. The real alloys may adopt metastable phases even if the total energy is above the curve of the convex hull. This fact results from the inaccurate estimation of the theoretical-derived formation energies for particular systems (space group $F\bar{4}3m$). Proposed limitations of E_{HD} indicate likely stable materials [28]. As can be inferred from Figure 2.5, no ion unequivocal determines E_{HD}; the lowest E_{HD} is revealed for TaRhGe, whereas the highest E_{HD} of 0.1 eV

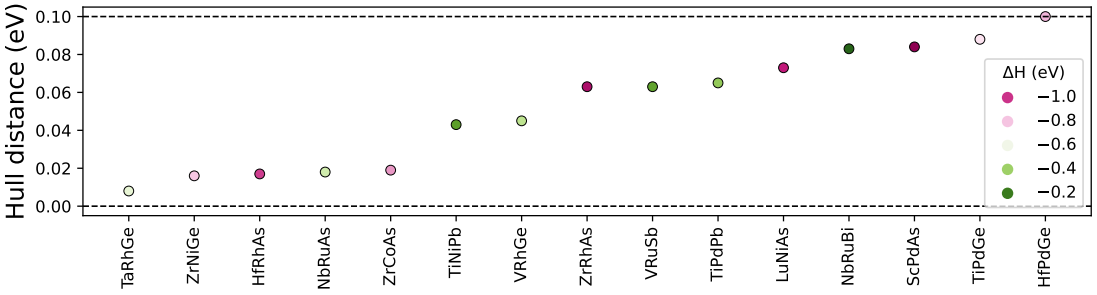

FIGURE 2.5: A distribution of hull distance E_{HD} for selected hH phases. The values of formation energy ΔH are marked with respective colors.

characterizes another Ge-based alloy, i.e., HfPdGe. Regarding formation energy, the As-based hH compounds discussed here exhibit relatively low ΔH compared to Pb-, Sb-, and Bi-bearing phases.

Comp.	a	C_{11}	C_{12}	C_{44}	E_g^{GGA}	E_g^{MBJ}
TiPdPb	6.328	142.43	84.61	43.98	0.35	0.32
TiPdGe	5.964	169.53	112.30	69.11	0.62	0.58
VRhGe	5.796	227.77	144.92	68.76	0.43	0.75
ZrCoAs	5.831	265.22	88.76	73.84	1.20	1.23
ZrRhAs	6.110	202.36	114.78	68.14	1.12	1.29
HfPdGe	6.142	179.29	110.92	72.83	0.55	0.51
HfRhAs	6.063	216.10	131.98	70.44	0.28	0.82
TaRhGe	5.973	251.19	152.10	88.02	1.04	1.03
VRuSb	6.044	237.79	129.57	44.91	0.19	0.63
ZrNiGe	5.893	246.34	89.18	79.85	0.68	0.65
ScPdAs	6.099	142.02	95.96	60.30	0.43	0.45
NbRuAs	5.961	255.97	146.71	73.63	0.34	0.51
TiNiPb	6.038	197.16	74.91	52.40	0.34	0.29
NbRuBi	6.307	233.14	111.08	41.55	0.38	0.56
LuNiAs	5.989	187.85	66.49	49.29	0.41	0.48

TABLE 2.3: Table of selected systems with the following parameters revealed: equilibrium lattice parameter a (Å), elastic constants C_{11}, C_{12}, and C_{44} (GPa), band gaps for GGA E_g^{GGA} (eV) and MBJGGA E_g^{MBJ} (eV) approaches.

The equilibrium lattice parameters (from 5.796 Å for VRhGe up to 6.328 Å for TiPdPb) and elastic constants C_{11}, C_{12}, and C_{44} were calculated with the use of GGA parametrization. Systems presented here exhibit strongly varying E_g values: from $E_g^{GGA} = 0.19$ eV for VRuSb and $E_g^{MBJ} = 0.29$ eV for TiNiPb up to $E_g^{GGA} = 1.20$ eV for ZrCoAs and

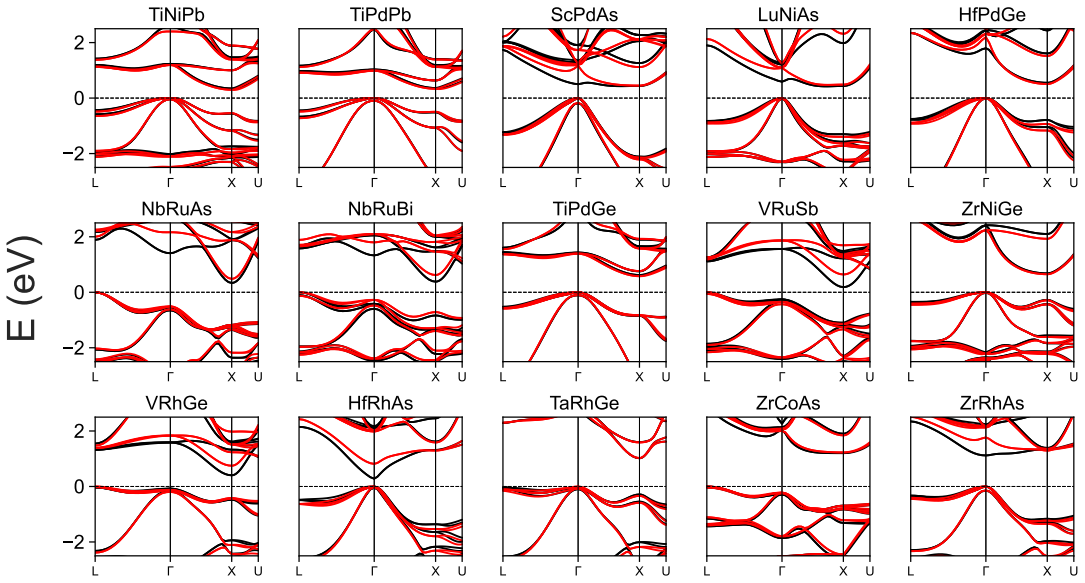

FIGURE 2.6: The band structures of selected systems, whereas with black and red, GGA and MBJGGA parametrizations are marked, respectively.

$E_g^{MBJ} = 1.29$ eV for ZrRhAs. In terms of the potential TE application at room temperature, materials with relatively narrow band gaps are preferred (e.g., NbFeSb with reported $E_g = 0.51$ eV [112]). However, in some cases, systems with even wider band gaps reveal good TE performance (e.g., E_g of 0.81 eV for TaFeSb [6]).

In Figure 2.6 the band structures of the likely stable hH phases are depicted. The expected underestimation of E_g^{GGA} with respect to E_g^{MBJ} is observed. Also, in some cases, the modifications of VBM or CBM locations for different XCF parametrizations employed are visible. Despite the well-known fact that MBJGGA is dedicated to studies on semiconducting systems, the intermetallics discussed here are complex, and the reasonable theoretical examination shall be based on at least two XCF parametrizations considered. While it is an experimental investigation to finally verify the theoretical insights.

Among the materials studied here, the majority exhibit the semiconducting character with visible dominance of the indirect transition type; only Rh-based arsenides exhibit the $\Gamma-\Gamma$ direct transition type (GGA parametrization). The similarity of band structures obtained here to the band structures of well-known hH phases is observed (e.g., LuNiAs and LuNiBi [3]; NbRuAs and NbFeSb [111, 112]). Some general trends in the shapes and positions of VBM and CBM in phases with similar compositions may be observed, e.g., for TiNiPb, TiPdPb, and TiPdGe. The specific shape of the conduction bands with CBM located in between the X and Γ points is present in ScPdAs (GGA-derived results) and LuNiAs (from GGA and MBJGGA). Additionally, the widening or narrowing of E_g

is observed depending on the weight and radii of the ions. Namely, for NbRuAs and NbRuBi (with relatively large volumes of unit cells due to the Bi ion), the narrowing of E_g is revealed, whereas the widening of E_g is observed for TiPdPb and TiPdGe (GGA and MBJGGA-derived results) according to the relatively light Z ions.

As the crucial factor for the description of the electronic structure of narrow band gap hH phases, SOC is included [2]. For some systems, the effect of SOC is relatively weak (hH arsenides), whereas for some phases (i.e., Ru-, Rh-, and Pd-bearing), it is clearly noticeable as splitting in valence bands.

2.6 Topological Insulators

In Figure 2.7 the band structures of the systems that are considered candidates for TI are depicted. A comprehensive analysis of the band inversion was not carried out. However, due to: 1) the characteristic shape of the band structure in the vicinity of CBM and VBM; 2) consequent GGA and MBJGGA-derived confirmation of the zero band gap; and 3) similar band structures analyzed in the past, the following systems were proposed as the TI: MBJGGA-derived ScPtAs [113], HfIrAs [14, 114], HfIrBi [14], YPdBi [115], and LuPtSb [116]. What is important here is the comparison of YPdBi and YPdAs (MBJGGA-derived semiconductors) - opposite for the revealed MBJGGA-derived electronic structure findings, the occurrence of the relatively heavier element constituent (Bi vs. As) in the particular phase resulted in the closure of the band gap. This finding may be crucial for understanding the narrow boundary of the GGA's applicability for semiconductors and TI. The TI vs. semiconducting classification of the mentioned phases differs for YPdBi and LuPdAs, whereas LuPdAs was recently reported by Mafe *et al.* [117] as a semi-metallic phase with a zero band gap. The rest of the systems listed here may also be MBJGGA-derived semi-metals. The investigation of non-trivial TI behavior and its realization within the electronic structure requires further research.

The electronic structures of potential TIs reveal two types of band structures: HfIrBi-like and YPdBi-like. The first one is characterized by a steep conduction band and a single dominant local minumum at the Γ point. Whereas, the second type, YPdBi-like, reveals a more complex conduction band region with a local minimum observed at the X point. The position of valence bands in the first case is characterized by higher energies at the L point, while for the second type, significantly lower energies are presented at the same point.

TIs were not the main subject of this study and no further analysis of their properties was carried out. This issue and the listed systems require further research.

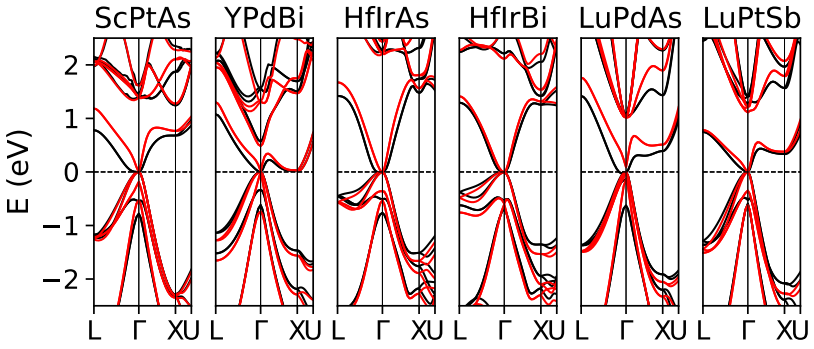

FIGURE 2.7: Systems proposed as TIs. With black and red lines the GGA and MBJGGA-derived results are shown.

2.7 Conclusions

This research stage provides a deep insight into the electronic structures of 34 stable (and mainly not investigated yet in terms of the potential TE performance) and 15 likely stable hH systems out of initial over 120 hH 18-electron semiconductors. The detailed analysis of band structures obtained with GGA and MBJGGA parametrizations is performed separately for stable and likely stable hH phases. Some characteristic features of the electronic structures were discussed and compared with the literature data. The specific shape of the band structure of HfCoAs in the vicinities of CBM is revealed and discussed. Additionally, some candidates for TI were presented.

First of all, the correlations between the width of the band gap and selected features (e.g., weight of the element constituent) were discussed in detail; in general, the inverse relation between E_g and the atomic weights of X and Y (in this order) is observed, but with some exceptions, taking different XC functionals into consideration. Additionally, the importance of SOC for heavy-ion systems is depicted.

Another significant insight is concerned with the differences between MBJGGA- and GGA-derived results, which were discussed in detail. For some systems (e.g., ScNiAs), vivid modifications of the conduction bands are observed, whereas in different cases, the GGA- and MBJGGA-derived band structures are highly similar (e.g., TiPdGe). Such findings ensure the requirement of providing at least two XC functional parametrizations for theoretical analysis of hH phases.

Chapter 3

Thermoelectric Performance

3.1 Introduction

In this part of the research, 49 stable and likely stable hH phases were analyzed in terms of TE performance. Among mentioned 49 hH phases, over 30 were not investigated yet at all as candidates for TE materials. The list of all the systems neglected at this stage due to the TE properties already reported or according to the non-zero E_{HD} is presented in Appendix A. Additionally, two Te-bearing hH systems (TiFeTe and ZrRuTe), not included in the initial hH set (Chapter 2), were considered here [5].

After the implementation of the declared limitations (Chapter 1.2.1), two subsets were revealed: 1) 34 stable (E_{HD} = 0 eV), and 2) 15 likely stable (0 eV < $E_{HD} \leq$ 0.1 eV) hH phases. The electronic structures of these phases are carefully discussed in Chapter 2, whereas in this chapter the complex analysis of TE performance (i.e., PF and ZT for GGA and MBJGGA parametrizations and for the p/n-type regimes) and crucial factors to determine it (e.g., effective mass of the carriers) is performed.

The analysis of the TE performance was extended by the DP theory application for the relaxation time calculations (Chapter 1.4.2) and the lattice thermal conductivity calculations (following the methodology by Slack [118]). Thanks to the two models applied, the two XC functional parametrizations, and the different doping considered at 300 and 900 K, the findings presented in this part of the research shall be considered highly realistic.

In this discourse, various chemical trends in transport and electronic properties were analyzed. Some promising TE candidates are proposed here. Especially, considering only stable hH phases, TaFeAs (PF_{GGA} = 1.67 mW/K^{2}m, ZT_{GGA} = 0.024 for p-type regime and PF_{GGA} = 2.91 mW/K^{2}m, ZT_{GGA} = 0.025 for n-type regime) could be considered

as good TE materials, but also results of the TE performance for TaFeSb, VFeAs, and TiRuAs shall encourage more extended studies on the hH phases named here. The analysis of PF and ZT for likely stable phases favored NbRuAs (n-type regime and GGA parametrization), VRuSb (n-type regime for both XC functionals considered), and NbRuBi (n-type regime and GGA parametrization). What is worth noting here is the fact that for some systems considered, GGA and MBJGGA parametrizations derived very similar and relatively high PF values for the particular type of carriers, e.g., VRhGe and TaRhGe for the n-type regime or LuNiAs and LuNiSb for the p-type regime.

The overall insights of this stage of the investigation were summarized in *High-throughput exploration of half-Heusler phases for thermoelectric applications* [6], but also part of *Machine Learning-Based Predictions of Power Factor for Half-Heusler Phases* [8] was devoted to the TE performance of likely stable hH phases considered here.

3.2 Computational details

The comprehensive methodology of DFT calculations is described in the Computational Details in Chapter 2. The elastic constants and equilibrium lattice parameters were provided with GGA parametrization. The calculations of the transport and thermoelectric properties were performed following the Boltzmann equation with the use of BoltzTraP2 software [119]. The mesh of **k**-points for the transport calculations was set to 125 000 points in IBZ. The stability criteria applied to the systems considered are: 1) 18-valence electrons; 2) Born criterion of mechanical stability for cubic systems; and 3) formation energies OQMD-derived (analysis of the convex hull and hull distance E_{HD}) (Chapter 1.2.1). Only the phases with $E_{HD} \leq 0.1$ eV (cubic ground state crystal structures expected) are considered in this part.

In order to provide the most realistic results, the DP theory was implemented; the relaxation time formula resulting from the DP theory is given in Chapter 1.4.2. The methodology of the constituent effective mass calculations is described in Appendix C.

The illustrative diagram of the whole investigation process is depicted in Figure 1.1.

3.2.1 Lattice thermal conductivity

In order to provide the ZT investigation, the lattice thermal conductivity κ_L for the particular systems was required. As commonly realized in the literature method, Slack's equation was implemented [118, 120, 121]. The calculations of κ_L in this approach are fully based on the GGA-derived elastic constants of the equilibrium system: C_{11}, C_{12}, and

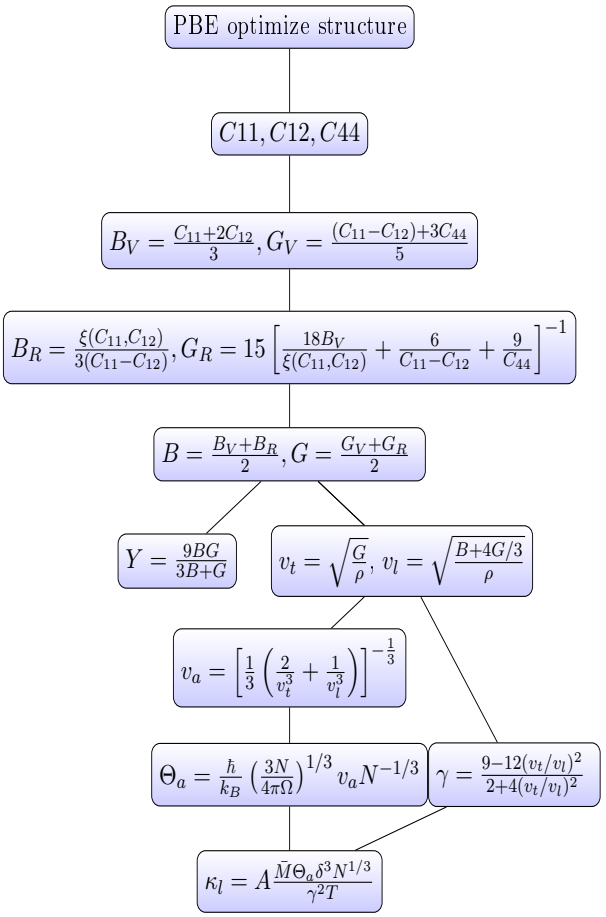

FIGURE 3.1: Illustration of lattice thermal conductivity calculations following Slack's methodology, where $\xi(C_{11}, C_{12}) = (C_{11} + C_{12})C_{11} - 2C_{12}^2$. The parameters considered: elastic constants C_{11}, C_{12}, C_{44} (GPa), bulk modulus B (GPa), Young's modulus Y (GPa), average sound velocity v_a, Grüneisen parameter γ, density ρ (g/cm^3), Debye temperature Θ_D (K), acoustic-mode Debye temperature Θ_a (K) and lattice thermal conductivity κ_L (W/mK).)

C_{44}. The Slack's equation for κ_L requires previous calculations of multiple intermediary quantities: bulk modulus B (GPa), Young's modulus Y (GPa), average sound velocity v_a, Grüneisen parameter γ, density ρ (g/cm^3), Debye temperature Θ_D (K), and acoustic-mode Debye temperature Θ_a (K). The complete diagram of the calculation process is depicted in Figure 3.1.

3.3 Effective mass and relaxation time of carriers

The effective mass value is directly given by the curvature of bands in the vicinities of VBM and CBM [122]:

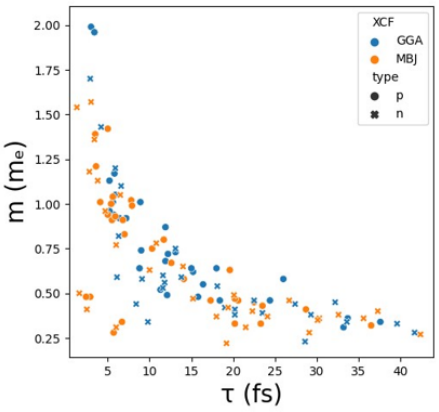

FIGURE 3.2: The relationship between effective mass and relaxation time with XC fucnctional parametrization and type of carriers is marked out for the selected hH phases.

$$\left[\frac{1}{m}\right]_{ij} = \frac{1}{\hbar^2} \cdot \frac{d^2\epsilon}{dk_i dk_j}$$

The flat structure bands define the slowly changing energy function in the reciprocal (here: IBZ FCC, $L\Gamma XU$ path) space. The high value of $\frac{d^2\epsilon}{dk_i dk_j}$, where i, j are denoted to the different directions, determines the low value of the effective mass. However, the described situation is ideal, and multiple different phenomena may take part in the final thermoelectric performance, e.g., band structure resonance [123] or grain boundary scattering [124].

The detailed methodology of effective mass calculations and accordance between the results and literature data are presented in Appendix C.

It is commonly believed that heavy carriers result in good TE characteristics according to the expected higher values of the Seebeck S coefficient [125]. This approach infers that the flat bands in the vicinities of VBM or CBM are favorable. However, this statement was questioned by Pei *et al.* [126]; some examples of hH phases with low effective mass (resulting from steep bands near VBM or CBM) were provided. Also, low-mass carriers were reported for Sb-bearing promising TE candidates [2]. The light carriers, based on the relaxation time DP-derived formula (Chapter 1.4.2), imply a long relaxation time, which leads to the high PF and ZT values.

In order to provide time-relevant TE results, the relaxation time calculated from the DP theory (Chapter 1.4.2) was considered. The relationship between effective mass and relaxation time of carriers for the chosen narrow-gap hH phases [4] is presented in Figure 3.2. One shall notice that the presented relation between effective mass and relaxation time is well employed for the GGA approach. For MBJGGA, however, the relation is

disturbed, and some of the systems, especially those with low values of the effective mass, present deviations from the expected trend. This fact may explain the further discrepancy between the GGA and MBJGGA results.

Comp.	m^p_{GGA}	m^n_{GGA}	m^p_{MBJ}	m^n_{MBJ}	τ^p_{GGA}	τ^n_{GGA}	τ^p_{MBJ}	τ^n_{MBJ}
ScPdBi	0.34	4.80	0.19	0.31	21.5	0.3	46.3	21.5
HfNiSn	0.65	0.75	0.59	0.78	18.5	13.1	18.5	10.8
HfPdSn	0.68	0.60	0.77	0.63	11.2	11.6	8.4	10.0
ZrPdSn	0.52	0.82	0.51	0.96	13.9	6.3	13.2	4.7
NbRuSb	0.32	0.21	0.36	0.22	31.6	64.8	6.1	19.2
TiNiGe	1.37	1.20	1.23	1.05	5.6	5.9	5.9	6.5
VIrGe	0.61	0.54	0.46	0.38	14.0	18.1	20.6	32.6
VFeSb	0.65	0.24	0.49	0.41	14.2	61.5	2.8	2.5
NbFeAs	0.32	1.43	0.33	0.31	39.0	4.2	4.4	6.0
NbIrGe	0.82	0.38	0.82	0.36	8.6	29.3	8.0	30.3
ZrPtPb	0.48	0.19	0.47	0.37	14.8	53.4	14.0	18.0
NbIrSn	0.81	0.39	0.81	0.37	7.8	23.5	7.4	24.1
HfIrSb	0.92	0.59	0.24	1.54	9.7	6.1	64.1	1.3
TiCoBi	0.54	0.56	0.54	1.13	14.2	11.8	13.3	3.8
TaRuAs	0.36	0.23	0.44	0.24	33.7	28.6	23.3	68.9
TiPtSn	0.53	0.53	0.65	0.77	13.0	11.6	9.1	6.0
TiRhBi	0.39	0.58	0.55	1.18	18.5	9.1	10.3	2.8
VFeAs	0.39	0.33	0.39	0.36	30.6	39.6	27.1	35.6
TaFeSb	0.38	0.33	0.39	0.40	45.3	51.4	48.6	37.3
TiPtGe	0.44	0.42	0.48	0.47	19.6	19.0	16.0	15.2
HfCoBi	0.54	0.59	0.58	0.40	18.8	13.8	15.2	22.3
TiRhAs	0.32	0.41	0.32	0.42	31.6	20.2	29.8	19.4
TiIrSb	0.35	0.28	0.36	0.27	32.4	41.7	28.8	42.4
TaFeAs	0.34	0.29	0.35	3.01	52.5	65.9	45.6	1.9
VCoGe	0.79	0.46	0.82	0.49	11.0	22.5	9.3	20.1
HfPtGe	0.56	0.44	0.25	1.36	17.6	8.4	53.0	3.4
TaCoSn	0.70	0.44	1.32	0.65	15.7	27.4	5.6	14.0
ZrPtGe	0.47	9.06	0.47	3.83	19.8	0.2	18.3	0.6
NbCoGe	0.58	0.34	0.6	0.35	17.2	33.6	14.0	30.1
TiFeTe	0.56	0.38	0.57	0.5	12.6	20.2	1.8	1.6
TaCoGe	0.69	0.45	0.78	0.46	20.0	32.2	14.2	26.7
TiCoAs	0.70	1.70	0.83	1.57	14.0	2.9	10.3	3.0
ZrRuTe	0.51	0.34	0.24	0.28	11.0	9.8	37.6	29.1
HfCoAs	1.67	1.1	2.84	3.03	4.3	6.6	2.1	1.4

TABLE 3.1: A juxtaposition of effective mass m_{XCF}^{regime} (m_e) and relaxation time τ_{XCF}^{regime} (fs), whereas: XCF = GGA., MBJ (MBJGGA); *regime* = *p*-, *n*-type, calculated for the hH phases considered.

3.3.1 Stable hH phases

In Table 3.1, the values of effective mass and relaxation time for 34 stable hH phases are revealed. Contrary to the band structures presented (Figure 2.1), the order of hH systems presented in Table 3.1 is determined by increasing E_{MBJ}.

The effective mass of carriers m_{XCF}^{regime} and their relaxation time τ_{XCF}^{regime} were considered for p and n-type carriers and for two XC functionals. As a result, for each compound, there were four combinations (p/n-type regime and GGA, MBJGGA parametrizations), not only for effective mass but also relaxation time, and for PF and ZT.

For some systems, the values of the effective mass differ significantly; this fact promotes the particular regime of the carriers. Similar effective mass values for p-type carriers were obtained for similar hH systems in the past, e.g., $m_{GGA}^{p} = 0.26\ m_e$ for ScPtSb [1], m_{MBJ}^{p} for LuPdSb [2], $m_{MBJ}^{p} = 0.22\ m_e$ for LuNiBi [3], $m_{MBJ}^{p} = 0.34\ m_e$ for ZrOsTe [5]. Also, the experimental value of effective mass for NbFeSb was reported by Shen *et al.* to be 1.65 m_e, which falls within the range proposed by both GGA and MBJGGA parametrizations [127]. The significant variations between p and n-type effective mass regimes were revealed for TiCoAs and ZrPtGe. The analog situation may be the result of the different XC functionals applied and could be justified by the local shape of the band structure in the nearest vicinity of VBM or CBM.

The average values of effective mass were 0.60 and 0.62 m_e for the GGA and MBJGGA approaches, respectively. The difference among the whole subset depending on the XC functional used is not significant, however, the range provided by the MBJGGA approach is twice as big as the one realized with GGA. Therefore, only based on the effective mass, one may consider if MBJGGA will provide more variability and deviate from the average PF and ZT results compared to GGA. The complex discussion on TE performance will be realized in the final part of this chapter.

The values of effective mass m_{GGA}^{p} and m_{MBJ}^{p} range from 0.32 m_e (NbRuSb) to 1.67 m_e (HfCoAs) and from 0.19 m_e (ScPdBi) to 2.84 m_e (HfCoAs), respectively. The average values of m_{GGA}^{p} and m_{MBJ}^{p} are equal 0.60 m_e and 0.62 m_e, respectively. In comparison, the value of m_p of NbFeSb was reported to be equal 1.65 m_e by Naydenov *et al.* [128].

The values of effective mass m_{GGA}^{n} and m_{MBJ}^{n} range from 0.19 m_e (ZrPtPb) to 9.06 m_e (ZrPtGe) and from 0.22 m_e (NbRuSb) to 3.83 m_e (ZrPtGe), respectively. The average

values of m^n_{GGA} and m^n_{MBJ} are equal 0.92 and 0.85 m_e, respectively. In comparison, the value of m_n of NbFeSb was reported to be 0.52 m_e by Shen *et.al* [127] and 0.35 by Naydenov *et al.* [128].

ZrPdSn, HfPdSn, and HfNiSn have electronic structures that are ScNiSb-like [1]. m^p_{GGA} and m^p_{MBJ} for ScNiSb were reported to be 0.36 m_e. For ZrPdSn the effective mass for different regimes and XC functional considered are as follows: m^p_{GGA} = 0.52 m_e and m^p_{MBJ} = 0.51 m_e, while for HfPdSn, m^p_{GGA} = 0.68 m_e and m^p_{MBJ} = 0.77 m_e. Effective masses of p-type carriers for HfNiSn are 0.65 and 0.59 m_e for the GGA and MBJ approaches, respectively. The results obtained for hH systems with similar band structures to ScNiSb provided higher m^p, while for ZrPdSn, the discrepancy between GGA and MBJ-derived results was the smallest.

The hH phases exhibiting the ScPtSb direct transition type were very few among the subsets considered. Only ScPdBi (E_{GGA} = 0.07 eV), ZrRuTe (E_{GGA} = 0.93 eV, E_{MBJ} = 1.25 eV), HfPtGe (E_{GGA} = 0.93 eV, E_{MBJ} = 1.02 eV), and HfIrSb (E_{GGA} = 0.66 eV, E_{MBJ} = 0.75 eV) were shown to represent the $\Gamma - \Gamma$ direct band gaps. The effective mass of ScPtSb was reported to be m^p_{GGA} = 0.26 m_e and m^p_{MBJ} = 0.27 m_e [1], whereas the effective mass of ScPdBi, ZrRuTe, HfPtGe, and HfIrSb ranged between 0.34 and 0.92 m_e (GGA) and between 0.19 and 0.25 m_e (MBJ).

In some cases, the effective mass values obtained are unexpectedly high, e.g., ZrPtGe (m^n_{GGA} = 9.06 m_e and m^n_{MBJ} = 3.83 m_e). The reason for the high effective mass may be connected with the local electronic structure of the usual type, as in the HfCoAs case (Figure 2.4).

The relaxation time of carriers varies significantly. In the p-type regime, τ^p_{GGA} ranges from 4.3 fs (HfCoAs) up to 52.5 fs (TaFeAs), whereas τ^p_{MBJ} ranges from 1.8 fs (TiFeTe) up to 64.1 fs (HfIrSb). The mean values of τ^p_{GGA} and τ^p_{MBJ} are 19.5 and 19.2 fs, respectively. In comparison, the relaxation time of hole-like carriers reported for NbFeSb by Naydenov *et al.* was 26.23 fs [128]. In the n-type regime, τ^n_{GGA} ranges from 0.20 fs (ZrPtGe) up to 65.9 fs (TaFeAs), whereas τ^n_{MBJ} ranges from 0.6 fs (ZrPtGe) up to 68.9 fs (TaRuAs). The mean values of τ^n_{GGA} and τ^n_{MBJ} are 22.8 and 16.9 fs, respectively. In comparison, the relaxation time of electrons reported for NbFeSb by Naydenov *et al.* was 247.54 fs. Such a difference may be due to the strongly differing deformation potential obtained here (discussed below).

The obtained values of the relaxation time are, in general, in good accordance with exceptions according to the values of the respective effective masses of carriers. One shall note that the effective mass is only one of the factors to determine τ. The impact

of the elastic constant and DP are crucial and may infer unexpected (due to the effective mass by itself) values of relaxation time (e.g., HfIrSb).

3.3.2 Likely stable hH phases

The values of effective mass and relaxation time for 15 likely stable hH phases are gathered in Table 3.2 [8]. Values of effective mass range from 0.11 m_e for NbRuAs (n-type regime and GGA parametrization) up to 4.23 m_e (n-type regime and MBJ parametrization), while the shortest and longest relaxation times (0.5 fs and 168 fs) were calculated for ScPdAs (n-type regime and MBJ parametrization) and LuNiAs (p-type regime and GGA parametrization), respectively.

Comp.	m^p_{GGA}	m^n_{GGA}	m^p_{MBJ}	m^n_{MBJ}	τ^p_{GGA}	τ^n_{GGA}	τ^p_{MBJ}	τ^n_{MBJ}
TiPdPb	0.65	0.70	0.66	0.64	7.7	6.5	6.9	6.9
TiPdGe	0.61	0.57	0.61	0.57	11.3	10.6	10.2	9.9
VRhGe	1.20	0.21	1.10	0.24	4.6	63.3	4.8	51.0
ZrCoAs	1.02	3.49	1.05	3.31	7.4	1.0	6.6	1.0
ZrRhAs	0.36	0.98	0.30	1.70	28.2	2.4	34.9	2.2
HfPdGe	0.40	0.61	0.31	0.61	27.6	12.5	35.5	11.3
HfRhAs	0.43	0.29	0.28	0.32	26.4	20.1	45.6	14.0
TaRhGe	0.79	0.14	0.83	0.15	11.9	154.9	11.9	129.2
VRuSb	0.53	0.19	0.52	0.23	14.9	73.6	14.4	57.0
ZrNiGe	0.83	0.71	0.60	0.74	13.3	14.0	19.5	11.9
ScPdAs	0.35	3.17	0.20	4.23	26.5	0.9	55.9	0.5
NbRuAs	0.36	0.11	0.37	0.12	24.7	165.9	15.9	67.8
TiNiPb	0.66	0.42	0.67	0.41	11.2	21.3	9.9	20.1
NbRuBi	0.42	0.13	0.52	0.16	16.8	98.5	10.3	10.8
LuNiAs	0.20	4.03	0.18	3.06	168.0	1.6	159.0	2.3

TABLE 3.2: A juxtaposition of effective mass m^{regime}_{XCF} (m_e) and relaxation time τ^{regime}_{XCF} (fs), whereas: XCF = GGA., MBJ; *regime* = p-, n-type, calculated for the hH phases considered.

One shall perceive a visible disproportion between the effective mass of p- and n-type carriers; extremely light carriers, i.e., below 0.16 m_e, were reported for NbRuAs, NbRuBi, and TaRhGe (for GGA and MBJ parametrizations). Such a case may favor hole-like or electron carriers due to the relatively longer relaxation time, e.g., in NbRuAs, VRuSb, TaRhGe, and LuNiAs. The high values of τ are, as expected, obtained for the carriers of the lowest mass, which is consistent with theory (1.4.2) and may be due to the relatively low values of DF combined with the greater elastic constant C_{11}. Finaly, even higher

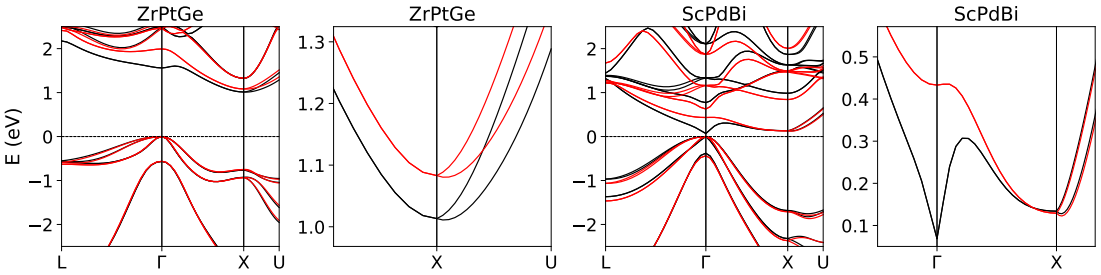

FIGURE 3.3: A comparison of the band structures of ZrPtGe and ScPdBi with close-ups of the vicinities of the CBM.

values of the relaxation time are reported in the literature for hH phases, e.g., for NbFeSb (τ^n = 247.54 fs) [128].

3.4 Deformation potential

In the literature, it is common to perform TE analysis with constant relaxation time as a function of the temperature [129]. However, this approach underestimates the fact that relaxation time is temperature-dependent (Chapter 1.4.2). In order to provide the most reasonable and close-to-fact state calculations, the DP theory was implemented for the relaxation time calculations. This methodology is commonly employed in the literature [130–132].

The values of relaxation time τ are presented in Table 3.1. What is worth mentioning is the fact that τ is dominated by the elastic constant and the DP value, which results in general in good accordance between relaxation time for GGA and MBJ parametrizations. However, at the same time, it may be strongly affected by the GGA parametrization due to the GGA-derived elastic constants.

For each hH system, the four combinations of p/n-type regimes and two XC functionals were calculated. The values of τ provided in this research ranged from 0.2 to 68.9 fs, whereas the literature reports for similar systems indicate the example values of 71.4 fs (ScPtSb), 12.1 fs (ScNiSb) [1] or 91.7 fs (LuPdSb), 33.7 fs (YNiSb) [2] or 10.3 fs (ScNiBi) and 43.6 fs (LuNiBi) [3] for various XC functionals applied.

The shapes of the vicinity of CBM for ZrPtGe and ScPdBi shall be discussed separately due to the very high effective mass of n-type carriers. In Figure 3.3, the electronic structures of ZrPtGe and ScPdBi are shown with a close view of the CBM attached. For ZrPtGe, one would perceive the translation of the minimums of the conduction bands at the X point: one of the bands is located strictly at the X point, while another is shifted

toward the right. This situation occurs for GGA and MBJ parametrizations, affecting the results and the effective mass calculations of both approaches.

In the ScPdBi case, band structures derived from GGA and MBJ vary significantly. The existence of double and shifted local minimum in the conductions bands occurs only for the MBJ approach, while GGA parametrization revealed a tip conduction spike at the Γ point, resulting in the change of the transition type. One shall perceive the specific shape of CBMs for ZrPtGe and ScPdBi and keep this in mind during the further investigation process.

In order to provide the complex analysis of deformation potential (DP or E_β in the particular β direction) for the mentioned hH systems, firstly the comparison of the DP calculations for already known systems was realized. The n-type carriers analysis is provided below. For LuNiSb and LuPdSb, E_β^{GGA} was calculated to be equal 23.1 and 25.5 eV, respectively, while for YNiSb and YPdSb, it is equal 23.3 and 26.1 eV, respectively. The methodology of the DP investigation in VBM applied to the electronic structure obtained with the particular XC functional parametrization was the same in both cases. The justification of the difference between the impact of mechanical deformation on the electronic structure may be due to the specific software performance.

However, this kind of deviation is indispensable, especially due to the strong correlation between E_β and τ. Probably, the reason for the undervaluation of the VASP-derived results compared with the previous Wien2k-derived results for the particular systems is due to the different behavior of the DFT software used when analyzing the hH system with a deformed lattice parameter. This trend of undervaluation of E_β is also realized for different systems: ScNiSb (E_β^{GGA} = 31.7 eV, E_β^{MBJ} = 37.2 eV Wien2k-derived and E_β^{GGA} = 25.59 eV, E_β^{MBJ} = 27.18 eV VASP-derived) and ScPdSb (E_β^{GGA} = 30.4 eV, E_β^{MBJ} = 32.80 eV Wien2k-derived and E_β^{GGA} = 29.0 eV, E_β^{MBJ} = 30.54 eV VASP-derived) [1]; ScNiBi (E_β^{LDA} = 39.7 eV, E_β^{MBJLDA} = 42.7 eV Wien2k-derived and E_β^{GGA} = 29.05 eV, E_β^{MBJ} = 31.18 eV VASP-derived), YNiBi (E_β^{LDA} = 36.8 eV, E_β^{MBJLDA} = 39.7 eV Wien2k-derived and E_β^{GGA} = 25.01 eV, E_β^{MBJ} = 26.96 eV VASP-derived), and LuNiBi (E_β^{LDA} = 36.7 eV, E_β^{MBJLDA} = 39.9 eV Wien2k-derived and E_β^{GGA} = 24.15 eV, E_β^{MBJ} = 26.92 eV VASP-derived) [3]. One shall perceive that observed underestimation of E_β is realized also for LDA and MBJLDA parametrizations, not only GGA and MBJ (MBJGGA) considered.

In Figure 3.4, the relation between DP for CBM and VBM, with XC functionals and values of the band gaps revealed by colors and size of markers, is presented. First of all, one shall visually perceive the smaller differences for GGA-derived results for not-narrow band gap hH systems. The same observation may not be provided for the MBJ approach.

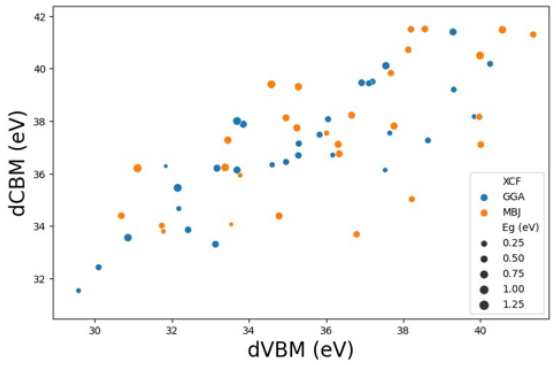

FIGURE 3.4: A comparison of the deformation potentials of the selected hH phases of p- and n-type carriers with XC functional mared with color and the E_g denoted to the size of the marker.

The investigation of DP resulted also in some remarkably high values of MBJ-derived deformation potential E_β^{MBJ} for VBM and CBM, respectively, for three of the 34 hH systems investigated here (not shown here), i.e., NbFeAs (113.89 and 102.74 eV), TiFeTe (101.86 and 119.86 eV), and VFeSb (101.00 and 121.66 eV). Provided E_β^{MBJ} are also significantly larger than the respective E_β^{MBJ} for the similar phases (e.g., HfCoAs: 31.11 and 36.20 eV for VBM and CBM, respectively). Finally, the GGA-derived deformation potentials for the listed systems are clearly smaller than their respective E_β^{MBJ}, i.e., NbFeAs (39.31 and 39.20 eV), TiFeTe (39.29 and 41.40 eV), and VFeSb (36.17 and 36.70 eV for VBM and CBM, respectively). This finding may be considered as a limitation of the MBJ functional application for non-equilibrium calculations. The consequence of remarkably high E_β^{MBJ} may result in a significant overestimation of the TE performance due to the extraordinarily long τ_{MBJ} of the carriers, which must be kept in mind during TE performance analysis.

3.5 Lattice thermal conductivity

In order to provide an investigation of the ZT of the system, a thermal lattice conductivity κ_L analysis must be performed. To obtain the high ZT characterizing good TE materials, κ_L values shall be possibly small (Chapter 1.4). What must be noticed here, is the fact that the modeling of κ_L was done following the Slack's methodology [118], which is, despite its limitations, widely applicable for similar phases.

Comp.	a	$C12$	Volume	κ_L
ScPdBi	6.525	65.93	69.45	72.20
HfNiSn	6.111	73.72	57.05	113.52
HfPdSn	6.360	93.09	64.31	99.54

ZrPdSn	6.396	86.55	65.41	91.21
NbRuSb	6.187	125.22	59.21	76.27
TiNiGe	5.668	95.40	45.52	61.53
VIrGe	5.818	169.88	49.23	38.92
VFeSb	5.788	98.83	48.48	45.43
NbFeAs	5.689	115.02	46.03	63.29
NbIrGe	6.010	156.94	54.27	62.45
ZrPtPb	6.508	90.27	68.91	95.69
NbIrSn	6.230	132.14	60.45	76.60
HfIrSb	6.333	112.19	63.50	112.06
TiCoBi	6.033	75.00	54.90	58.22
TaRuAs	5.972	158.49	53.25	52.81
TiPtSn	6.231	108.25	60.48	65.36
TiRhBi	6.280	93.95	61.92	50.51
VFeAs	5.496	126.62	41.50	44.79
TaFeSb	5.960	98.45	52.93	97.50
TiPtGe	5.991	126.35	53.76	51.50
HfCoBi	6.188	65.63	59.24	102.54
TiRhAs	5.889	128.96	51.06	43.12
TiIrSb	6.165	119.58	58.58	73.10
TaFeAs	5.692	128.43	46.10	69.27
VCoGe	5.512	121.07	41.87	47.04
HfPtGe	6.171	124.52	58.75	72.45
TaCoSn	5.962	96.36	52.98	88.66
ZrPtGe	6.200	119.11	59.58	66.56
NbCoGe	5.698	116.33	46.25	69.23
TiFeTe	5.864	67.43	50.41	60.65
TaCoGe	5.715	125.23	46.74	79.43
TiCoAs	5.605	104.92	44.02	57.09
ZrRuTe	6.298	82.02	62.45	86.20
HfCoAs	5.783	99.48	48.35	76.60

TABLE 3.3: Selected parameters of the considered 34 hH phases: equilibrium lattice parameter a (Å), elastic constants C_{12} (GPa), unit cell volumes (Å^3), and values of the lattice thermal conductivity κ_L (W/mK).

In Table 3.3, the properties connected with Slack methodology are gathered for 34 hH stable phases: lattice parameter a (Å), elastic constant C_{12} (GPa), the unit cell volume of the particular system (Å^3), and lattice thermal conductivity κ_L (W/mK). The process

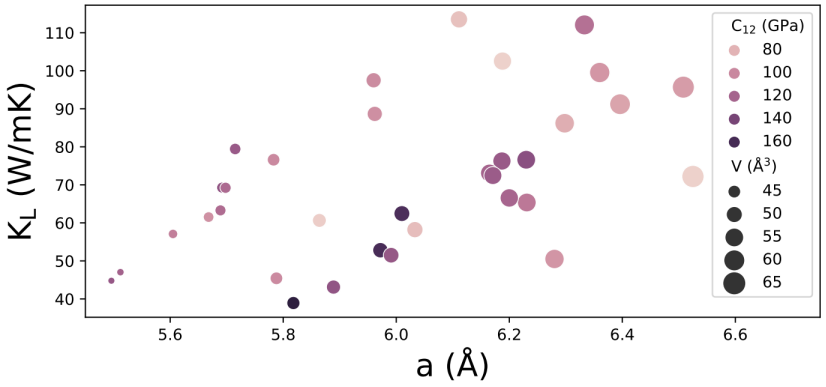

FIGURE 3.5: The relationship between lattice thermal conductivity κ_L (W/mK) and lattice parameter a (Å) with elastic constant C_{12} (GPa) marked with different hue and the volume of the unit cell V (Å^3) presented as the different size of the marker.

of calculation of κ_L is depicted in Figure 3.1. Also, the visualization of Table 3.3 is shown in Figure 3.5.

There is a clear interplay between the cubic lattice parameter and lattice thermal conductivity. Systems with the smallest a are characterized by the lower κ_L values; however, the criterion of the lattice parameter of cell volume is not enough to unequivocally determine systems with the lowest κ_L.

One shall perceive the general trend of increasing C_{12} with an increase in the lattice parameter and, therefore, cell volume. One may disclose the delicate tendency of systems with the biggest C_{12} values to exhibit relatively low κ_L. Another relationship between κ_L and the rest of the properties of the systems is not so obvious.

The possible trends between mass of the particular constituent elements and κ_L were investigated, but no pronounced dependencies were revealed. For some of the hH systems, the high sum of the element constituent leads to a low κ_L (e.g., HfPdSn, HfNiSn), whereas for others the observed tendency is opposite (e.g., HfCoBi, HfCoAs). The only general trends to be considered here are: 1) the decrease of κ_L for heavy Y ions; 2) the increase of κ_L for heavy X and Z ions.

3.6 Thermoelectric performance

There is a commonly held belief that the higher effective mass of the carriers results in a higher Seebeck coefficient and, therefore, better TE performance [125]. However, Pei *et al.* [126] provided an example of the contrary phenomenon, when the lower effective mass resulted in the higher TE performance. Similarly to Pei, it was shown that among the ScMSb systems (M = Ni, Pd, Pt), the lighter the carriers (p-type regime), the higher

relaxation time-relevant PF [1]. It is a high relaxation time to determine the good TE performance, while the τ calculations are more complex than effective mass by itself and include more parameters (e.g., deformation potential).

An example may be the group of selected previously investigated hH systems (LuNiSb, LuPdSb, YNiSb, LuPdSb [2]), whereas the system with the relatively heaviest carriers (YNiSb and its $m = 0.27\, m_e$ both for GGA and MBJ parametrizations) was characterized by having one of the lowest PF in the range 200–1200 K among the similar systems with lighter carriers. Taking into consideration the relaxation time, it was LuNiSb with the longest GGA-derived relaxation time (τ^{GGA} = 76.4 fs) to provide the best PF of 9 mW/K^{2}m at room temperature. However, LuPdSb with even higher MBJ-derived τ revealed much lower PF (especially at room temperature) than LuNiSb, but still - higher than all remaining PF results at high temperatures. Therefore, one shall understand that, despite the provided clear formulas and definitions, there is no one strict tendency or standard procedure for obtaining the best TE performance of the phase with particular parameters. Keeping in mind the above insight, the final analysis of the TE performance is realized below.

3.6.1 Stable hH phases

In Figures 3.6 and 3.7, the comparison of the highest PF and ZT (for the particular concentration of carriers) at 300 and 900 K is revealed. With black and red color, the GGA and MBJ parametrizations are marked, whereas with full dots, the results for the electrons are marked, and with circles, for holes. In the bottom parts of the graphs, the considered values of the carrier concentration *cc* for the particular system, the XC functional, and the regime type are revealed. The disclosed values of the *cc* are chosen to maximize the PF or ZT at the considered temperature, whereas the considered range of *cc* is determined by the reasonable experimental values for the similar phases [133] and is found and applicable in the experimental data concerned about hH phases [134].

The PF and ZT values revealed here are within the expected range of the average TE hH phases. One may consider the proportional relation between PF and ZT for the particular phase, which has a slightly different PF distribution compared to the distribution of ZT.

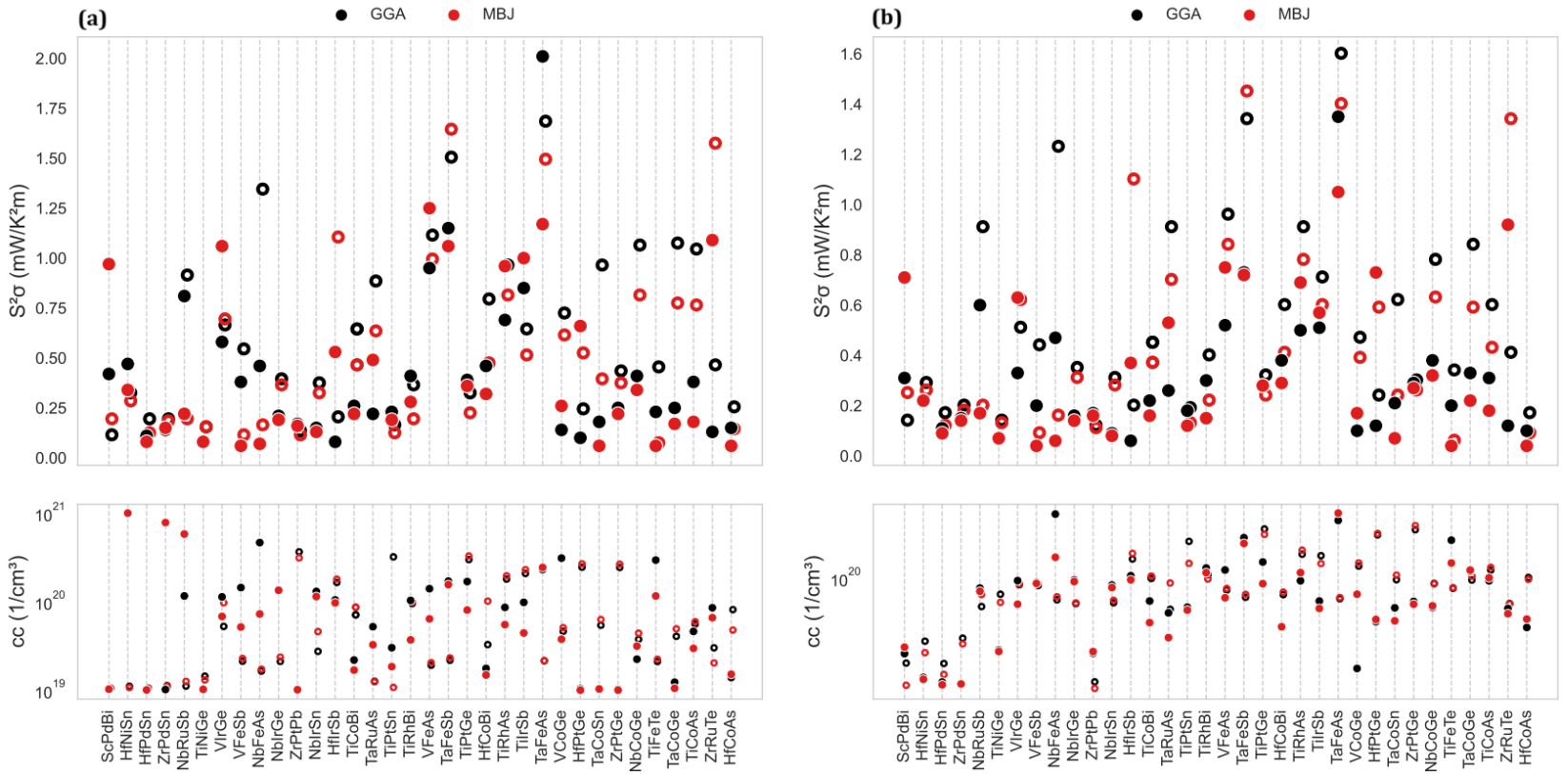

FIGURE 3.6: A comparison of the distributions of PF at (a) 300 K and (b) 900 K for the considered 34 hH phases. The XC functional parametrizations are denoted with black (GGA) and red (MBJ), whereas the carrier types are denoted with the shapes of the markers (full dots for n-type carriers and circles for p-type carriers). In the bottom part of the graph, the respective values of the carrier concentration (of the particular regime and corresponding XC functional applied) are marked.

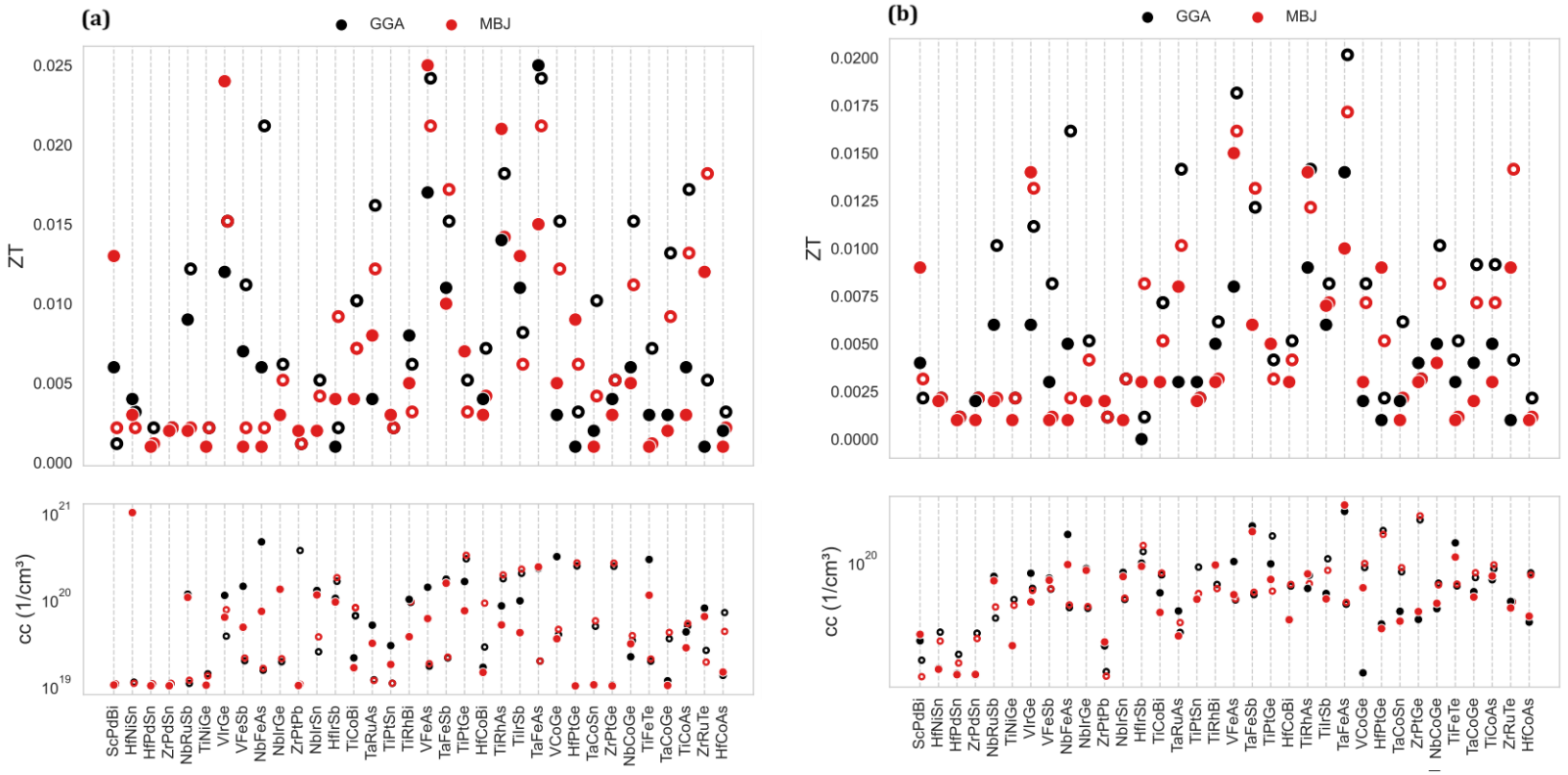

FIGURE 3.7: A comparison of the distributions of ZT at (a) 300 K and (b) 900 K for the considered 34 hH phases. The XC functional parametrizations are denoted with black (GGA) and red (MBJ), whereas the carrier types are denoted with the shapes of the markers (full dots for n-type carriers and circles for p-type carriers). In the bottom part of the graph, the respective values of the carrier concentration (of the particular regime and corresponding XC functional applied) are marked.

The highest PF and ZT values were obtained for TaFeAs, TaFeSb, VFeAs, and for TiRhAs (due to the relatively low κ_L). Also, an implication similar to one observed in the TiRhAs case may be observed for VIrGe (MBJ approach).

Among the phases considered here, HfNiSn occurred to be investigated by Downie *et al.* in the past [135], revealing the perfect accordance between experimental PF at 330 K for n-type carriers and disclosed here MBJ-derived PF. Also, the possible enhancement of TE performance shall be considered at least in the HfNiSn case, especially due to the observed discrepancy between our predictions and the very high experiment-derived ZT for various HfNiSn-based materials (above 800 K). What is worth recalling here is the reported negligible ZT for HfNiSn at room temperature [136]. Also, for TaFeSb, the next most valuable high-temperature TE material after HfNiSn, a good alignment is revealed between the reported PF [105] and value provided here.

As another valuable candidate for good TE performance, TaCoSn should be considered. Indeed, the ZT at 300 K for n-type carriers is confirmed by the experiment to be low [137]; however, the p-type regime for this system provides more promising possibilities of good TE performance.

The rest of the systems were poorly investigated in terms of TE potential applications. For example, for ScPdBi, the available experimental reports are focused on electrical transport [138]. Also, HfPdSn and ZrPdSn were investigated in a different field than the TE applications; in the theoretical studies, the electronic structure was analyzed [139] and the full-Heusler counterparts of the particular hH phases were considered in ML models [55].

The overall good accordance between reported PF values and the presented here results of the calculations proves the methodology used (the DFT-based approach combined with the DP theory, the Slack-derived κ_L, and transport modeling applied) to be reasonable for the discussed subject and phases considered.

As was already pointed out, no significantly better hH phases were proposed; however, one shall undoubtedly perceive some useful hints on the further analysis and synthesis of the particular phases. First of all, there is no unequivocal tendency of GGA or MBJ to provide consequently lower or higher PF or ZT values. Therefore, the need for two XC functional considerations in the theoretical examination is justified.

What also shall be considered is the possibility of the experimental enhancement of the TE performance of the particular hH phase. Many physical phenomena are not included in theoretical investigations, e.g., it was already reported for VFeSb that in some cases, the modifications to the microstructure of a crystal may induce a strong increase in ZT due to the significant decrease in thermal conductivity [140].

Another important insight will be the analysis of the preferred type of regime. For PF at 300 and 900 K, but also for ZT at 900 K, it is p-type carriers that provided the highest PF and ZT results (excluding GGA-derived PF for TaFeAs at 300 and 900 K). The realization of the highest PF or ZT values at 300 and 900 K for TaFeSb, TaFeAs, VFeAs, and TiRhAs is in good accordance with expectations made based on the band structures of the mentioned systems. For the valence bands, one shall perceive the steep bands in the vicinities of VBM, which may be a useful hint at the low effective mass of the carriers and, therefore, the long relaxation time that induces the high PF and ZT. However, the matter of PF and ZT is far more complex, and the general induction of better TE performance for systems with heavy carriers is not unquestionably true [126]. The analysis of the effective mass, therefore the steepness of the bands in the vicinities of VBM and CBM, revealed few significant insights. First of all, for TaFeAs, the heavier carriers did not result in greater PF or ZT values; the tendency observed is opposite. For the n-type carriers with GGA-derived analysis, both PF and ZT revealed were the highest for this system. A similar situation is observed for the MBJ approach. This tendency is consistent with the statement postulated by Pei *et al.* that the belief in the better TE performance of the heavy-carrier systems (due to the higher expected Seebeck coefficient) is not a universal axiom.

On the contrary, for TaFeSb for the GGA approach, the p-type regime characterized by the greater effective mass of carriers revealed significantly higher PF and ZT. However, for MBJ-derived results and almost the same effective mass of the electrons and holes, the PF revealed varies significantly. The aspect of the effective mass is without doubt crucial for the analysis of TE performance; however, it is not the only determinant, and the final PF or ZT may strongly differ depending on the various factors.

Similarly, for GGA-derived results for VFeAs, the higher PF and ZT were obtained for heavier p-type carriers. However, for the MBJ approach, the situation is opposite, and the lighter n-type carriers resulted in higher PF and ZT, as it is in the TaFeAs case.

Also for TiRhAs, the revealed tendency of GGA-derived PF and ZT is opposite to PF and ZT calculated with the MBJ approach. For GGA-derived calculations, the p-type regime characterized by the lighter carriers is connected to the higher PF and ZT, while for MBJ-derived results, better PF and ZT are obtained for heavier n-type carriers.

The analysis of DP-derived relaxation time also did not reveal an undeniable relationship between τ and PF or ZT. It is expected, due to the PF formula, that the longer the relaxation time of the carriers, the higher the PF and, consequently, also the ZT. Such a tendency is in fact observed for TaFeAs both for GGA- and MBJ-derived results; the longest relaxation time (GGA approach) of n-type carriers resulted in the highest PF and ZT considered here for this system. However, for VFeAs, the n-type regime with

the longest relaxation time is characterized by the lowest PF and ZT compared to the MBJ-derived results and hole-like carriers. Also, for TaFeSb, it is not the p-type MBJ-derived system with the longest relaxation time to be connected to the highest PF and ZT obtained for this phase. Just like TiRhAs, it is the system with the shortest relaxation time that revealed the best TE performance.

In the comparison of the PF and ZT results at 300 and 900 K, first of all, one shall perceive that the increase in temperature does not unequivocally lead to the enhancement of thermoelectric performance, neither for PF nor for ZT. In general, the range of PF and ZT at higher temperatures results in a narrower PF and ZT range. Also, the difference among the carrier concentration distributions for both PF and ZT considered at higher temperatures is visible.

PF and ZT were revealed at 900 K compared to 300 K, e.g., TaFeAs (ZT up to 0.025 at 300 K vs. ZT up to 0.020 at 900 K), ScPdBi (possible ZT greater than 0.010 at 300 K and smaller than 0.010 at 900 K), and ZrRuTe (PF equals 1.5 mW/K^{2}m at 300 K and PF $<$ 1.4 mW/K^{2}m at 900 K). Such a phenomenon is consistent with the relaxation time formula, in which the τ is inversely dependent on the temperature (Chapter 1.4.2), whereas the smaller the relaxation time, the smaller PF and ZT. The modification of the other temperature-relevant factors may not fully balance the decrease due to the shorter relaxation time at higher temperatures. However, for some systems, the higher temperature leads to comparable thermoelectric performance, e.g., TaRuAs (for p/n-type regimes and for both XC functionals considered).

Comp.	$\mathbf{PF}_{GGA}$	$\mathbf{PF}_{MBJ}$	$\mathbf{ZT}_{GGA}$	$\mathbf{ZT}_{MBJ}$
TaFeAs	1.67^{p}, 2.01^{n}	1.48^{p}, 1.17^{n}	0.024^{p}, 0.025^{n}	0.021^{p}, 0.015^{n}
TaFeSb	1.49^{p}, 1.15^{n}	1.63^{p}, 1.06^{n}	0.015^{p}, 0.011^{n}	0.017^{p}, 0.010^{n}
VFeAs	1.10^{p}, 0.95^{n}	0.98^{p}, 1.25^{n}	0.024^{p}, 0.017^{n}	0.021^{p}, 0.025^{n}
TiRhAs	0.95^{p}, 0.69^{n}	0.80^{p}, 0.96^{n}	0.018^{p}, 0.014^{n}	0.014^{p}, 0.021^{n}

TABLE 3.4: hH systems with the best predicted thermoelectric performance revealed, based on the PF (mW/K^{2}m) and ZT at room temperature. With indexes $^{regime=p,n}$, the corresponding type of the carriers is denoted, whereas the XC functional parametrization used is marked in the lower index (PF, ZT and $_{GGA,MBJ}$).

In Table 3.4, the summary of the favorable hH systems with the best thermoelectric performance calculated at 300 K is presented. As was already presented in Figures 3.6 and 3.7, most of the systems are characterized by relatively low PF values (i.e., below 0.5 mW/K^{2}m) for both regimes considered. One shall note the possibility of the poor (compared to the *explicit* calculations) Slack modeled κ_L. Notwithstanding, the PF calculated here reveals very good TE candidates (Table 3.3). Four out of the 34

hH systems presented in this table were disclosed as the most promising phases for TE performance at 300 K, taking into consideration the employed doping (p/n-type regimes) and two XC functionals applied. The findings presented are in fact lower than TE performance for the best hH systems known [112, 127, 152]. However, such a summary of the whole research process shall clearly encourage the investigation and synthesis of Fe-, and As-bearing hH phases. In particular, TaFeSb could be interesting due to its NbFeSb-like electronic structure, possible synthesis and promising TE performance [128]. Also, the dominant nature of the Fe-based hH systems among the phases with the highest PF or ZT disclosed here will encourage further investigation of Fe-bearing alloys. It is already well known that NbFeSb and its stunning thermoelectric performance [112, 127, 152] are examples of good Fe-based TE material. However, one shall keep in mind that NbFeSb exhibits ZT and PF, respectively, of 0.4 and 3.3 mW/K^{2}m at 300 K [161]. The presence of As or heavy, metallic elements shall not discredit the system as the TE candidate.

On the other hand, the MBJ-derived TE performance for the discussed systems may be biased by the extraordinary long relaxation time of the carriers. An example of such a situation shall be considered in the ZrRuTe case, where the GGA-derived TE performance is significantly smaller than the corresponding results obtained for MBJ parametrization. However, the careful examination of the electronic structures of ZrRuTe for GGA and MBJ approaches discloses a minute change in E_g with similar shapes of VBM and CBM conserved.

What is also important in the discussion with the previously applied methodology of limiting the considered potentially valuable systems due to the narrow band gap is that all of the presented four hH systems exibit $E_g > 0.35$ eV. The narrowest E_g^{GGA} is revealed for VFeAs, whereas the rest of systems (and VFeAs with MBJ parametrization) exhibit $E_g > 0.70$ eV. This observation shall encourage the investigation of hH systems with band gaps wider than suggested by, e.g., the '10 k_BT rule' [109]. Especially due to the fact that among the hH phases considered here, TaFeAs ($E_g^{GGA} = 0.88$ eV and $E_g^{MBJ} = 0.98$ eV) is the most promising TE candidate.

In the end, it is worth recalling that for some hH systems considered here (e.g., LaPtSb), the band structures may suggest the desired good TE performance shapes of VBM and CBM (due to the light carriers involved). Indeed, the role of the flattening of the conduction bands in $\Gamma - X - L$ direction (without the flattening of CBM) may be the reason for the best TaFeAs TE performance for n-type carriers, due to the high Seebeck coefficient and light carriers. Such features were revealed for Fe-based arsenides, both for p and n-type carriers. In general, Fe-based hH systems are expected to exhibit good TE performance for hole-like carriers due to the relatively high τ.

3.6.2 Likely stable hH phases

In order to provide a sufficient feature space for ML modeling of PF (Chapter 5), the investigation of the TE performance of fifteen likely stable hH phases was performed. Some of those systems were already reported in terms of their potential TE applications.

Based on the properties gathered in Table 3.2 (e.g., long relaxation time for LuNiAs) and taking into consideration the band structures in Figure 2.6 (e.g., possible high Seebeck coefficient for p-type regime due to the presence of additional valence bands below VBM for As- and Ge-bearing phases), some favorable hH compounds are revealed. In case of the degeneracy of the valence bands in the vicinity of VBM, VRhGe and TaRhGe shall be considered (VBM at L and Γ points, respectively).

The distributions of PF and ZT at room temperature for fifteen likely stable hH phases are presented in Figure 3.8 (a) and (b), respectively. With black and red color, the results obtained with GGA and MBJ parametrizations are marked, whereas with dot or circle, the type of carrier is revealed (hole-like carriers: circle; electrons: dot). In the lower part of Figure 3.8 (a) and (b), the carrier concentration for the particular values of PF or ZT is provided.

The majority of hH phases discussed here are characterized by PF and ZT lower than 2 mW/K^{2}m and 0.04, respectively. The considered range of carrier concentration, i.e., from 10^{18} up to 10^{20} cm^{-3}, is feasible to obtain in the experiment. The use of specific XC functionals does not necessarily result in consistently lower or higher PF or ZT. However, one shall perceive that the relatively highest PF was exhibited for n-type regime for the following hH phases: NbRuAs (the highest $PF^n_G GA$ of over 4 mW/K^{2}m), VRuSb, TaRhGe, and VRhGe. For the last three named hH systems, the alignment between GGA- and MBJ-derived PF is very good. Also, LuNiAs exhibit relatively high PF values (similar to GGA and MBJ parametrizations), but for p-type regime. Alloys listed here, i.e., NbRuAs, VRuSb, TaRhGe, VRhGe, LuNiAs, and LuNiSb (order due to the decreasing PF), emerge as promising candidates for TE materials.

Some systems, among the hH phases considered here, were already investigated in terms of potential TE applications. For TiPdPb, relatively low thermal conductivity (0.98 W/mK) and ZT equals 0.64 (1000 K, p-type regime) were revealed [162]. Similar ZT was reported for TiPdGe at 1200 K [162]. Another among the hH phases considered here, ZT^p equals 0.30 (at 300 K) and 0.62 (at 1000 K), was reported for NbRuAs [163]. Relatively high PF and ZT (GGA-derived results for n-type regime) were also revealed here. Also, VRuSb, HfPdGe, and VRGe were analyzed in terms of TE performance [96, 164, 165].

All but one (NbRuAs of numerous valence bands and low effective mass) arsenides considered here, i.e., ZrCoAs, ZrRhAs, HfRhAs, ScPdAs, and LuNiAs, were not investigated as potential TE material candidates. There is a lack of reports on TE performance for TiNiPb and NbRuBi too [63, 166]. There are six novel hH phases, with some exhibiting relatively high PF (i.e., LuNiAs for p-type regime; NbRuBi for n-type regime and GGA parametrization) or ZT (i.e., LuNiAs for p-type regime). Moreover, some As-bearing phases were recently the subject of interest [4, 96, 167–169], which also shall encourage further theoretical and experimental investigation for arsenides and their potential TE application.

The distribution of PF and ZT was also analyzed at 900 K (not shown here). The highest PF equals 1.69 mW/K^{2}m is revealed for n-type regime (GGA parametrization) for NbRuAs. The next highest value of PF is obtained for p-type regime and GGA parametrization for ZrRhAs (1.17 mW/K^{2}m), whereas the rest of the hH systems considered revealed PF $<$ 1.00 mW/K^{2}m for all combinations of XC functional and carrier regime. Importantly, a significant difference is observed for VRhGe, which exhibits good TE performance at 300 K (n-type regime for GGA and MBJ), but at 900 K, PF^n is not favorable any more. The distribution of ZT at 900 K reveals the highest PF one again for NbRuAs, $PF^n_{GGA} = 0.021$. The next highest ZTs were exhibited for p-type regime for ZrRhAs ($ZT^p_{GGA} = 0.014$), VRuSb ($ZT^p_{GGA} = 0.014$, $ZT^p_{MBJ} = 0.013$), ScPdAs ($ZT^p_{MBJ} = 0.013$), and NbRuAs ($ZT^p_{GGA} = 0.013$). The rest of the systems considered here exhibit ZT $\leq$ 0.12 at 900 K.

In the end, one shall perceive the good accordance between GGA-, and MBJ-derived relatively highest PF for hH phases considered here (n-type regime for VRhGe, TaRhGe, VRuSb; p-type regime for LuNiAs). Such a confirmation of the TE performance shall ensure that the listed alloys are good candidates for TE materials.

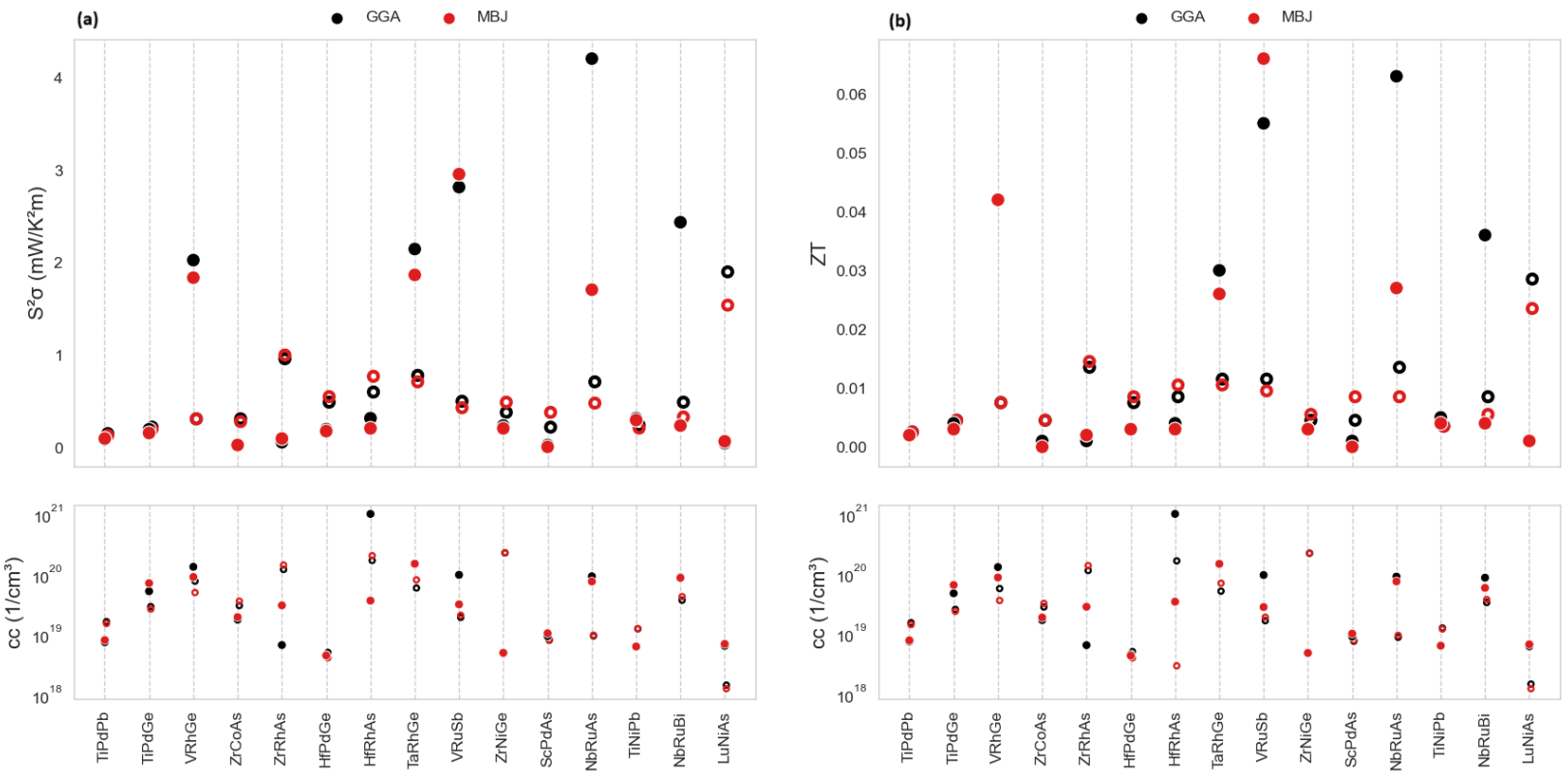

FIGURE 3.8: A comparison of the distributions of (a) PF and (b) ZT at 300 K for the considered hH phases. The XC functional parametrizations are denoted with black (GGA) and red (MBJ), whereas the carrier types are denoted with the shapes of the markers (full dots for n-type carriers and circles for p-type carriers). In the bottom part of the graph, the respective values of the carrier concentration (of the particular regime and corresponding XC functional applied) are marked.

3.7 Conclusions

The high-throughput *ab initio* and BTE calculations performed in this stage of the research resulted in the comprehensive TE analysis of 49 hH phases, including over 30 stable and 6 likely stable hH phases, with no reports on the potential TE performance.

For the research, the two XC functionals were used, two temperatures (300 and 900 K), and p/n-type regimes were considered; the considered range of the carrier concentration is based on the experimental insights. Also, Slack's method of lattice thermal conductivity calculations was implemented, and, PF, the ZT of the 34 hH systems are revealed. The examination of the multiple hH phases considered here is complex and reveals some interesting tendencies for the prediction of novel hH systems. Due to the relatively high PF and ZT at room temperature, the following phases shall be found to be promising TE materials: TaFeAs, TaFeSb, VFeAs, and TiRuAs. Also among the likely stable hH phases, at least two shall arouse interest as a potential TE materials: NbRuBi (n-type regime) and LuNiAs (p-type regime).

What is worth mentioning here are numerous novel As-bearing TE candidates, encouraging the arsenides as a promising family of hH phases to be investigated in the field of TE performance. Recently, other As-bearing hH systems were predicted to exhibit interesting properties [106, 141–143]. Also, for quaternary Heusler phases, some As-bearing systems have already been reported [144]; however, further experimental investigation is required. These reports shall also encourage the examination of As-bearing hH phases, in particular TaFeAs, TaFeSb, VFeSb, TiRhAs, and LuNiAs.

Chapter 4

Machine Learning-Based Predictions of Selected Features

4.1 Introduction

Nowadays, Machnine Learning (ML) methods are commonly used as support for solid state calculations, including studies for hH phases (Chapter 1.5). The main goals of ML in this research were: 1) to provide the initial lattice parameters for all the hH systems to be examined with the use of DFT [4]; 2) to investigate various properties (e.g., band gap) of hH phases as the ML target [7]; and 3) to investigate the TE performance as the ML target [8].

In this chapter, the results of the best-considered Support Vector Machine (SVR) models for crucial properties of hH phases are disclosed, revealing some novel insights ("Machine Learning-Based Predictions for Half-Heusler Phases" [7]).

In Chapter 5, the SVR model with PF considered as a target is discussed [8].

4.2 Computational details

SVR software was implemented in Python 3.10 [145] with the use of the Scikit-learn library [67]. The kernel function used for the SVR model was the Gaussian Radial Basis Function [75]. The C and γ hyperparameters were chosen as defaults after an analysis of the heatmap of the validation accuracy of the *C-gamma* function (not shown here). The feature scaling applied was a Standard Scaler from sklearn, while the cross-validation method was the Leave One Out (LOO). The quantitative accuracy of SVR

models was investigated with the use of the Root Mean Squared Error (RMSE). The elemental properties of the hH phases feature space were taken from the WebElements periodic table (University of Sheffield [146]).

4.2.1 Feature Scaling

In the preprocessing of the initial feature space, the Standard Scaler from Scikit-learn was implemented [67]. The feature scaling is especially important if the values of predictors or targets significantly differ in value, e.g., bulk modulus $B \approx 10^2$ GPa and band gap $E_g \approx 0.5$ eV. The methodology behind the standardizing features of the Standard Scaler is scaling to the unit variance. The formula used for this particular feature scaling is given as follows: $z = (x - u)/s$, where x is a sample, u is the mean of the training set, and s is the standard deviation of the training set, whereas the scaling and centering are performed independently on each parameter in the feature space. An important element of the Standard Scaler is its vulnerability to outliers. One shall expect the significant differences in the order of magnitude among the feature space to affect the whole model stronger than fewer outliers [147].

However, outliers are not the only ones that have a strong influence on the final model. Also, systems with the presence or absence of particular ions may determine the target, especially if there is observed disproportion in the number of phases bearing particular elements between the learning subset and the targets. Therefore, the feature space proposed here (also in Chapter 5) consists of hH systems with various phases considered. Lack of Te-bearing systems in the given target resulted in exclusion of tellurides from the learning subset, even though their TE performance was discussed (Chapter 3).

4.3 Selected SVR models

4.3.1 Feature space and validation

The aim of this stage of research is to implement ML models to support DFT calculations. After a careful investigation and comparison of the various models, the following parameters were determined as targets for SVR prediction:

- lattice parameter a,
- bulk modulus B,
- GGA-derived band gap E_g^{GGA},

- MBJGGA-derived band gap E_g^{MBJ},
- lattice thermal conductivity κ_L.

The train subset was created out of the previously discussed 32 hH stable phases, excluding tellurides (Chapter 3), but with additional 15 hH systems with hull distance (Chapter 1.2.1.3) less than or equal to 0.1 eV. According to Aykol *et al.* [28], such a limitation still indicates stable phases in many cases. The properties of fifteen mentioned hH phases, not discussed earlier, are revealed in the table in Figure 4.1.

The lattice thermal conductivity κ_L was calculated following the Slack's equation [118, 120, 121] (see Figure 3.1).

Comp.	a	B	E_g^{GGA}	E_g^{MBJ}	κ_L
TiPdPb	6.328	103.88	0.35	0.32	55.57
TiPdGe	5.964	131.38	0.62	0.58	45.00
VRhGe	5.796	172.54	0.43	0.75	38.73
ZrCoAs	5.831	147.58	1.20	1.23	68.47
ZrRhAs	6.110	143.97	1.12	1.29	59.94
HfPdGe	6.142	133.71	0.55	0.51	66.63
HfRhAs	6.063	160.02	0.28	0.82	58.39
TaRhGe	5.973	185.13	1.04	1.03	64.25
VRuSb	6.044	165.64	0.19	0.63	42.96
ZrNiGe	5.893	141.57	0.68	0.65	74.56
ScPdAs	6.098	111.31	0.43	0.45	42.58
NbRuAs	5.961	183.13	0.34	0.51	53.07
TiNiPb	6.038	115.66	0.34	0.29	66.00
NbRuBi	6.307	151.77	0.34	0.56	57.56
LuNiAs	5.989	106.94	0.41	0.48	65.65

TABLE 4.1: Table of the additional fifteen hH systems and their parameters (lattice parameter a (Å), bulk modulus B (GPa), band gap $E_g^{GGA/MBJ}$ (eV), lattice thermal conductivity κ_L (W/mK)) with hull distance E_{HD} (OQMD) given as: 0 eV $< E_{HD} <$ 0.1 eV.

A selected subset of 47 hH systems was used as a train subset for ML predictions. The reason for considerations of the Te-bearing stable hH phases taken into account in the previous paper [6] is that the initial set of over 150 systems to be investigated was proposed without any tellurides. Moreover, the lack of two records did not significantly affect the RMSE investigated as a function of the number of samples in the train subset (Figure 4.2).

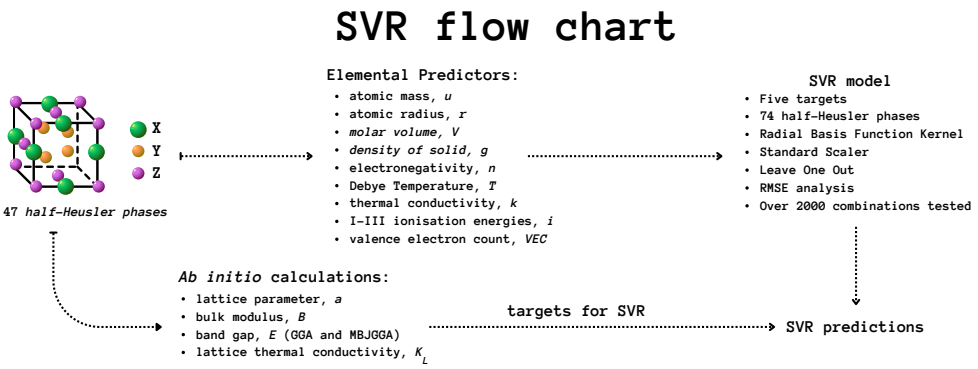

FIGURE 4.1: The illustrative flow chart of the performed SVR modeling.

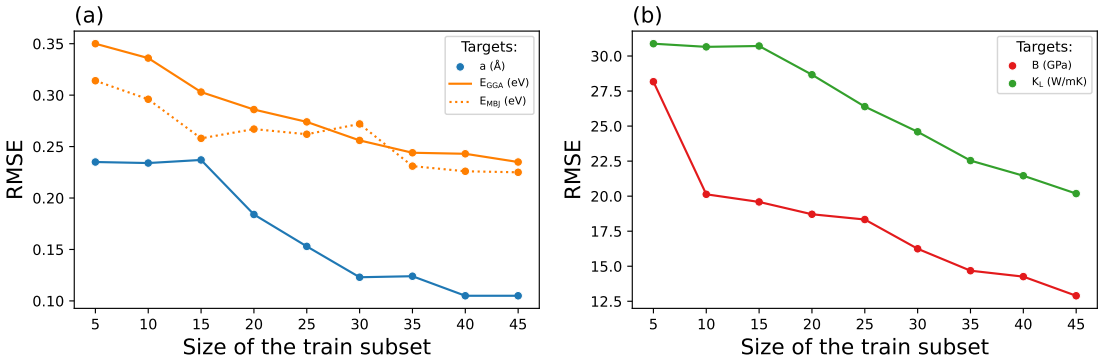

FIGURE 4.2: Learning curves (RMSE as a function of the size of the train subset) of the predictions for the particular targets: (a) a, E_g^{GGA}, and E_g^{MBJ}; (b) B and κ_L. The units of RMSE for the particular values are as follows: a (Å), E_g^{GGA} and E_g^{MBJ} (eV), B (GPa), and κ_L (W/mK).

In Figure 4.1 the flow chart of the whole ML investigation process is depicted.

All five targets (a, B, E_g^{GGA}, E_g^{MBJ}, and κ_L) for the mentioned 47 hH systems to be the learning feature space were calculated with the use of DFT. The 32 systems (and two not included here, tellurides) were already provided in Chapter 3 [6], while the rest of the 47 phases with their parameters are gathered in Table 4.1. The mentioned 47 hH phases were used to train the SVR model, whereas selected properties of the remaining 74 hH phases (out of the initial 121 semiconducting hH systems) were predicted. What is worth emphasizing is the fact that for the predictions of the ternary systems, only the features connected to the elements were used, and only the stable or likely stable due to the OQMD systems were considered.

The predictors used are as follows:

- atomic mass `u`;
- atomic radius `r`;

- molar volume `V`;
- density of solid `g`;
- electronegativity `n`;
- Debye temperature `T`;
- thermal conductivity `k`;
- I-III ionization energies `i(I), i(II), i(III)`;
- Valence Electron Count `VEC`.

For each target, all the possible over 2000 combinations of the predictors were investigated (from the single predictor to the feature space made out of all the eleven predictors), while each predictor was considered as the three values of the particular parameter for the particular *XYZ* site. Therefore, the feature spaces considered ranged from three (a single parameter for each inon in the ternary hH system) to 33 dimensions. The RMSE distribution, with the size of the train subset marked with color, is disclosed in Figure 4.3. One shall perceive that neither the most numerous predictors nor the single predictors provide the lowest RMSE results. The number of combinations is given on the logarithmic scale due to its better clarity. The histograms depicted also reveal that there is no single best combination, and it is not RMSE to unequivocally determine which predictors shall be applied for the particular target.

The greatest RMSE values for all the targets considered were obtained for scarce predictor combinations. On the contrary, the most numerous sets did, in general, provide a lower RMSE. However, by further limitation of predictors, it is shown that for each target, there are still many better combinations than the one gathering all the possible predictors. In fact, for some groups of combinations, the RMSE results were close in value and might be found sufficient for the predictions, depending on the particular validation analyzed. As was already mentioned, the RMSE by itself does not unequivocally determine the best feature space but can be used as a preliminary limitation in the search for the best predictor candidates. Therefore, the best combination of predictors was chosen in two stages: 1) selection of the combinations with the lowest RMSE values; and 2) comparing the calculated-predicted values of targets for the particular combinations of predictors (validation). In Figure 4.4 one can see the juxtaposition of the predicted and calculated values of the particular targets. Due to the LOO used, the SVR predictions were repeated for each of the 47 records as a single target and gathered. In each subplot (a) - (e), there are three different SVR models for selected combinations (out of over 2000 possible combinations) compared.

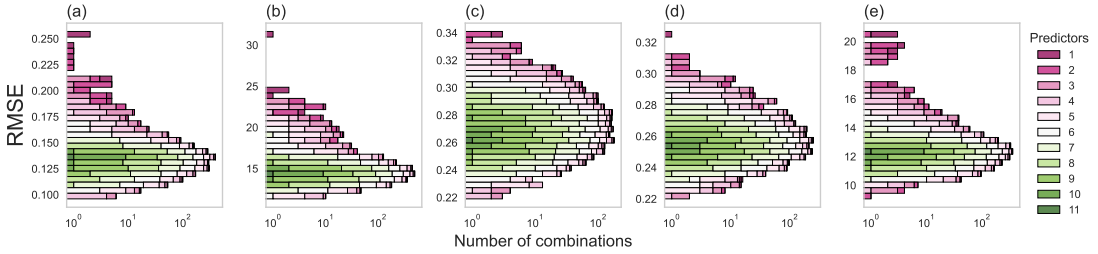

FIGURE 4.3: Histograms with the distributions of the RMSE for all the possible combinations of predictors for the following targets: (a) lattice parameter (Å), (b) bulk modulus (GPa), (c) GGA-derived band gap (eV), (d) MBJGGA-derived band gap (eV), and (e) lattice thermal conductivity κ_L (W/mK). With colors, the number of predictors used is marked.

In Figure 4.2, RMSE values for: (a) a, E_g^{GGA}, and E_g^{MBJ}; (b) B and κ_L predictions in the function of the size of the train subset for the best predictor combinations are depicted. The shapes of the learning curves shall ensure sufficient sizes of train subsets. Especially for a, E_g^{GGA}, and E_g^{MBJ}, the desired plateau for the most numerous of the train subsets is observed. For B and κ_L, no plateau is yet visible; however, the difference between RMSE for the smallest subset and the largest subset regarded is relatively big. Therefore, one may expect, based on the learning curves provided, that all the SVR models considered will provide reasonable predictions for the hH phases studied.

For most of the targets, `i(II)` and `i(III)` are considered significant predictors. This trace might be useful in further ML modeling for similar intermetallic systems. Only for the lattice thermal conductivity (Figure 4.4 (e)) was the `V` to be present in low-RMSE combinations. Such a finding is insightful and consistent with Slack's methodology for the lattice thermal conductivity calculations.

In particular, for the lattice parameter (Figure 4.4 (a)) predictions, predictors `i(II)` and `T` are to occur the most often in the favorable combinations of the predictors (RMSE of 0.1 Å). However, one shall note that `i(II)` and `T` were not sufficient as predictors and did require some additional features to provide predictions with both low RMSE and visual consistency of predicted and calculated lattice parameters. Only the addition of at least one more predictor (e.g., `[u]`, `[i(III)]`, or `[V, u]`) provided the best possible predictions for the model considered. This observation is in agreement with previous discussion, i.e., the analyzed distributions of the RMSE as a function of the number of predictors (Figure 4.3).

For bulk modulus (Figure 4.4 (b)), the crucial predictors were `[i(II), i(III), T]`. In this case, the addition of `u` or `g` leads to predictions with a similar RMSE value (11-12 GPa). However, after the visual analysis, it is `[i(II), i(III), T]` chosen to be the

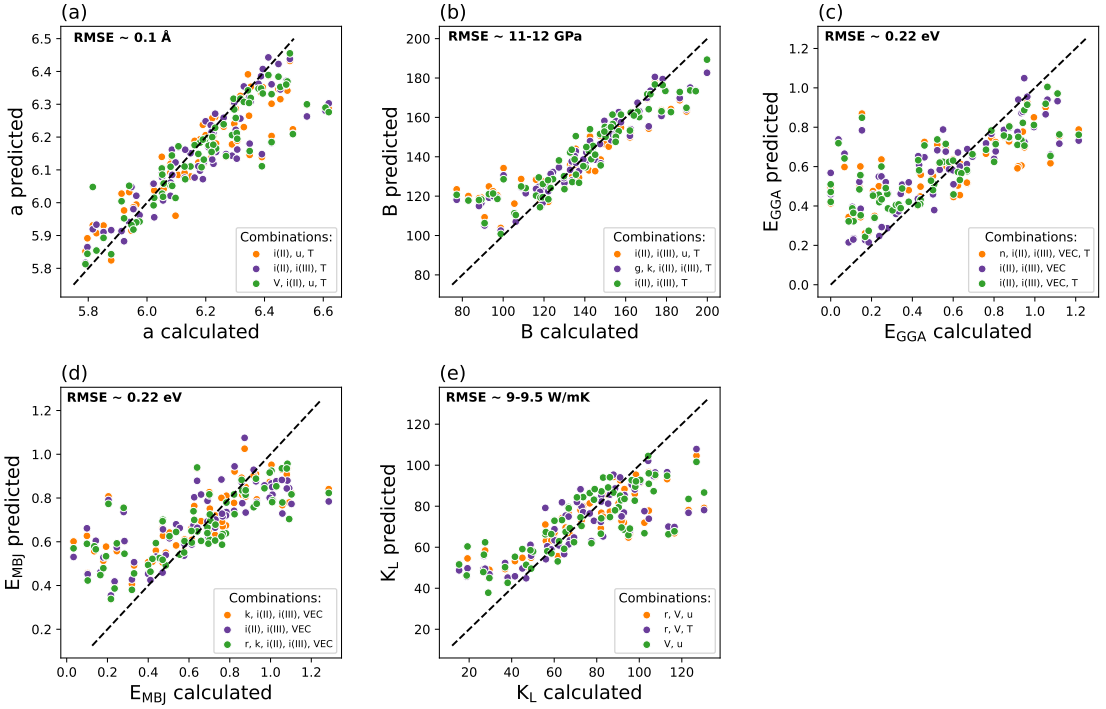

FIGURE 4.4: Predicted and calculated values for the particular targets are: (a) lattice parameter (Å), (b) bulk modulus (GPa), (c) GGA-derived band gap (eV), (d) MBJGGA-derived band gap (eV), and (e) lattice thermal conductivity (W/mK). With color, the favorable predictor combinations for each target were depicted, whereas in the upper left part of each subplot, the considered RMSE range or value denoted.

best. This is an example of when more features may provide even worse results than those for a limited subset.

In Figures 4.4 (c) and (d), the comparison of predicted and calculated values of the band gaps is depicted. Figure 4.4 (c) is devoted to the GGA-derived results, whereas (d) is to the MBJGGA-derived results. For both parametrizations of targets, the lowest possible RMSE for the discussed models equals 0.22 eV. Also, the favorable predictors were similar. For GGA, the best combinations consisted of `[i(II), i(III), VEC]` whereas, in the lattice parameter case (Figure 4.4 (a)), they were not sufficient. The best combination for E_g^{GGA} predictions included also `T`. The situation observed for E_g^{MBJ} predictions is analogous, but instead of `T`, it has been `r, k` to be considered. This difference in the predictors favorable for GGA and MBJGGA approaches may be due to the particular MBJ formula [47]. What is also worth mentioning in the band gap case is the significance of the `VEC` predictor. The electronic band structure is strongly related to the distribution of the valence electrons of the particular element constituent among the crystal structure, depending on the site occupied.

The last target considered is lattice thermal conductivity. Apparently, the lattice thermal conductivity revealed via the Slack method is not strictly correlated to the thermal

conductivity of the particular element constituents. The most often occurring in the low-RMSE (9-9.5 W/mk) combinations is `V` instead. Also, `u, T, r` were considered; however, the most favorable combination is `[V, u]` with comparable RMSE but fewer predictors.

The final favorable combinations of the predictors for the particular targets are given below:

- a: `[V, i(II), u, T]`;
- B: `[i(II), i(III), T]`;
- E_g^{GGA}: `[i(II), i(III), VEC, T]`;
- E_g^{MBJ}: `[r, k, i(II), i(III), VEC]`;
- κ_L: `[V, u]`.

4.3.2 Results of the SVR-derived predictions

While in Figure 4.4 the train and test subsets (47 stable hH systems) are included, in Table 4.2 the final predictions of target features for 74 hH systems are gathered. The majority of these systems have already been comprehensively investigated and are present in the literature. Some of the predictions for systems revealed in the table in Figure 4.2 are discussed and compared to the available data below.

The analysis of the predictions for germanides indicates promising results. For the cubic HfNiGe, Adetunji *et al.* [101] revealed information about the following parameters: a of 5.861 Å, B of 143.1 GPa, and E_g of 0.61 eV. Those values are in good accordance with the predictions provided in this work, even though there is an indirect $\Gamma - X$ band gap in the electronic structure of HfNiGe. Also, they are consistent in value with the RMSE values obtained for the particular targets (Figure 4.4). At the same time, NbRhGe Popoola *et al.* [148] reported a much larger band gap than calculated here. Such an underestimation of the predictions may be due to the indirect $L - X$ band gap of NbRhGe.

Comp.	a	B	E_g^{GGA}	E_g^{MBJ}	κ_L
HfNiGe	5.893	151.53	0.74	0.70	79.52
HfRhBi	6.331	128.63	0.64	0.76	86.65
HfNiPb	6.175	129.51	0.46	0.48	94.83
HfRhSb	6.284	138.78	0.65	0.78	104.50
HfPdPb	6.353	124.08	0.39	0.39	92.69

HfPtSn	6.348	143.19	0.69	0.82	95.28
HfPtPb	6.369	138.14	0.62	0.70	92.82
HfCoSb	6.028	134.71	0.97	0.96	101.62
LuNiSb	6.142	118.59	0.45	0.53	86.67
LuPdSb	6.300	118.32	0.39	0.42	90.92
LuNiBi	6.185	117.78	0.47	0.57	83.54
NbRhGe	5.942	176.72	0.78	0.88	53.10
NbOsAs	5.992	173.71	0.42	0.59	57.95
NbOsBi	6.319	153.33	0.46	0.53	73.17
NbRhSn	6.195	152.96	0.62	0.78	70.38
NbRhPb	6.317	142.94	0.58	0.67	67.46
NbIrPb	6.317	162.40	0.58	0.64	79.63
NbCoSn	5.940	150.13	0.81	0.92	74.59
NbCoPb	6.104	141.06	0.73	0.73	73.26
NbOsSb	6.228	162.70	0.43	0.52	83.18
NbFeSb	5.932	160.15	0.62	0.74	74.12
NbFeBi	6.144	145.50	0.62	0.70	66.30
ScNiAs	6.048	126.16	0.71	0.69	58.06
ScNiSb	6.172	111.29	0.60	0.59	66.83
ScNiBi	6.239	106.29	0.56	0.58	68.6
ScPdSb	6.348	100.79	0.34	0.34	66.58
ScPtSb	6.333	120.26	0.58	0.64	69.62
TaRhSn	6.131	162.94	0.82	0.89	87.23
TaRhPb	6.206	155.14	0.75	0.76	84.45
TaIrGe	6.015	189.33	0.80	0.85	69.30
TaIrSn	6.159	172.90	0.75	0.79	89.15
TaIrPb	6.212	164.16	0.71	0.70	86.42
TaRuSb	6.108	173.42	0.46	0.64	93.97
TaRuBi	6.195	161.39	0.49	0.61	79.00
TaOsSb	6.165	164.87	0.51	0.59	94.12
TaCoPb	6.086	153.94	0.89	0.82	88.35
TaFeBi	6.110	156.66	0.76	0.78	84.33
TiNiSn	5.918	124.13	0.43	0.49	62.46
TiPdSn	6.200	114.38	0.43	0.46	57.02
TiPtPb	6.342	128.13	0.57	0.60	72.91
TiCoSb	5.843	135.62	0.92	0.92	61.96
TiRhSb	6.110	135.24	0.66	0.83	59.22
TiIrAs	5.952	171.78	0.72	0.94	51.43
TiIrBi	6.258	144.95	0.63	0.82	67.39

VCoSn	5.813	150.09	0.57	0.82	50.27
VRhSn	6.018	152.80	0.41	0.68	42.65
VIrSn	6.052	171.75	0.38	0.65	55.34
VRuAs	5.844	176.39	0.24	0.73	37.81
VOsSb	6.051	163.10	0.32	0.60	59.10
VRuBi	6.183	154.00	0.27	0.63	46.24
VOsAs	5.854	173.33	0.32	0.65	44.98
VOsBi	6.200	155.11	0.36	0.60	60.37
VCoPb	6.004	142.22	0.53	0.62	56.36
VRhPb	6.175	143.60	0.40	0.59	47.93
VIrPb	6.192	161.41	0.41	0.61	62.40
VFeBi	6.052	150.48	0.41	0.64	51.61
YNiAs	6.058	124.92	0.53	0.54	58.54
YNiSb	6.157	121.03	0.49	0.55	66.32
YNiBi	6.209	120.66	0.48	0.57	67.77
YPdAs	6.111	121.33	0.42	0.49	49.56
YPdSb	6.290	118.01	0.35	0.45	65.94
YPtSb	6.276	128.57	0.51	0.59	69.09
ZrNiSn	6.072	123.54	0.48	0.52	85.14
ZrNiPb	6.177	119.30	0.42	0.46	82.71
ZrPdGe	6.149	130.13	0.63	0.55	62.95
ZrPdPb	6.455	110.42	0.39	0.38	82.90
ZrPtSn	6.389	130.93	0.71	0.84	89.55
ZrCoSb	6.014	127.17	1.00	0.93	87.32
ZrCoBi	6.155	119.47	0.91	0.84	78.01
ZrRhSb	6.307	126.79	0.76	0.82	92.14
ZrRhBi	6.384	118.40	0.71	0.77	74.73
ZrIrAs	6.110	160.96	0.85	0.94	66.41
ZrIrSb	6.304	147.57	0.76	0.82	96.04
ZrIrBi	6.360	138.67	0.72	0.77	83.56

TABLE 4.2: Predicted values of the following targets: lattice parameter a (Å), bulk modulus B (GPa), band gap with GGA parametrization E_g^{GGA} (eV), band gap with MBJGGA parametrization E_g^{MBJ} (eV), and lattice thermal conductivity κ_L (W/mK).

The predictive power and limitations of ML modeling for the particular types of transitions in the electronic structure will be investigated in the future.

If it is about the arsenides, the predictions made for ScNiAs were very close to the literature data. Jaishi *et al.* [149] revealed a of 5.84 Å and E_g values of 0.48 (GGA) and

0.52 eV (MBJGGA), which are similar to the parameters disclosed here. Surprisingly, the band gap prediction is closer to the literature data than the lattice parameter (difference of 0.2 Å). This fact may be an example of statistical ML behavior; in general, one should expect lattice parameter models to provide better results due to the lower RMSE than for band gap predictions. However, in the singular examples, the deviations may vary strongly.

A variety of types of transitions are characteristic of arsenides. Among the 47 hH systems in the feature space, the majority were characterized by the $L - X$ transition (e.g., ScPdAs, NbRuAs, NbFeAs, VFeAs). Another type of transition is the $L - \Gamma(X)$ for TaRuAs and $L(\Gamma) - \Gamma/X$ for HfCoAs, whereas in brackets, the CBM and VBM obtained with the MBJGGA approach are given. The electronic structure of HfCoAs is exotic compared to the rest of the systems investigated; it is the only phase that, for both XC functionals, revealed CBM located right in between two IBZ points (Γ and X marked as Γ/X).

To summarize, the expectations from the proposed SVR model are to provide the best results for the dominant type of band gap transition (e.g., for arsenides, the indirect $L - X$ transition type). The accordance between SVR predictions and literature data (also for the lattice parameter) is still satisfying and may be due to the fact that there were multiple arsenides in the train-test subset.

The number of bisimides in the learning subset is limited to the four phases only. Among the bisimides, three different types of VBM-CBM were revealed: $L - X$ (NbRuBu), $\Gamma - X$ (TiRhBi, HfCoBi), and $\Gamma - \Gamma(X)$ (ScPdBi). The investigation for HfRhBi by Kangsabanik *et al.* [110] provided the following values of the targets considered: a = 6.41 Å, B = 127.62 GPa, E_g = 0.17 eV, and κ_L = 40 W/mK at 300 K. The accordance between the predictions and literature data for lattice parameter and bulk modulus is very good, while for the band gap there is a strong discrepancy. This fact may be the result of the direct $\Gamma - \Gamma$ band gap of HfRhBi and the lack of similar data in the learning feature space.

Values similar to the lattice thermal conductivity of HfRhBi were obtained by Kangsabanik *et al.* also for ZrIrBi (55 W/mK) and ZrRhBi (30 W/mK). None of the presented predictions for bisimides of the lattice thermal conductivity fall within the bounds of the respective RMSE. In this case, it may be related to the different methodology for providing the desired parameter (Slack's equation vs. phonon spectra). The difference between predicted and calculated band gaps for ZrIrBi (predicted 0.71 eV vs. calculated 0.26 eV) and ZrRhBi (predicted 0.77 vs. calculated 1.02 eV) is significant. SVR seems to yield averaged values far beyond the limits of the RMSE. The explanation for such a discrepancy may be due to a few factors, as follows: 1) the limited number of bisimides

in the learning subset; 2) various band structures; and 3) the generally poor performance of the obtained SVR model for the narrow band gap materials. Notably, there are some better SVR results for bisimides, e.g., TiIrBi, with good accordance for the lattice parameter and bulk modulus predictions. Candan *et al.* [107] reported the lattice parameters ranged from 6.309 to 6.358 Å, depending on the alloy model, and bulk modulus from 104.4 to 123.7 GPa, which is slightly lower than the SVR predictions done. For TiIrBi, even though the type of transition is direct $\Gamma - \Gamma$, the band gap predictions are in good accordance with GGA and MBJGGA-derived results by Candan *et al.* (0.56 and 0.87 eV, respectively). For another system, VRuBi, with an indirect $L - X$ transition type, the accordance between the predictions and DFT-derived results are much better for lattice parameter, bulk modulus, and band gap with two XC approaches considered. Previous calculations revealed the following parameters for VRuBi: a = 6.180 Å, B = 142.5 GPa, E_g^{GGA} = 0.19 eV, and E_g^{MBJ} = 0.50 eV eV [4].

In order to provide better results for bisimides, more Bi-bearing systems shall be included in the feature space, taking into consideration the diversity of the types of transitions in previous DFT calculations.

Also, the antimonides were analyzed here, with various results. For example, the DFT-derived a and B for ScMSb (M = Ni, Pd, and Pt) are in very good accordance with SVR predictions [1]. Also, for the well-known NbFeSb system, the SVR-predicted lattice parameter is in very good accordance with both theory (5.968 Å [112]) and experiment (5.949 Å [111]). Also, E_g of 0.53 eV is close to the 0.62 eV predicted with GGA parametrization [161].

However, not all the results provided for antimonides are well validated with theory or experiment. For NbFeSb only, κ_L SVR-predicted values are higher than values reported. Also, some significant deviations between lattice parameter values that are SVR- and DFT-derived are observed for LuPdSb, YNiSb, and YPdSb. The difference between SVR-predictions and theory (0.2-0.3 Å) for the mentioned phases is beyond the limits of RMSE. Furthermore, the predicted E_g^{GGA} and E_g^{MBJ} of ScMSb, LuNiSb, LuPdSb, YNiSb, and YPdSb are overestimated in comparison to the theoretical values [1–3]. Therefore, such complex predictions may require an extended and more hermetic feature space. Moreover, it is not without significance that the effective mass (at VBM) for these systems is very small, and they may be insufficiently numerous within the learning feature space. Finally, the explanation for such a discrepancy could be due to some extraordinary features of the electronic structure of the systems investigated [1–3, 150, 151]. The antimonides included in the learning feature space are characterized by the $L - X$ transition in most cases (e.g., NbRuSb, VFeSb). The representation of other transition types is poor (e.g., $\Gamma - \Gamma(X)$ of HfIrSb or $\Gamma - X$ of TiIrSb), while the majority

(excluding NbFeSb with $L-X$ and ScPtSb with $\Gamma-\Gamma(X)$ transition types, respectively) of the antimonides compared are characterized by indirect $\Gamma-X$ transitions for both XC functionals considered. The dominance of the $L-X$ transition type in the learning subset may explain the accordance obtained in comparison to the DFT results for NbFeSb. However, the final insight about the particular transition type presence correlation with a better SVR model is not obvious here because some properties for systems of $\Gamma - X$ transition type were also well predicted (e.g., a and B for ScMSb).

Finally, the predicted targets for hH phases from less favorable categories were also compared. For an example, Carrete *et al.* [61] provided κ_L for FeNbP (109 W/mK), CoSbZr (25 W/mK), and NiPbTi (109 W/mK). All those values are strongly different from the values predicted here for particular or similar (e.g., NbFeSb) systems. However, in the VRuAs case, the predicted κ_L value of 37.81 W/mK with a standard deviation of 13% seems to be a reasonable result. Furthermore, the SVR modeling for NbCoSn revealed good consistence with the data reported [152].

4.4 Conclusions

Based on the parameters of the element constituents in the hH phase, five targets were considered. What is worth emphasizing is the fact that the parameters of the ternary system were predicted based only on the elemental features. Only the declared stable and likely stable [25] phases were included for the predictions.

The predictions of the lattice parameter and bulk modulus are, in general, promising and provide very good results compared both to the theory and experiment for the majority of hH phases investigated. The rest of the targets are characterized by results with strongly varying deviations. For some specific electronic structures (e.g., the spectrum of the carrier concentration value for p/n-type carriers or the direct-indirect type of the band gap), the predictions are not reasonable, while for some systems, the predictions are close to reported data. This fact may be the result of the strong effect of the specific combination of elements and the overall electronic structure issue, which is comprehensively discussed above.

The final insight will be that the novel systems may not be the best feature space for complex predictions. The data provided is for sure sufficient for modeling the fundamental parameters as a lattice parameter or bulk modulus; however, more complex quantities, such as the band gap or the lattice thermal conductivity, require more extended or even more hermetic (e.g., bisimides only), but also more versatile (i.e., different transition types considered) feature space.

Such findings clearly confirm that the ML model is only as good (and, therefore, reasonable) as the data it was fed with but has huge potential for DFT support in general.

Chapter 5

Machine Learning-Based Predictions of the Power Factor

5.1 Introduction

Despite numerous ML models to analyze particular features of hH phases (e.g., lattice parameters [7, 56], band structures [58, 59], and thermal conductivity [61–63]), there is limited literature data concerning predictions of the TE performance of these alloys [153].

Similarly to the case of the previously implemented SVR models (Chapter 5), the eleven features of the elements constituent (for each of XYZ ions, separately) were considered as the predictors of the TE performance of the ternary hH system. The number of hH phases used for the train-test subset equals 53 (49 hH phases with $E_{HD} \leq 0.1$ eV (Chapter 2) and four recalculated antimonides [2]), even though the issue of PF or ZT prediction was found highly demanding. Contrary to other targets (e.g., lattice parameter), TE performance was found difficult to predict, and only one SVR model among the sixteen tested was satisfactory (all possible combinations of the following boundary conditions and properties: type of carriers (p/n-type regimes), XCF (GGA or MBJGGA), temperature (300 or 900 K), and finally, PF or ZT considered). The best results, i.e., relatively low RMSE, good validation (also visual), and consistent learning curves, were obtained only for predictions of PF^{p}_{GGA}.

Final predictions exhibited a relatively good representation of qualitative trends among PF^{p}_{GGA} for 70 hH phases.

5.2 Computational details

In the SVR model proposed here, the same methodology (including Feature scaling) was implemented as it was for the previous SVR models (Chapter 4.2).

5.3 Feature space

First attempts to create reasonable SVR models for TE performance predictions were unsuccessful (not shown here) due to the too few records (i.e., hH phases) in the feature space. In order to provide sufficient feature space, the subset of 34 stable hH systems (Chapter 3.6.1) was extended with fifteen likely stable hH alloys [25, 28] (Chapter 3.6.2) and four antimonides of given formula: (Y;Lu)(Ni;Pd)Sb [2] (Appendix B). The proposed set of 53 hH phases was found sufficient for PF^{p}_{GGA} predictions for 70 hH systems; the qualitative trends of the TE performance of the hH alloys considered were recreated and conserved.

Among the created feature space, various ions were included (e.g., bisimides, antimonides, arsenides, germanides) and hH phases with different transition types and band degeneracy (e.g., NbRuAs with indirect $L - X$ transition and HfRhAs with $\Gamma - \Gamma$ direct transition type). The diversity of electronic structures and ion constituents allowed us to propose the universal SVR model for prediction of PF^{p}_{GGA} for hH phases.

The explicit values of PF^{p}_{GGA} for 53 hH systems considered here are revealed in Figure 3.6, Figure 3.8, and Table B.3.

5.3.1 Predictors

The set of eleven elemental features used as the predictors was the same as defined in the previously implemented SVR models (Chapter 4). Considered properties shall be found relevant for ML modeling of various parameters of hH alloys due to the available literature data [7, 62, 63, 154].

For each target taken into account, all possible combinations (over 2000) of the listed eleven elemental features (from 3-dimensional feature space up to 33-dimensional feature space, due to the three XYZ ions in ternary hH phases) were tested for RMSE.

5.3.2 Targets

In order to comprehensively investigate the TE performance of the hH phases considered here, numerous targets were tested. First of all, PF and ZT were to be predicted. Moreover, PF and ZT were tested for: two carrier regimes (electrons and hole-like carriers); two XC functionals (GGA and MBJGGA); and two temperatures (300 and 900 K). The results obtained for GGA parametrization were, in general, slightly better than those provided with the MBJGGA approach. The observations presented here are in agreement with Qu *et al.*, who reported ML predictions (based on the experimental data) of PF significantly better than ZT for the selected TE materials [153]. One shall consider ZT more demanding to be predicted than PF; the result may be due to the difficulties with lattice thermal conductivity predictions (Chapter 4). It is worth mentioning at this point that Narducci *et al.* discussed an estimation of PF as more desirable than ZT in the case of the potential TE application of the particular material [155].

What is also worth mentioning here is the vivid difference in modeling for p and n-type regimes. The attempts to predict the considered here properties of hH alloys in the n-type regime were unsuccessful. Clearly, SVR models implemented for p-type regime were significantly better according to the RMSE, learning curves and final validation. Such an observation leads to the conclusion that the particular applied ML model, i.e., SVR, may be inaccurate for n-type regime predictions.

As the last parameter of TE performance for the considered target, it is temperature equal to 300 or 900 K to be considered; the reasonable SVR models were obtained for the room temperature only. This information may infer some different features required for predictions at higher temperatures. Similarly to the n-type regime case, the reasonable may be examination of the different ML models.

5.4 SVR model validation

In order to determine the best predictors for the target considered, over 2000 combinations of targets (from single-feature up to sets of eleven elemental features) were tested according to RMSE. As discussed in Chapter 5.3.2, only PF^{p}_{GGA} is considered here as the reasonable target for SVR modeling. The distribution of RMSE depending on the number of predictors included in the feature space is depicted in Figure 5.1 (a). One shall note that neither the most numerous nor single-feature subsets of predictors provide the lowest RMSE. In fact, the single-predictor feature spaces (e.g., `i(III)`) exhibited the biggest RMSE. At the same time, there is no single subset of predictors that clearly

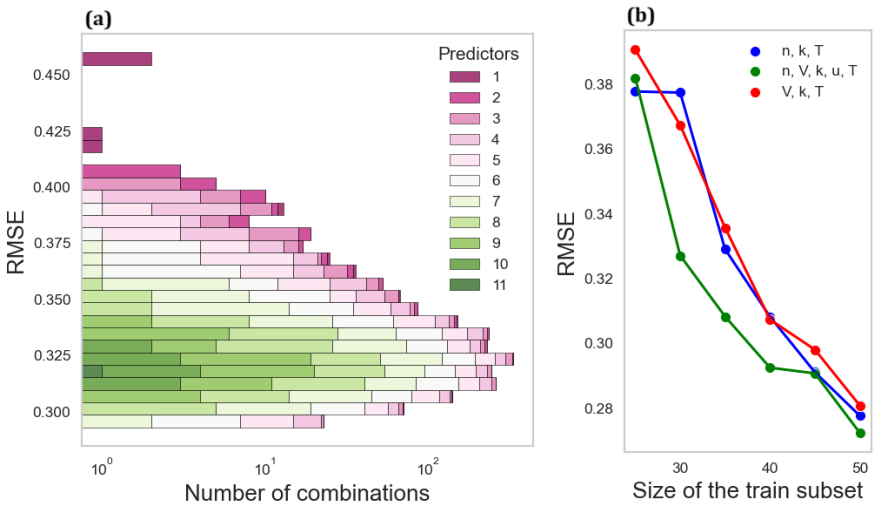

FIGURE 5.1: Parameters and validation of the SVR model. In (a), the distribution of the RMSE of F^p_{GGA} (mW/K^{2}m) for over 2000 combinations of the elemental features, with different colors, and the different number of elemental features (predictors) are marked. In (b), the learning curves for particular subsets of the predictors are: `[n, r, k, i(I), VEC]` (blue), `[n, k, i(I), VEC]` (green), and `[n, i(I), VEC]` (red).

results in the lowest RMSE. Those observations are similar to those made for the different features of hH phases (Chapter 4) and ensure the requirement of testing all possible combinations of predictors.

However, there may be some favorable predictors among the elemental features considered. Namely, for PF^p_{GGA} as the target, over 150 combinations of the predictors with the lowest RMSE (from 0.319 mW/K^{2}m for `[n, r, k i(I), VEC]` to 0.339 mW/K^{2}m for `[g, k, i(III), VEC]`), included at least one of the following features: `i(I)`, `VEC` or `n`. In previously implemented SVR models for E_g predictions, also `i(I)` and `VEC` were found to be significant predictors. These facts may indicate the significance of the named predictors for modeling of various properties of hH phases. One may expect `VEC` to be related to the specific properties or features of the band structures (e.g., shape or number of valence bands). The influence of `i(I)` and `n` could reflect the values of the effective mass and band gap.

In order to arbitrarily choose the subset of predictors used, the minimalization of RMSE and number of elemental features required and the visual validation were performed.

In Figure 5.2 (b), the examples of learning curves (LOO cross-validation) for the particular size of the train subset are presented. With different colors, the different subsets of predictors for PF^p_{GGA} modeling are marked: `[n, r, k, i(I), VEC]` (blue), `[n, k, i(I), VEC]` (green), and `[n, i(I), VEC]` (red). Even though no visible plateau (compare: Figure 4.2) is observed, the presented learning curves shall be considered sufficient due to the significant differences between the least and most numerous train subsets

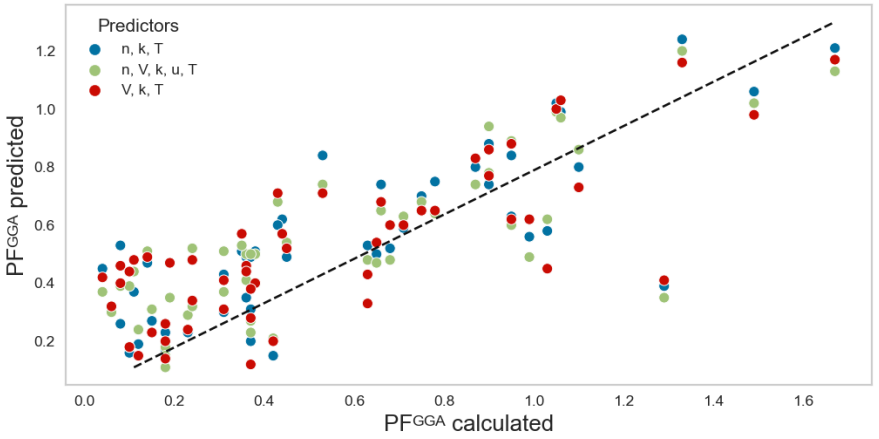

FIGURE 5.2: A comparison of DFT-derived PF^{p}_{GGA} (mW/K^{2}m) and SVR predictions. With different colors, different predictors are marked: `[n, r, k, i(I), VEC]` (blue), `[n, k, i(I), VEC]` (green), and `[n, i(I), VEC]` (red). The dashed line depicts the region of complete validation between predictions and calculations.

considered. The improvement of the model (i.e., lowering of RMSE) with the number of records included in the train procedure is visible. Finally, there is also a number of stable hH compounds to limit both the training and predicted subsets.

The validation of DFT-derived PF^{p}_{GGA} and SVR-based predictions is presented in Figure 5.2. The range of the predicted values of PF^{p}_{GGA} is narrower in comparison to the train-test subset. Due to the LOO approach, the predicted values of PF^{p}_{GGA} were obtained based on the $n-1$ repetitions of SVR modeling. With different colors, the different models are marked, whereas the predictors used are as follows: `[n, r, k, i(I), VEC]` (blue), `[n, k, i(I), VEC]` (green), and `[n, i(I), VEC]` (red). `[n, i(I), VEC]` is chosen as the most favorable subset of predictors according to the minimalization of the number of predictors and RMSE.

One shall note that the distributions depicted in Figure 5.2 indicate the visible consistency for SVR models considered. Namely, for all the cases discussed here, a clear, albeit nonlinear, relationship between DFT-derived results and SVR-based predictions is observed.

As expected due to the poor ability of ML models in general to predict values that deviate strongly and are sparse [70], the greatest discrepancies between SVR- and DFT-based values of PF^{p}_{GGA} were exhibited for the relatively highest PF^{p}_{GGA} values, i.e., LuNiAs (PF^{p}_{GGA} calculated = 1.87 mW/K^{2}m) and LuNiSb (PF^{p}_{GGA} calculated = 1.84 mW/K^{2}m). Notwithstanding, the majority of predictions fall within the RMSE range for favorable combinations of the predictors (e.g., RMSE = 0.319 mW/K^{2}m for `[n, i(I), VEC]`). The SVR modeling may be used as support for qualitative estimations useful in

high-throughput investigations and the search for novel materials. The compounds indicated with this approach would require further exact theoretical studies or experimental examination.

5.5 Predictions of Power Factor for hH Phases

In Table 5.1, the final predictions of PF^{p}_{GGA} obtained with the SVR model are gathered. A subset of predictors is chosen based on: 1) learning curves (Figure 5.1 (b)); 2) validation plots (Figure 5.2); and 3) the smallest possible number of the predictors. Finally, `[n, i(I), VEC]` were chosen as the elemental features to predict TE performance. The possibility of reasonable predictions of complex phenomena as TE performance based on three fundamental properties of the elements constituents shows the strength of ML modeling.

The mean and median values of SVR-based PF^{p}_{GGA} presented in Table 5.1 are equal 0.47 and 0.48 mW/K^{2}m. The range of PF^{p}_{GGA} is from 0.16 mW/K^{2}m for ScPdSb up to 1.11 mW/K^{2}m for LuNiBi.

As previously signaled, the proposed SVR model is favorable (compared to the rest of the 70 hH systems predicted) for some hH systems of remarkably high PF and ZT, e.g., NbFeSb (PF^{p}_{GGA} predicted = 0.83 mW/K^{2}m). The predicted value of PF^{p}_{GGA} for NbFeSb is significantly smaller than the TE performance reported for this phase [111, 112]; however, there is a clear dominance of the PF values for this phase in comparison to the rest of the considered hH compounds. A similar discussion is conducted for two favorable hH phases among the train subset, i.e., LuNiSb and LuNiAs.

Comp.	PF^{p}_{GGA}	Comp.	PF^{p}_{GGA}	Comp.	PF^{p}_{GGA}
HfNiGe	0.40	ScPtSb	0.28	VOsAs	0.73
HfRhBi	0.47	TaRhSn	0.64	VOsBi	0.53
HfNiPb	0.31	TaRhPb	0.43	VCoPb	0.35
HfRhSb	0.55	TaIrGe	0.58	VRhPb	0.38
HfPdPb	0.19	TaIrSn	0.53	VIrPb	0.30
HfPtSn	0.24	TaIrPb	0.35	VFeBi	0.68
HfPtPb	0.18	TaRuSb	0.84	YNiAs	0.90
HfCoSb	0.51	TaRuBi	0.77	YNiBi	0.85
LuNiBi	1.11	TaOsSb	0.77	YPdAs	0.30
NbRhGe	0.34	TaCoPb	0.41	YPtSb	0.37
NbOsAs	0.72	TaFeBi	1.10	ZrNiSn	0.34
NbOsBi	0.53	TiNiSn	0.28	ZrNiPb	0.30
NbRhSn	0.27	TiPdSn	0.19	ZrPdGe	0.22
NbRhPb	0.37	TiPtPb	0.18	ZrPdPb	0.18
NbIrPb	0.29	TiCoSb	0.65	ZrPtSn	0.23
NbCoSn	0.69	TiRhSb	0.52	ZrCoSb	0.51
NbCoPb	0.34	TiIrAs	0.54	ZrCoBi	0.52
NbOsSb	0.60	TiIrBi	0.35	ZrRhSb	0.56
NbFeSb	0.83	VCoSn	0.68	ZrRhBi	0.47
NbFeBi	0.70	VRhSn	0.26	ZrIrAs	0.31
ScNiAs	0.72	VIrSn	0.41	ZrIrSb	0.25
ScNiSb	0.64	VRuAs	0.72	ZrIrBi	0.22
ScNiBi	0.59	VOsSb	0.61		
ScPdSb	0.16	VRuBi	0.49		

TABLE 5.1: SVR-derived values of PF^{p}_{GGA} (mW/K^{2}m) at 300 K based on the `[n, i(I), VEC]` predictors.

The highest PF^{p}_{GGA} of 1.11 mW/K^{2}m is predicted here for LuNiBi, which was indeed reported to exhibit high PF at 300 K (p-type regime) [3, 156]. Another reported high-PF or high-ZT hH phases that were also predicted here as promising TE candidates are: TaFeBi [157], TaOsSb [158], YNiBi [150], TaRuSb [159], VRuAs [167], and ScNiAs [149, 160].

However, one shall keep in mind that some hH phases may prefer (due to the formation energies) and adopt different crystal structures, e.g., YNiAs ($P63/mmc$) [23, 24]. Also, for ScPtSb to be reported as a promising TE candidate [1], the predictions presented here suggest low PF.

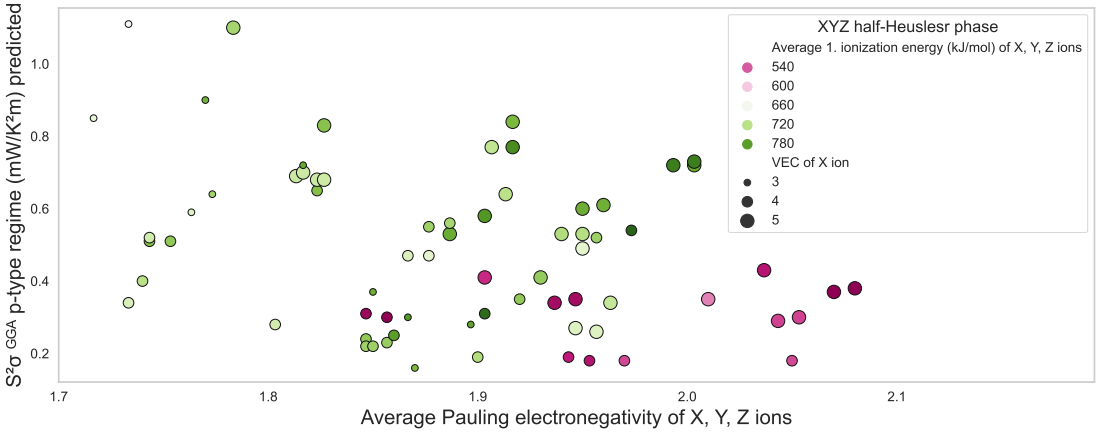

FIGURE 5.3: The distribution of the SVR-predicted PF^{p}_{GGA} for 70 hH phases as the function of the crucial predictors and most significant visually, i.e., average electronegativity `n`, average the first ionization energy `i(I)` (kJ/mol), and `VEC` of X ion.

The rest of the favorable TE candidates among the predicted 70 hH phases (YNiAs, NbOsAs, TaRuBi, and VOsAs) were not investigated in terms of TE performance yet. The recent interest in As-bearing hH phases [4, 96, 167–170], all the more shall encourage further both theoretical and experimental investigation of arsenides.

The relationship between SVR-derived PF^{p}_{GGA} and the best subset of predictors (i.e., `[n, i(I), VEC]`) is presented in Figure 5.3. There are no strict, linear relations between any of the target and elemental features mentioned. However, one shall note some tendencies; e.g., for hH phases with relatively low PF^{p}_{GGA}, the higher the average `n`, the lower the average of the first ionization energy of X, Y, and Z ions. For higher values of PF^{p}_{GGA}, such a trend is not observed.

Additionally, the dominance of the fewer `VEC` of X ions for hH phases with relatively low average `n` is observed. Nonetheless, for some hH systems, the hH compounds with `VEC` of X ion equal to 3 may be observed for relatively higher values of average `n`, i.e., over 1.85. Main insights based on the provided in Figure 5.3 distribution shall ensure the requirement of the non-trival kernel functions [75] used for SVR modeling of the TE performance issue.

5.6 Conclusions

The implementation of the SVR model for analysis of the TE performance (PF^{p}_{GGA} as the target for the most reasonable model) revealed the predictive power of ML for TE materials high throughput investigation. The ability to identify favorable TE candidates

based on the fundamental features only (electronegativity, the first ionization energy, and VEC) of the elements composing those phases was proved here.

Some promising SVR-derived novel TE candidates were revealed here (YNiAs, NbOsAs, TaRuBi, and VOsA), and numerous phases were proposed as interesting subjects for further theoretical and experimental investigation.

Final conclusions

The overall results of the Ph.D. research performed are very satisfactory. The DFT calculations provided the high-throughput investigation among of 150 hH cubic systems. The 121 semiconducting phases were carefully investigated in light of their novelty in the potential TE application. The 49 stable or likely stable hH phases (including over 30 novel) were revealed here and investigated comprehensively, from the electronic structure (Chapter 2), through the TE performance for p/n-type regimes, and GGA/MBJGGA parametrizations at room temperature and 900 K (Chapter 3), finishing with complex ML analysis and predictions of the selected features (Chapter 4) and TE performance (Chapter 5). Additionally, the 15 likely stable hH phases were included in the presented process to extend the required feature space for the ML-based predictions.

The results revealed here provide comprehensive and explicit insight into electronic structure and TE performance in p/n-regimes and for two XC functionals considered (GGA and MBJGGA). The superior transport properties of hH phases directly connected with specific properties of band structures (e.g., numerous bands in the vicinity of VBM or CBM and low effective mass) were investigated and discussed here in terms of the crucial factors to determine good TE material. Also, due to the SVR-derived predictions, the most important factors for high TE performance were investigated and discussed. Although there are some undeniable limitations, a fusion of DFT and ML has the potential to expedite progress in the investigation of novel and promising materials.

Finally, the presented work delivers both solid DFT-based analysis of particular features and trends for numerous hH phases as well as more sophisticated ML-based predictions of the selected properties, especially the potential TE performance. Novel and promising TE candidates revealed here (i.e., TaFeAs, TaFeSb, VFeAs, TiRuAs, ZrCoAs, ZrRhAs, HfRhAs, ScPdAs, LuNiAs, and NbRuBi) shall encourage further theoretical and experimental examination. One shall consider the presence of numerous favorable As-bearing hH phases as the reason for the investigation of arsenides as potential TE materials.

Appendix A

Complete hH Data

A.1 References

In Table A.1, all the semiconducting hH phases from the initial subset of over 150 hH systems considered (with additional tellurides) are disclosed with the references, if available. In Table A.1, also the equilibrium lattice parameters and band gaps from GGA and MBJGGA approaches are gathered.

Comp.	a	E_g^{GGA}	E_g^{MBJ}	Ref.
HfNiGe	5.852	0.52	0.47	[101, 171, 172]
HfPdGe	6.142	0.55	0.51	[63, 164]
HfPtGe	6.171	0.93	1.02	[171, 173]
HfCoAs	5.783	1.29	1.36	[121]
HfCoBi	6.188	0.98	0.92	[102, 121]
HfRhAs	6.063	0.28	0.82	[174, 175]
HfRhBi	6.424	0.07	0.28	[176]
HfNiSn	6.111	0.32	0.27	[101, 177]
HfNiPb	6.210	0.24	0.18	[95]
HfRhSb	6.297	1.08	1.06	[175]
HfPdPb	6.454	0.28	0.23	[95]
HfPtSn	6.380	0.76	0.82	[178–181]
HfPtPb	6.478	0.55	0.63	[96]
HfPdSn	6.360	0.38	0.33	[168]
HfIrSb	6.333	0.66	0.75	[106]
HfCoSb	6.051	1.11	1.08	[88, 121]
LuNiSb	6.269	0.21	0.19	[2, 156]
LuPdSb	6.544	0.11	0.10	[2]

LuNiAs	5.989	0.41	0.48	-
LuNiBi	6.424	0.00	0.03	[156]
NbCoGe	5.698	1.09	1.13	[182, 183]
NbRhGe	5.975	0.79	0.86	[148, 184]
NbIrGe	6.010	0.60	0.72	[184]
NbFeAs	5.689	0.57	0.70	-
NbRuAs	5.961	0.34	0.51	[105]
NbRuBi	6.307	0.38	0.56	[63]
NbOsAs	6.022	0.24	0.44	[63]
NbIrSn	6.230	0.63	0.73	[185–188]
NbOsBi	6.353	0.28	0.46	-
NbRhSn	6.200	0.80	0.78	[188]
NbRhPb	6.295	0.67	0.69	[58]
NbIrPb	6.318	0.67	0.78	[63]
NbRuSb	6.187	0.35	0.48	[159, 189]
NbCoSn	5.964	1.00	1.00	[188, 190–192]
NbCoPb	6.050	0.93	0.82	[14, 58, 63]
NbOsSb	6.232	0.25	0.42	[92, 105]
NbFeSb	5.947	0.53	0.62	[127, 128, 157, 159, 193, 194]
NbFeBi	6.085	0.58	0.71	-
ScNiAs	5.816	0.46	0.47	[149]
ScNiSb	6.107	0.25	0.25	[149]
ScNiBi	6.261	0.15	0.14	[3]
ScPdAs	6.099	0.43	0.45	-
ScPdSb	6.388	0.21	0.22	[1]
ScPdBi	6.525	0.07	0.12	[195, 196]
ScPtSb	6.394	0.43	0.54	[1, 197]
TaCoGe	5.715	1.16	1.19	[182, 183]
TaCoSn	5.962	1.01	1.03	[137, 198, 199]
TaRhGe	5.973	1.04	1.03	[14, 63]
TaRhSn	6.193	0.94	0.93	[18, 199–202]
TaRhPb	6.289	0.92	0.92	[18]
TaIrGe	6.025	0.87	1.03	[199, 203, 204]
TaIrSn	6.226	0.87	1.01	[156, 199, 201, 205]
TaIrPb	6.306	0.91	1.09	[63, 206]
TaFeAs	5.692	0.88	0.98	[63, 93]
TaFeSb	5.960	0.81	0.87	[128]
TaRuAs	5.972	0.37	0.78	[167]
TaRuSb	6.186	0.60	0.77	[18, 159]

TaRuBi	6.307	0.35	0.70	[18]
TaOsSb	6.235	0.51	0.70	[63, 105]
TaCoPb	6.052	0.95	0.87	[63]
TaFeBi	6.080	0.85	1.01	[157]
TiNiGe	5.668	0.63	0.58	[207]
TiNiSn	5.954	0.44	0.40	[89, 149, 177]
TiNiPb	6.038	0.34	0.29	[166]
TiPdGe	5.964	0.62	0.58	[63, 162]
TiPdSn	6.217	0.44	0.41	[208–211]
TiPdPb	6.328	0.35	0.32	[63, 162, 206]
TiPtGe	5.991	0.72	0.91	[212, 213]
TiPtSn	6.231	0.67	0.81	[179–181, 212, 214]
TiPtPb	6.344	0.62	0.66	[63]
TiCoAs	5.605	1.30	1.24	[93, 215]
TiCoSb	5.878	1.05	1.00	[88, 89, 216–219]
TiCoBi	6.033	0.88	0.78	[102, 220, 221]
TiRhAs	5.889	0.77	0.96	[97, 222–224]
TiRhSb	6.148	0.69	0.86	[17, 103, 225, 226]
TiRhBi	6.280	0.66	0.81	[63, 149, 222, 227]
TiIrAs	5.922	0.56	1.06	[228]
TiIrSb	6.165	0.68	0.97	[228, 229]
TiIrBi	6.302	0.43	0.70	[107]
VCoGe	5.512	0.68	0.99	[182, 183]
VCoSn	5.791	0.64	0.88	[230–235]
VRhGe	5.796	0.43	0.75	[14, 199, 236]
VRhSn	6.055	0.44	0.73	[56, 192, 234, 236–240]
VIrGe	5.818	0.27	0.64	[199]
VIrSn	6.080	0.30	0.64	-
VFeAs	5.496	0.36	0.86	[241]
VFeSb	5.788	0.34	0.66	[242, 243]
VRuAs	5.797	0.17	0.70	[163, 167, 244–246]
VRuSb	6.044	0.19	0.63	[189, 245–247]
VOsSb	6.086	0.11	0.58	-
VRuBi	6.181	0.19	0.50	[63]
VOsAs	5.828	0.09	0.61	[63]
VOsBi	6.222	0.11	0.61	[63]
VCoPb	5.913	0.63	0.76	[14, 63, 206, 248]
VRhPb	6.162	0.43	0.76	[14, 63, 206]
VIrPb	6.190	0.32	0.73	[63, 206]

VFeBi	5.939	0.33	0.69	[63, 157, 206, 249]
YNiAs	6.057	0.49	0.55	[250]
YNiSb	6.350	0.27	0.28	[2, 86, 251]
YNiBi	6.497	0.14	0.14	[3, 150, 251–253]
YPdAs	6.391	0.00	0.49	[173]
YPdSb	6.608	0.15	0.17	[2, 86, 255, 256]
YPtSb	6.619	0.00	0.10	[86, 116, 197]
ZrNiGe	5.893	0.68	0.65	[257–259]
ZrNiSn	6.130	0.50	0.47	[177, 260–267]
ZrNiPb	6.226	0.38	0.33	[95, 129, 267–271]
ZrPdGe	6.175	0.60	0.58	[63, 272–274]
ZrPdSn	6.396	0.44	0.42	[51, 187, 275]
ZrPdPb	6.486	0.34	0.32	[14, 95, 271]
ZrPtGe	6.200	1.01	1.08	[98, 212, 276]
ZrPtSn	6.413	0.81	0.88	[179–181, 214, 277–280]
ZrPtPb	6.508	0.67	0.73	[63, 271]
ZrCoAs	5.831	1.20	1.23	[281, 282]
ZrCoSb	6.097	1.06	1.08	[88, 182, 283–285]
ZrCoBi	6.220	0.96	0.97	[99, 100, 102, 265, 286, 287]
ZrRhAs	6.110	1.12	1.29	-
ZrRhSb	6.330	1.12	1.10	[103, 225, 288, 289]
ZrRhBi	6.448	0.95	0.93	[14, 176, 290, 291]
ZrIrAs	6.128	0.15	0.64	[14, 170, 204, 292]
ZrIrSb	6.347	1.21	1.29	[170, 204, 229, 292]
ZrIrBi	6.474	0.04	0.20	[170, 204, 292]
TiFeTe	5.864	0.98	1.18	[293]
TiRuTe	6.116	0.72	0.79	-
TiOsTe	6.161	0.29	0.79	-
ZrFeTe	6.070	1.17	1.22	[294]
ZrRuTe	6.298	0.93	1.25	[295]
ZrOsTe	6.344	-0.05	0.40	-
HfFeTe	6.024	0.86	1.23	[296]
HfRuTe	6.277	0.06	0.46	-

TABLE A.1: Gathered semiconducting 18-electron hH phases are considered in this work with selected parameters (equilibrium lattice parameter a (Å) and E_g (eV) for GGA and MBJGGA parametrizations). In the last column, references to the literature data (up to and including 2022) for the particular hH system are given, if available.

A.2 Thermodynamical stability

In Table A.2, the subset of hH phases among the initial over 120 systems considered that were not (by Q3 2022) comprehensively investigated in terms of the potential TE application. The table was filled with the OQMD-derived parameters to determine the stability of the system (Chapter 1.2.1.3). Due to Aykol *et al.* [28], phases with hull distance E_{HD} up to 0.1 eV can likely be considered stable.

Comp.	ΔH	E_{HD}	Comp.	ΔH	E_{HD}
HfPdGe	-0.832	0.100	TiPtPb	-0.631	0.129
HfPtGe	-0.983	0	TiCoAs	-0.863	0
HfCoAs	-0.828	0	TiCoBi	-0.321	0
HfCoBi	-0.365	0	TiRhAs	-0.912	0
HfRhAs	-0.989	0.017	TiRhBi	-0.531	0
HfNiSn	-0.665	0	TiIrSb	-0.815	0
HfPtPb	-0.863	0.191	TiIrBi	-0.589	0.126
HfPdSn	-0.752	0	VCoGe	-0.391	0
HfIrSb	-0.924	0	VRhGe	-0.456	0.045
LuNiAs	-1.030	0.073	VRhSn	-0.423	0.122
NbCoGe	-0.511	0	VIrGe	-0.451	0
NbIrGe	-0.598	0	VIrSn	-0.427	0.107
NbFeAs	-0.514	0	VFeAs	-0.468	0
NbRuAs	-0.493	0.018	VFeSb	-0.211	0
NbRuBi	-0.149	0.083	VRuSb	-0.285	0.063
NbOsAs	-0.453	0.168	VOsSb	-0.189	0.123
NbIrSn	-0.558	0	VRuBi	-0.168	0.331
NbOsBi	-0.111	0.229	VOsAs	-0.336	0.152
NbRhPb	-0.274	0.129	VOsBi	-0.178	0.522
NbIrPb	-0.341	0.205	VCoPb	-0.125	0.370
NbRuSb	-0.421	0	VRhPb	-0.261	0.351
NbCoPb	-0.114	0.158	VIrPb	-0.349	0.477
NbFeBi	-0.068	0.111	VFeBi	-0.093	0.301
ScPdAs	-1.125	0.084	YNiAs	-1.075	0.133
ScPdBi	-0.836	0	YPdAs	1.203	0.111
TaCoGe	-0.494	0	ZrNiGe	-0.792	0.016
TaCoSn	-0.317	0	ZrPdGe	-0.906	0.135
TaRhGe	-0.551	0.008	ZrPdSn	-0.817	0
TaIrPb	-0.395	0.293	ZrPtGe	-0.996	0
TaFeAs	-0.467	0	ZrPtPb	-0.724	0

TaFeSb	-0.304	0	ZrCoAs	-0.880	0.019
TaRuAs	-0.431	0	ZrRhAs	-1.070	0.063
TaOsSb	-0.364	0.102	TiFeTe	-0.539	0
TaCoPb	-0.168	0.277	TiRuTe	-0.654	0.052
TaFeBi	-0.111	0.225	TiOsTe	-0.600	0.247
TiNiGe	-0.701	0	ZrFeTe	-0.600	0.059
TiNiPb	-0.278	0.043	ZrRuTe	-0.702	0
TiPdGe	-0.723	0.088	ZrOsTe	-0.634	0.208
TiPdPb	-0.379	0.065	HfFeTe	-0.586	0.112
TiPtGe	-0.884	0	HfRuTe	-0.696	0.061
TiPtSn	-0.871	0			

TABLE A.2: Summary of the composition analysis of the selected hH systems, where: ΔH (eV/atom) - hull energy; E_{HD} (eV/atom) - distance from the convex hull, i.e., hull distance.

Appendix B

Validation

B.1 Equilibrium Lattice Parameters

In Table B.1, selected parameters recalculated for (Y;Lu)(Ni;Pd)Sb are gathered. The previously calculated values for the equilibrium lattice parameter a are consistent with the results presented here. The greatest discrepancy was revealed for YNiSb ($\Delta a = 0.28$ Å), whereas the smallest was obtained for YPdSb ($\Delta a = 0.01$ Å).

Such discrepancies may be the result of the different software used (pseudopotentials vs. the full potential approach).

compound	a	B	E_g^{GGA}	E_g^{MBJ}
YNiSb	6.350	93.02	0.27	0.28
YPdSb	6.608	88.15	0.15	0.16
LuNiSb	6.269	97.16	0.21	0.19
LuPdSb	6.544	89.30	0.11	0.10

TABLE B.1: Selected parameters of recalculated hH phases (Y;Lu)(Ni;Pd)Sb: lattice parameter a (Å), bulk modulus B (GPa), and GGA- and MBJGGA-derived band gaps (eV).

B.2 Bulk modulus

The values of bulk modulus B for the selected hH phases are presented in Table B.1. The discrepancies between reported and calculated values of B for YNiSb, YPdSb, LuNiSb, and LuPdSb are as follows: 1.67 GPa, 47.05 GPa, 15.79 GPa, and 1.28 GPa, respectively.

Interestingly, the greater discrepancy of compared values of B is obtained for hH phases, with reported smaller discrepancies between values of a. Therefore, one may assume

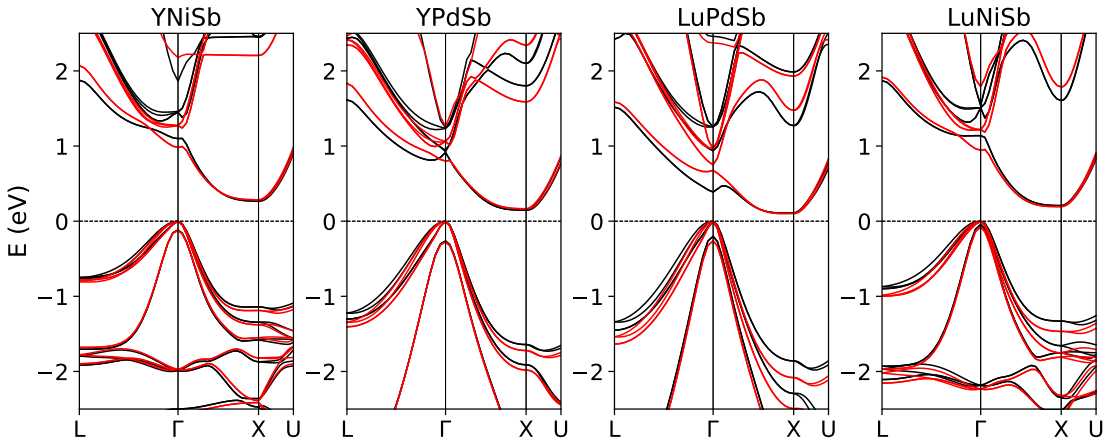

FIGURE B.1: Bandstructures of selected systems, whereas with black and red, GGA and MBJGGA parametrizations are marked, respectively.

that the differences between VASP- and Wien2k-derived B are due to the software used (perturbation theory and energy approach, respectively) rather than to the equilibrium lattice parameter applied.

B.3 Electronic structures

The repetition of the electronic structure calculations with the use of VASP for YNiSb, YPdSb, NbFeSb, LuNiSb, and LuPdSb was performed. The results are depicted in Figure B.1.

The features of electronic structures presented here are consistent with previous results [2]. Even the relatively specific shapes of the band structures are well recreated, e.g., the existence of the local minimum of the conduction band at the Γ point (MBJ approach) for YPdSb or the GGA-derived spike of the conduction band at the Γ point for LuPdSb.

B.4 Band gaps

The values of GGA- and MBJGGA-derived band gaps are gathered in Table B.1. The discrepancies between E_g presented here and previous results range from 0.01 eV (LuNiSb and LuPdSb) up to 0.08 eV (YPdSb) for GGA parametrization and from 0.01 eV (LuNiSb) up to 0.04 eV (YPdSb). The values provided here are highly consistent with the previous data, despite possible deviations in the various parameters of the particular hH phase, e.g., the lattice parameter.

B.5 Deformation potential

The discussion on the discrepancies between VASP- and Wien2k-derived deformation potential is carried out in Chapter 3.4 as the crucial factor for the discrepancies observed in terms of the TE performance.

B.6 Effective mass and relaxation time of the carriers

A complex discussion on the repetition of effective mass calculations is conducted in Appendix C.

The relaxation times of the carriers obtained here with GGA and MBJGGA approaches and for p/n-type regimes are gathered in Table B.2. The smallest discrepancy is observed for YPdSb: $\Delta\tau^{p}_{MBJ} = 5.5$ fs, whereas the greatest discrepancy is revealed for LuPdSb: $\Delta\tau^{p}_{MBJ} = 79.7$ fs. The reason for the presented differences may be due to the strong influence of the elastic constant and deformation potential, whose values differ significantly depending on the software used.

compound	τ^{p}_{GGA}	τ^{n}_{GGA}	τ^{p}_{MBJ}	τ^{n}_{MBJ}
YNiSb	83.8	85.2	1.8	0.8
YPdSb	85.8	86.7	3.8	2.9
LuNiSb	128.5	95.9	2.4	0.5
LuPdSb	9.1	12.0	7.5	8.1

TABLE B.2: Values of the relaxation time τ (fs) e of the carriers at room temperature for selected hH systems with XF functional (GGA or MBJGGA) and regime type (p or n) given.

B.7 Thermoelectric Power Factor

In Table B.3, the values of recalculated PF for selected hH phases are gathered. The discrepancy between the previously obtained PF and the values obtained with the pseudopotential approach is visible; the PF presented here is significantly lower. However, the trend toward favorable hH alloys (i.e., LuNiSb and YNiSb) and the dominant p-type regime is repeated [8].

A reason for such differences may be due to the complex scheme of the τ calculations. Even a small variation in the deformation potential can lead to a significant extension or reduction of τ for the particular compound. A similar effect may be observed due to the relationship between relaxation time and the elastic constant.

compound	PF^{p}_{GGA}	PF^{n}_{GGA}	PF^{p}_{MBJ}	PF^{n}_{MBJ}
YNiSb	0.95	0.07	0.89	0.03
YPdSb	0.51	0.01	0.49	0.01
LuNiSb	1.84	0.06	1.38	0.04
LuPdSb	0.32	0.01	0.35	0.02

TABLE B.3: The maximum TE PF at room temperature for p/n-type regimes and for GGA and MBJGGA parametrizations for the selected hH systems.

Appendix C

Effective mass calculations

The calculations of the effective mass of the carriers were carried out based on the band structures in the vicinity of the VBM (p-type carriers) and CBM (n-type carriers) of the particular systems. The degeneracy of the bands was considered. The final effective mass in the VBM or CBM was calculated as the average value of the effective masses of each band in one (e.g., VBM at the L-point) or two directions (e.g., VBM at the Γ-point), if possible.

In Figure C.1, an example of VBM for ScNiSb located at the Γ point is presented. The *explicit* **k**-mesh points in the considered $L - \Gamma - X - U$ line were fit with the parabola functions. The value of the effective mass of p-type carriers obtained here for ScNiSb is nearly the same as reported in the literature, i.e., 0.36 m_e [1].

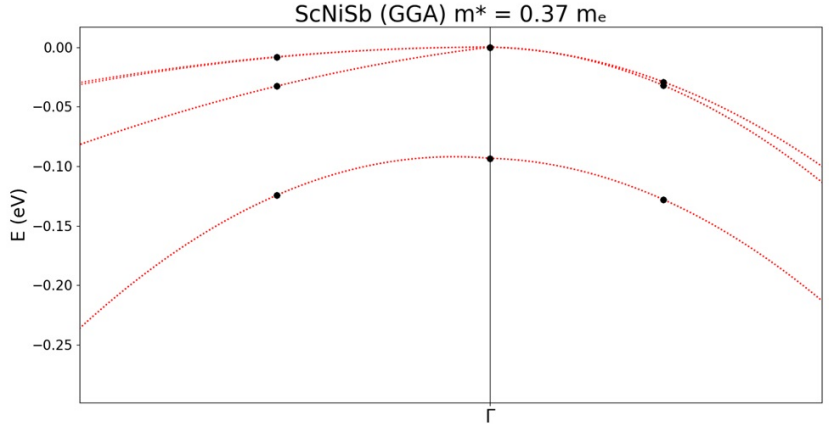

FIGURE C.1: A visualization of fitting **k**-mesh points in the vicinity of VBM for ScNiSb (GGA parametrization).

In Table C.1, the effective mass of hH phases recalculated for SVR modeling is gathered [8]. Listed antimonides were previously investigated in terms of transport and TE properties in the p-type regime with GGA and MBJ approaches [2]. The discrepancies Δm of effective mass between the previous results and values presented here are as follows:

- YNiSb: $\Delta m^p_{GGA} = 0.03\ m_e$, $\Delta m^p_{MBJ} = 0.00\ m_e$;
- YPdSb: $\Delta m^p_{GGA} = 0.00\ m_e$, $\Delta m^p_{MBJ} = 0.01\ m_e$;
- LuNiSb: $\Delta m^p_{GGA} = 0.01\ m_e$, $\Delta m^p_{MBJ} = 0.02\ m_e$.

Much stronger deviation is observed for LuPdSb ($m^p = 0.17$ and $0.15\ m_e$ reported based on GGA and MBJGGA, respectively [2]). Such a discrepancy may be due to the difference between calculations for the full potential approach and pseudopotentials (different software used). Additionally, it is hard to obtain the high accuracy of the second derivative of the total energy of the systems.

compound	m^p_{GGA}	m^n_{GGA}	m^p_{MBJ}	m^n_{MBJ}
YNiSb	0.30	3.58	0.27	5.76
YPdSb	0.20	1.51	0.18	1.70
LuNiSb	0.24	3.00	0.25	7.85
LuPdSb	0.90	0.97	0.65	0.87

TABLE C.1: The effective mass for p/n-type regimes and for GGA and MBJGGA parametrizations for some of the systems investigated here and present in the literature.

Bibliography

[1] Winiarski, M. J., Bilińska, K., Kaczorowski, D., Ciesielski, K. Thermoelectric performance of p-type half-Heusler alloys ScMSb (M= Ni, Pd, Pt) by ab initio calculations. *J. Alloys Compd.* **2018** *762*, 901–905.

[2] Winiarski, M. J., Bilińska, K. High thermoelectric power factors of p-type half-Heusler alloys YNiSb, LuNiSb, YPdSb, and LuPdSb. *Intermetallics* **2019** *108*, 55–60.

[3] Winiarski, M. J., Bilińska, K. Power Factors of p-type Half-Heusler Alloys ScNiBi, YNiBi, and LuNiBi by ab initio Calculations. *Acta Phys. Pol. A.* **2020** *138(3)*

[4] Bilińska, K., Winiarski, M. J. Search for semiconducting materials among 18-electron half-Heusler alloys. *Solid State Commun.* **2023** *365*, 115133.

[5] Bilińska, K., Winiarski, M. J. A theoretical investigation of 18-electron half-Heusler tellurides in terms of potential thermoelectric value. *EPJ B* **2023** *96(10)*, 131.

[6] Bilińska, K., Winiarski, M. J. High-Throughput Exploration of Half-Heusler Phases for Thermoelectric Applications. *Crystals* **2023** *13(9)*, 1378.

[7] Bilińska, K., Winiarski, M. J. Machine Learning-Based Predictions for Half-Heusler Phases. *Inorganics* **2023** *12(1)*, 5.

[8] Bilińska, K., Winiarski, M. J. Machine Learning-Based Predictions of Power Factor for Half-Heusler Phases. *Crystals* **2024** *14(4)*, 354.

[9] `https://en.wikipedia.org/wiki/Heusler_compound`, last accessed: 12.02.2024.

[10] Azzi, S., Belkharroubi, F., Ramdani, N., Messaoud, I. S., Belkilali, W., Drici, L., Blaha, L., Ameri, I., Al-Douri, Y., Bouhemadou, A. Investigation of optoelectronic properties of half-Heusler KZnN and KZnP compounds. *Rev. Mex. de Fis.* **2023** *69(6)*, 060501-1.

[11] Dubey, S., Abraham, J. A., Dubey, K., Sahu, V., Modi, A., Pagare, G., Gaur, N. K. DFT study of RhTiP half Heusler semiconductors: Revealing its mechanical, optoelectronic, and thermoelectric properties. *Phys. B: Condens.* **2024** 672(1), 415452.

[12] Sudharsan, J.B.; Srinivasan, M.; Elavarasan, N.; Ramasamy, P.; Fujiwara, K. Ferrimagnetic half Heusler alloys for waste heat recovery application-First principle study using different exchange–correlation functionals. *J. Magn. Magn. Mater.* **2023**, *588*, 171409.

[13] Setyawan and Curtarolo, DOI: 10.1016/j.commatsci.2010.05.010.

[14] Gautier, R., Zhang, X., Hu, L., Yu, L., Lin, Y., Sunde, T. O., Chon, D., Poeppelmeier, K. R., Zunger, A. Prediction and accelerated laboratory discovery of previously unknown 18-electron ABX compounds. *Nat. Chem.* **2015** *7(4)*, 308-316.

[15] Douglas, J. E., Chater, P. A., Brown, C. M., Pollock, T. M., Seshadri, R. Nanoscale structural heterogeneity in Ni-rich half-Heusler TiNiSn. *J. Appl. Phys.* **2014** *116(16)*.

[16] Kandpal, H. C., Felser, C., Seshadri, R. Covalent bonding and the nature of band gaps in some half-Heusler compounds. *J. Phys. D: Appl. Phys.* **2006** *39(5)*, 776.

[17] J. Yang, H. Li, T. Wu, W. Zhang, L. Chen, J. Yang. Evaluation of half-Heusler compounds as thermoelectric materials based on the calculated electrical transport properties. *Adv. Funct. Mater.* **2008** *18*, 2880.

[18] Hoat, D. M. Electronic structure and thermoelectric properties of Ta-based half-Heusler compounds with 18 valence electrons. *Comput. Mater. Sci.* **2019** *159*, 470–477.

[19] Liu, Z., Guo, S., Wu, Y., Mao, J., Zhu, Q., Zhu, H., Pei, Y., Suu, J., Zhang, Y., Ren, Z. Design of high-performance disordered half-Heusler thermoelectric materials using 18-electron rule. *Adv. Funct. Mater.* **2019** *29(44)*, 1905044.

[20] Zeier, W. G., Anand, S., Huang, L., He, R., Zhang, H., Ren, Z., Wolverton, C., Snyder, G. J. Using the 18-electron rule to understand the nominal 19-electron half-Heusler NbCoSb with Nb vacancies. *Chem. Mater.* **2017** *29(3)*, 1210–1217.

[21] Born, M. On the stability of crystal lattices. I. *Proc. Cambridge Philos. Soc.* **1940** *36*, 160.

[22] Milstein, F., Hill, R. Divergences among the born and classical stability criteria for cubic crystals under hydrostatic loading. *PRL*, **1979** *43(19)*, 1411.

[23] S. Kirklin, S., Saal, J.E., Meredig, B., Thompson, A., Doak, J.W., Aykol, M., Rühl, S., Wolverton, C. The Open Quantum Materials Database (OQMD): assessing the accuracy of DFT formation energies. **Npj Comput. Mater. 2015** *1*, 15010.

[24] Saal, J. E.; Kirklin, S.; Aykol, M.; Meredig, B.; and Wolverton, C. Materials Design and Discovery with High-Throughput Density Functional Theory: The Open Quantum Materials Database (OQMD). *JOM* **2013** *65*, 1501–1509.

[25] `https://www.oqmd.org/`, last accessed 28.12.2023.

[26] Kim, K., Ward, L., He, J., Krishna, A., Agrawal, A., Wolverton, C. Machine-learning-accelerated high-throughput materials screening: Discovery of novel quaternary Heusler compounds. *Phys. Rev. Mater.* **2018** *2(12)*, 123801.

[27] Park, C. W., Wolverton, C. Developing an improved crystal graph convolutional neural network framework for accelerated materials discovery. *Phys. Rev. Mater.* **2020** *4(6)*, 063801.

[28] Aykol, M., Dwaraknath, S. S., Sun, W., Persson, K. A. Thermodynamic limit for synthesis of metastable inorganic materials. *Sci. Adv.* **2018** *4(4)*, eaaq0148.

[29] Shen, J., Griesemer, S. D., Gopakumar, A., Baldassarri, B., Saal, J. E., Aykol, M., Hegde, V. I., Wolverton, C. Reflections on one million compounds in the open quantum materials database (OQMD) *JPhys Materials* **2022** *5(3)*, 031001.

[30] Rzewuski, J. Introduction to Quantum Theory. Pages 117-121, 149-151, 159-167, *Wrocław University of Science and Technology Publishing House Wroclaw* **1992**, ISBN 83-7085-002-2.

[31] Mattsson, A. E., Schultz, P. A., Desjarlais, M. P., Mattsson, T. R., Leung, K. Designing meaningful density functional theory calculations in materials science—a primer. *Model. Simul. Mat. Sci. Eng.* **2004** *13(1)*, R1.

[32] Kiejna, A. Fizyka materiałów i powierzchni z pierwszych zasad. *Postepy Fizyki* **2008** *59(3)*, 110–117.

[33] Hohenberg, P., Kohn, W. Inhomogeneous electron gas. *Phys. Rev.* **1964** *136(3B)*, B864.

[34] Piela, L. Idee chemii kwantowej. *PWN* **2003** Warszawa.

[35] Kohn, W., Sham, J. Self-consistent equations including exchange and correlation effects. *Phys. Rev.* **1965** *140(4A)*, A1133.

[36] Blaha, P., Schwarz, K., Sorantin, P., Trickey, S. B. Full-potential, linearized augmented plane wave programs for crystalline systems. *Comput. Phys. Commun.* **1990** *59(2)*, 399–415.

[37] Blügel, S., Bihlmayer, G. Full-potential linearized augmented planewave method. *Comput. nanosci.* **2006** *31*, 85–129.

[38] Michalicek, G., Krasovskii, E. E., Wessel, S., Blügel, S. Extending the precision and efficiency of the all-electron full-potential linearized augmented plane-wave density-functional theory method. `https://api.semanticscholar.org/CorpusID:126169481` **2015**.

[39] Schwarz, K., Blaha, P. Solid state calculations using WIEN2k. *Comput. Mater. Sci.* **2003** *28(2)*, 259–273.

[40] Ziman, J. M. Wstep do teorii ciała stałego. Pages: 24-27, *PWN Warszawa* **1977**.

[41] Blöchl, P. E. Projector augmented-wave method. *Phys. rev. B* **1994** *50(24)*, 17953.

[42] Welch E. DFT modeling of halide perovskites for optoelectronic applications. *PhD Dissertation* **2019**.

[43] Hood, R. Q., Chou, M. Y., Williamson, A. J., Rajagopal, G., Needs, R. J., Foulkes, W. M. C. Quantum monte carlo investigation of exchange and correlation in silicon. *Phys. Rev. Lett. 78(17)* **1997**, 3350.

[44] Sahni, V., Bohnen, K. P., Harbola, M. K. Analysis of the local-density approximation of density-functional theory. *Phys. Rev. A* **1895** *37(6)*, 1895.

[45] Bagayoko D. Understanding density functional theory (DFT) and completing it in practice. *API Adv.* **2014** *4*, 127104.

[46] Perdew, J. P., Burke, K., Ernzerhof, M. Generalized gradient approximation made simple. *Phys. Rev. Lett.* **1996** *77(18)*, 3865.

[47] Tran, F., Blaha, P. Accurate band gaps of semiconductors and insulators with a semilocal exchange-correlation potential. *Phys. Rev. Lett.* **2009** *102(22)*, 226401.

[48] Becke, A. D., Roussel, M. R. Exchange holes in inhomogeneous systems: A coordinate-space model. *Phy. Rev. A* **1989** *39(8)*, 3761.

[49] Martínez, J. C., Baquero, R. The modified Becke-Johnson potential analyzed. *Superf. y Vacio* **2013** *26(2)*, 54-5-57.

[50] Ashcroft, N. W., Mermin, N. D. Fizyka ciała stałego. *PWN* **1986** *Warszawa*, ISBN 83-01-05360-7.

[51] Zhang, L., Shi, X.-L., Yang, Y.-L., Chen, Z.-G. Flexible thermoelectric materials and devices: From materials to applications. *Mater. Today* **2021** *46*, 62–108.

[52] Faghaninia, A. Theory of carrier transport from first principles: Applications in photovoltaic and thermoelectric materials. **2016** *Washington University in St. Louis.*

[53] Singh, J. Singh, J. Modern physics for engineers. **2008** *John Wiley and Sons.*

[54] Bardeen, J., Shockley, W. J. P. R. Deformation potentials and mobilities in non-polar crystals. *Phys. Rev.* **1950** *80(1)*, 72.

[55] Gzyl, A. S., Oliynyk, A. O., Adutwum, L. A., Mar, A. Solving the Coloring Problem in Half-Heusler Structures: Machine-Learning Predictions and Experimental Validation. *Inorg. Chem.* **2019** *58(14)*, 9280–9289.

[56] Zhang, Y., Xu, X. Machine learning modeling of lattice constants for half-Heusler alloys. *AIP Adv.* **2020** *10*, 045121.

[57] Legrain, F., Carrete, J., van Roekeghem, A., Madsen, G. K., Mingo, N. Materials screening for the discovery of new half-Heuslers: Machine learning versus ab initio methods. *J. Phys. Chem. B.* **2018** *122(2)*, 625–632.

[58] Dylla, M. T., Dunn, A., Anand, S., Jain, A., Snyder, G. J. Machine learning chemical guidelines for engineering electronic structures in half-heusler thermoelectric materials. *Research* **2020**.

[59] Choudhary, M. K., Raj V, A., Ravindran, P. Composition and Structure Based GGA Bandgap Prediction Using Machine Learning Approach. *arXiv preprint arXiv:2309.07424* **2023**.

[60] Kurniawan, I., Miura, Y., Hono, K. Machine learning study of highly spin-polarized Heusler alloys at finite temperature. *Phys. Rev. Mater.*, **2022** *6(9)*, L091402.

[61] Carrete, J., Li, W., Mingo, N., Wang, S., Curtarolo, S. Finding unprecedentedly low-thermal-conductivity half-Heusler semiconductors via high-throughput materials modeling. *Phys. Rev. X* **2014** *4(1)*, 011019.

[62] Miyazaki, H., Tamura, T., Mikami, M., Watanabe, K., Ide, N., Ozkendir, O. M., Nishino, Y. Machine learning based prediction of lattice thermal conductivity for half-Heusler compounds using atomic information. *Sci. Rep.* **2021** *11(1)*, 13410.

[63] Tranås, R., Løvvik, O. M., Tomic, O., Berland, K. Lattice thermal conductivity of half-Heuslers with density functional theory and machine learning: Enhancing predictivity by active sampling with principal component analysis. *Comput. Mater. Sci.* **2022** *202*, 110938.

[64] Sklearn, `https://scikit-learn.org/stable/modules/cross_validation.html#cross-validation-evaluating-estimator-performance`, last accessed 15.12.2023.

[65] Huo, H., Rong, Z., Kononova, O., Sun, W., Botari, T., He, T., Tshitoyan, V., Ceder, G. Semi-supervised machine-learning classification of materials synthesis procedures. *Npj Comput. Mater.* **2019** *5(1)*, 62.

[66] Sklearn `https://scikit-learn.org/stable/modules/cross_validation.html#cross-validation-evaluating-estimator-performance`, last accessed 15.12.2023.

[67] Pedregosa, F., Varoquaux, G., Gramfort, A. and Michel, V., Thirion, B., Grisel, O., Blondel, M., Prettenhofer, P., Weiss, R., Dubourg, V., Vanderplas, J., Passos, A., Cournapeau, D., Brucher, M., Perrot, M., Duchesnay, E. Scikit-learn: Machine Learning in Python. *J. Mach. Learn. Res.* **2011** *12*, 2825–2830.

[68] `https://machine-learning-note.readthedocs.io/en/latest/algorithm/svm.html`, last accessed 15.12.2023.

[69] Awad, M.; Khanna, R.; Awad, M.; Khanna, R. Support vector regression. In *Efficient Learning Machines: Theories, Concepts, and Applications for Engineers and System Designers*; *Springer* **2015**, 67–80.

[70] Smola, A. J., Schölkopf, B. A Tutorial on Support Vector Regression. *Stat. Comput.* **2004** *14(3)*, 199–222.

[71] Vapnik, V. The nature of statistical learning theory. *Springer science and business media* **1999**.

[72] Lee, J., Seko, A., Shitara, K., Nakayama, K., Tanaka, I. Prediction model of band gap for inorganic compounds by combination of density functional theory calculations and machine learning techniques. *Phys. Review B* **2016** *93(11)*, 115104.

[73] Rohmah, M.F.; Putra, I.K.G.D.; Hartati, R.S.; Ardiantoro, L. Comparison four kernels of svr to predict consumer price index. *J. Phys. Conf. Ser.* **2021**, *1737*, 012018.

[74] Schölkopf, B. The kernel trick for distances. *Adv. Neural Inf. Process.* **2000** *13*.

[75] Fornberg, B., Larsson, E., Flyer, N. Stable computations with Gaussian radial basis functions. *SIAM J. Sci. Comput.* **2011** *33(2)*, 869–892.

[76] Mao, W., Mu, X., Zheng, Y., Yan, G. Leave-one-out cross-validation-based model selection for multi-input multi-output support vector machine. *Neural. Comput. Appl.* **2014** *24*, 441–451.

[77] Zhang, J., Wang, S., A fast leave-one-out cross-validation for SVM-like family. *Neural. Comput. Appl.* **2016** *27*, 1717–1730.

[78] Kresse, G., Hafner, J. Ab initio molecular dynamics for open-shell transition metals. *Phys. Rev. B* **1993** *48(17)*, 13115.

[79] Kresse, G., Hafner, J. Ab initio molecular-dynamics simulation of the liquid-metal–amorphous-semiconductor transition in germanium. *Phys. Rev. B* **1994** *49(20)*, 14251.

[80] Kresse, G., Furthmüller, J. Efficiency of ab-initio total energy calculations for metals and semiconductors using a plane-wave basis set. *Comput. Mater. Sci.* **1996** *6(1)*, 15–50.

[81] Kresse, G., Furthmüller, J. Efficient iterative schemes for ab initio total-energy calculations using a plane-wave basis set. *Phys. Rev. B* **1996** *54(16)*, 11169.

[82] Koller, D., Tran, F., Blaha, P. Improving the modified Becke-Johnson exchange potential. *Phys. Rev. B* **2012** *85(15)*, 155109.

[83] Aliev, F. G., Brandt, N. B., Moshchalkov, V. V., Kozyrkov, V. V., Skolozdra, R. V., Belogorokhov, A. I. Gap at the Fermi level in the intermetallic vacancy system RBiSn (R= Ti, Zr, Hf). *Z. Phys. B* **1989** *75*, 167–171.

[84] Kleinke, H., Franzen, H. F. Crystal Structures, Bonding and Electronic Structures of MM' As, a Series of New Ternary Arsenides (M= Zr, Hf; M'= Fe, Co, Ni). *Zeitschrift für anorganische und allgemeine Chemie* **1998** *624(1)*, 51–56.

[85] Nanda, B. R. K., Dasgupta, I. Electronic structure and magnetism in half-Heusler compounds. *J. Condens. Matter Phys.* **2003** *15(43)*, 7307.

[86] Oestreich, J., Probst, U., Richardt, F., Bucher, E. Thermoelectrical properties of the compounds ScMVIIISb and YMVIIISb (MVIII= Ni, Pd, Pt). *J. Condens. Matter Phys.* **2003** *15(4)*, 635.

[87] Demchyna, R., Prots, Y., Schwarz, U., Grin, Y. The Crystal Structures of the New Ternary Compounds TiPdGe, TiPdGa and ZrPdGa. *Zeitschrift für anorganische und allgemeine Chemie* **2004** *630(11)*, 1717–1717.

[88] Sekimoto, T., Kurosaki, K., Muta, H., Yamanaka, S. Thermoelectric properties of (Ti, Zr, Hf) CoSb type half-heusler compounds. *Mater. Trans.* **2005** *46(7)*, 1481–1484.

[89] Wang, L. L., Miao, L., Wang, Z. Y., Wei, W., Xiong, R., Liu, H. J., Shu, J., Tang, X. F. Thermoelectric performance of half-Heusler compounds TiNiSn and TiCoSb. *J. Appl. Phys.* **2009** *105(1)*.

[90] Lee, M. S., Poudeu, F. P., Mahanti, S. D. (2011). Publisher's Note: Electronic structure and thermoelectric properties of Sb-based semiconducting half-Heusler compounds. *Phys. Rev. B* **2011** *83(15)*s, 159907.

[91] Schmitt, J., Gibbs, Z. M., Snyder, G. J., Felser, C. Resolving the true band gap of ZrNiSn half-Heusler thermoelectric materials. *Mater. Horiz.* **2015** *2(1)*, 68–75.

[92] Abid, O. M., Menouer, S., Yakoubi, A., Khachai, H., Omran, S. B., Murtaza, G., Prakash, D., Khenata, R., Verma, K. D. Structural, electronic, elastic, thermoelectric and thermodynamic properties of the NbMSb half heusler (M= Fe, Ru, Os) compounds with first principle calculations. *Superlattices Microstruct.* **2016** *93*, 171–185.

[93] Bhattacharya, S., Madsen, G. K. A novel p-type half-Heusler from high-throughput transport and defect calculations. *J. Mater. Chem. C* **2016** *4(47)*, 11261–11268.

[94] Narimani, M., Nourbakhsh, Z. Topological band order, structural, electronic and optical properties of XPdBi (X = Lu, Sc) compounds. *Mod. Phys. Lett. B.* **2016** *30(14)*, 1650159.

[95] Wang, G., Wang, D. Electronic structure and thermoelectric properties of Pb-based half-Heusler compounds: ABPb (A= Hf, Zr; B= Ni, Pd). *J. Alloys Compd.* **2016** *682*, 375–380.

[96] Kaur, K., Rai, D. P., Thapa, R. K., Srivastava, S. Structural, electronic, mechanical, and thermoelectric properties of a novel half Heusler compound HfPtPb. *J. Appl. Phys.* **2017**, *122(4)*, 045110.

[97] Weber, S. F., Chen, R., Yan, Q., Neaton, J. B. Prediction of TiRhAs as a Dirac nodal line semimetal via first-principles calculations. *Phys. Rev. B* **2017** 96(23), 235145.

[98] Singh, B., Zhou, X., Lin, H., Bansil, A. Saddle-like topological surface states on the T T' X family of compounds (T, T'= Transition metal, X= Si, Ge). *Phys. Rev. B* **2018** *97(7)*, 075125.

[99] Zhao, D., Wang, L., Bo, L., Wu, D. Synthesis and thermoelectric properties of Ni-doped ZrCoSb half-Heusler compounds. *Metals* **2018** *8(1)*, 61.

[100] Zhu, H., He, R., Mao, J., Zhu, Q., Li, C., Sun, J., Ren, W., Wang, Y, Liu, Z., Tang, Z., Sotnikov, A., Wang, Z., Broido, D., Singh, D. J., Chen, Gang, Nielsch, K., Ren, Z. Discovery of ZrCoBi based half Heuslers with high thermoelectric conversion efficiency. *Nat. Commun.* **2018** *9(1)*, 2497.

[101] Adetunji, B.I.; Adebambo, P.O.; Bamgbose, M.K.; Musari, A.A.; Adebayo, G.A. Predicting the elastic, phonon and thermodynamic properties of cubic HfNiX (X = Ge and Sn) Half Heusler alloys: A DFT study. *Eur. Phys. J. B* **2019**, *92*, 1–7.

[102] Ma, H., Yang, C. L., Wang, M. S., Ma, X. G., Yi, Y. G. Effect of M elements (M= Ti, Zr, and Hf) on thermoelectric performance of the half-Heusler compounds MCoBi. *J. Phys. D* **2019** *52(25)*, 255501.

[103] Surucu, G., Candan, A., Erkisi, A., Gencer, A., Güllü, H. H. First principles study on the structural, electronic, mechanical and lattice dynamical properties of XRhSb (X= Ti and Zr) paramagnet half-Heusler antimonides. *MRX* **2019** *6(10)*, 106315.

[104] Synoradzki, K., Ciesielski, K., Veremchuk, I., Borrmann, H., Skokowski, P., Szymański, D., Grin, Y., Kaczorowski, D. Thermal and electronic transport properties of the half-Heusler phase ScNiSb. *Mater.* **2019** *12(10)*, 1723.

[105] Zhu, H., Mao, J., Li, Y., Sun, J., Wang, Y., Zhu, Q., Li, G., Song, Q., Zhou, J., Fu, Y., Ren, Z. Discovery of TaFeSb-based half-Heuslers with high thermoelectric performance. *Nat. Commun* **2019** *10(1)*, 270.

[106] Bamgbose, M. K. (2020). Electronic structure and thermoelectric properties of HfRhZ (Z= As, Sb and Bi) half-Heusler compounds. *Appl. Phys. A* **2020** *126*, 1–8.

[107] Candan, A.; Kushwaha, A.K. A first-principles study of the structural, electronic, optical, and vibrational properties for paramagnetic half-Heusler compound TiIrBi by GGA and GGA+ mBJ functional. *Mater. Today Commun.* **2021** *27*, 102246.

[108] Hong, A. J., Li, L., He, R., Gong, J. J., Yan, Z. B., Wang, K. F., Liu, J-M, Ren, Z. F. Full-scale computation for all the thermoelectric property parameters of half-Heusler compounds. *Sci. Rep.* **2016** *6(1)*, 22778.

[109] Mahan, G. D. Figure of merit for thermoelectrics. *J. Appl. Phys.* **1989** *65(4)*, 1578–1583.

[110] Kangsabanik, J.; Alam, A. Bismuth based half-Heusler alloys with giant thermoelectric figures of merit. *J. Mater. Chem. A* **2017**, *5*, 6131–6139.

[111] Fu, C.; Zhu, T.; Liu, Y.; Xie, H.; Zhao, X. Band engineering of high performance p-type FeNbSb based half-Heusler thermoelectric materials for figure of merit zT $>$ 1. *Energy Environ. Sci.* **2015**, *8*, 216–220.

[112] Fang, T.; Zheng, S.; Chen, H.; Cheng, H.; Wang, L.; Zhang, P. Electronic structure and thermoelectric properties of p-type half-Heusler compound NbFeSb: A first-principles study. *RSC Adv.* **2016**, *6*, 10507–10512.

[113] Feng, W., Xiao, D., Zhang, Y., Yao, Y. Half-Heusler topological insulators: A first-principles study with the Tran-Blaha modified Becke-Johnson density functional. *Phys. Rev. B* **2010** *82(23)*, 235121.

[114] Song, Z. G., Felser, C., Sun, Y. Prediction of ideal triple degenerate points in HfIrAs and HfIrBi. *Phys. Rev. B* **2018** *98(16)*, 165131.

[115] Wang, W., Du, Y., Xu, G., Zhang, X., Liu, E., Liu, Z., Shi, Y., Chen, J., Wu, G., Zhang, X. X. Large linear magnetoresistance and Shubnikov-de Hass oscillations in single crystals of YPdBi Heusler topological insulators. *Sci. Rep.* **2013** *3(1)*, 2181.

[116] Nowak, B., Kaczorowski, D. Nonmetallic behaviour in half-Heusler phases YPdSb, YPtSb and LuPtSb. *Intermetallics* **2013** *40*, 28–35.

[117] Musari, A. A. Systematic study of stable Palladium and Nickel based half-Heusler compounds for thermoelectric generators. *Available at SSRN 4640619.*

[118] Slack, G.A. Nonmetallic crystals with high thermal conductivity. *J. Phys. Chem. Solids* **1973**, *34*, 321–335.

[119] Madsen, G. K. H., Carrete, J., Verstraete, M. J. BoltzTraP2, a program for interpolating band structures and calculating semi-classical transport coefficients. *Comput. Phys. Commun.* **2018** *231*, 140–145.

[120] Sun, H.L.; Yang, C.L.; Wang, M.S.; Ma, X.G. Remarkably high thermoelectric efficiencies of the half-Heusler compounds BXGa (X = Be, Mg, and Ca). *ACS Appl. Mater. Interfaces* **2020**, *12*, 5838–5846.

[121] Yang, K.; Wan, R.; Zhang, Z.; Lei, Y.; Tian, G. First-principle investigation on the thermoelectric and electronic properties of HfCoX (X = As, Sb, Bi) half-Heusler compounds. *J. Solid State Chem.* **2022**, *312*, 123386.

[122] Kittel, C. Wstep do fizyki ciala stalego. *PWN* **1960** *Warszawa*, pages 291–293.

[123] Wiendlocha, B. Thermopower of thermoelectric materials with resonant levels: PbTe:T1 versus PbTe:Na and Cu1-xNix. *Phys. Rev. B* **2018** *97*, 205203.

[124] Qiu, Q.; Liu, Y.; Xia, K.; Fang, T.; Yu, J.; Zhao, X.; Zhu, T. Grain boundary scattering of charge transport in n-type (Hf, Zr) CoSb half-Heusler thermoelectric materials. *Adv. Energy Mater.* **2019** *9(11)*, 1803447.

[125] Snyder, G. J., Toberer, E. S. Complex thermoelectric materials. *Nat. Mater.* **2008** *7(2)*, 105–114.

[126] Pei, Y., LaLonde, A. D., Wang, H., Snyder, G. J. (2012). Low effective mass leading to high thermoelectric performance. *Energy Environ. Sci.* **2012** *5(7)*, 7963–7969.

[127] Shen, J., Fan, L., Hu, C., Zhu, T., Xin, J., Fu, T., Zhao, D., Zhao, X. Enhanced thermoelectric performance in the n-type NbFeSb half-Heusler compound with heavy element Ir doping. *Mater. Today Phys.* **2019** *8*, 62–70.

[128] Naydenov, G. A.; Hasnip, P. J.; Lazarov, V. K.; Probert, M. I. J. Huge power factor in p-type half-Heusler alloys NbFeSb and TaFeSb. *JPhys* **2019** *2(3)*, 035002.

[129] Guo, S. D. Importance of spin–orbit coupling in power factor calculations for half-Heusler ANiB (A= Ti, Hf, Sc, Y; BSn, Sb, Bi). J. Alloys Compd. **2016** *663*, 128–133.

[130] Bannov, N., Aristov, V., Mitin, V., Stroscio, M. A. Electron relaxation times due to the deformation-potential interaction of electrons with confined acoustic phonons in a free-standing quantum well. *Phys. Rev. B* **1995** *51(15)*, 9930.

[131] Ahmad, S., Mahanti, S. D. Energy and temperature dependence of relaxation time and Wiedemann-Franz law on PbTe. *Phys. Rev. B* **2010** *81(16)*, 165203.

[132] Liu, J., Jiang, Q. Y., Zhang, S. D., Zhang, H. Carrier mobility and relaxation time in BiCuSeO. *Phys. Lett. A* **2019** *383(34)*, 125990.

[133] Xia, K., Liu, Y., An, S., Snyder, G.J., Xin, J., Yu, J., Zhao, X., Zhu, T. Enhanced thermoelectric performance in 18-electron Nb0.8CoSb half-heusler compound with intrinsic Nb vacancies. *Adv. Funct. Mater.* **2018** *28*, 1705845.

[134] Krez, J., Schmitt, J., Snyder, G. J., Felser, C., Hermes, W., Schwind, M. Optimization of the carrier concentration in phase-separated half-Heusler compounds. *J. Mater. Chem. A* **2014** *2(33)*, 13513–13518.

[135] Downie, R. A., MacLaren, D. A., Bos, J. W. Thermoelectric performance of multi-phase XNiSn (X= Ti, Zr, Hf) half-Heusler alloys. *J. Mater. Chem. A* **2014** *2(17)*, 6107–6114.

[136] Gürth, M., Rogl, G., Romaka, V.V., Grytsiv, A., Bauer, E., Rogl, P. Thermoelectric high ZT half-Heusler alloys Ti1-x-yZrxHfyNiSn ($0 < x < 1$; $0 < x < 1$). *Acta Mater.* **2016** *104*, 210—222

[137] Li, S., Zhu, H., Mao, J., Feng, Z., Li, X., Chen, C., Cao, F., Liu, X., Singh, D.J., Ren, Z., et al. n-Type TaCoSn-Based Half-Heuslers as Promising Thermoelectric Materials *ACS Appl. Mater. Interfaces* **2019** *11(44)*, 41321-–41329.

[138] Ramarao, S.D., Pawbake, A., Singh, A.K., Núñez-Regueiro, M., Méasson, M.A., Peter, S.C. Electrical transport properties of half-heusler ScPdBi single crystals under extreme conditions. *J. Alloys Compd.* **2020** *848*, 156632.

[139] Çiftci, Y.Ö., Çoban, C. Ab initio calculations on the structural, mechanical, electronic, dynamic, and optical properties of semiconductor half-heusler compound ZrPdSn. *Z. Naturforsch. A* **2016** *71*, 135-–143.

[140] Chauhan, N.S., Miyazaki, Y. Low lattice thermal conductivity and microstructural evolution in VFeSb half-Heusler alloys. *Materialia* **2022** *22*, 101430.

[141] Gupta, Y., Sinha, M.M., Verma, S.S. First-principles investigation on the electronic, mechanical and lattice dynamical properties of novel AlNiX (X = As and Sb) half-Heusler alloys. *Mater. Today Commun.* **2021** *26*, 101885.

[142] Razzaq, S., Ismail, K., Murtaza, G., Raza, H.H. Theoretical Study of Half-Heusler CsXAs (X = Ca, Sr, and Ba) from First Principle Calculations. *J. Supercond. Nov. Magn.* **2022** *35*, 3291-–3299.

[143] Mokhtari, H., Boumia, L., Mokhtari, M., Dahmane, F., Mansour, D., Khenata, R. Mechanical Stability, Electronic, and Magnetic Properties of XZrAs (X = Cr, Mn, V) Half-Heusler Compounds. *J. Supercond. Nov. Magn.* **2023** *36*, 1217—1244.

[144] Xiong, L., Yi, L., Gao, G. Y. Search for half-metallic magnets with large half-metallic gaps in the quaternary Heusler alloys CoFeTiZ and CoFeVZ (Z= Al, Ga, Si, Ge, As, Sb). *J. Magn. Magn. Mater.* **2014** *360*, 98–103.

[145] Van Rossum, G., Drake, F. L. Python 3 Reference Manual. *CreateSpace Scotts Valley, CA* **2009**, ISBN 1441412697.

[146] WebElements, `https://www.webelements.com`, last accessed 13.11.2023.

[147] `https://scikit-learn.org/stable/modules/generated/sklearn.preprocessing.StandardScaler.html`, last accessed 18.12.2023.

[148] Popoola, A.I.; Odusote, Y.A. The properties of NbRhGe as high temperature thermoelectric material. *IOSR J. Appl. Phys.* **2019**, *11*, 51–56.

[149] Jaishi, D.R.; Sharma, N.; Karki, B.; Belbase, B.P.; Adhikari, R.P.; Ghimire, M.P. Electronic structure and thermoelectric properties of half-Heusler alloys NiTZ. *AIP Adv.* **2021**, *11*, 025304.

[150] Li, S.; Zhao, H.; Li, D.; Jin, S.; Gu, L. Synthesis and thermoelectric properties of half-Heusler alloy YNiBi. *J. Appl. Phys.* **2015**, *117*, 205101.

[151] Chen, J.; Li, H.; Ding, B.; Hou, Z.; Liu, E.; Xi, X.; Zhang, H.; Wu, G.; Wang, W. Structural and magnetotransport properties of topological trivial LuNiBi single crystals. *J. Alloys Compd.* **2019**, *784*, 822–826.

[152] Zerrouki, T.; Rached, H.; Rached, D.; Caid, M.; Cheref, O.; Rabah, M. First-principles calculations to investigate structural stabilities, mechanical and optoelectronic properties of NbCoSn and NbFeSb half-Heusler compounds. *Int. J. Quantum Chem.* **2021**, *121*, e26582.

[153] Qu, J.; Xie, Y. R.; Ciesielski, K. M.; Porter, C. E.; Toberer, E. S.; Ertekin, E. Leveraging language representation for materials exploration and discovery. *Npj Comput. Mater.* **2024**, *10(1)*, 58.

[154] Tranås, R.; Løvvik, O.M.; Berland, K. Lattice Thermal Conductivity from First Principles and Active Learning with Gaussian Process Regression. *arXiv* **2023**, arXiv:2309.06786.

[155] Narducci, D. Do we really need high thermoelectric figures of merit? A critical appraisal to the power conversion efficiency of thermoelectric materials. *Appl. Phys. Lett.* **2011**, *99*, 102104.

[156] Touia, A.; Benyahia, K.; Tekin, A. First-principles calculations of structural, electronic, optical, and thermoelectric properties of LuNiBi and LuNiSb half-heusler. *J. Supercond. Nov. Magn.* **2021**, *34*, 2689—2698.

[157] Singh, S.; Zeeshan, M.; Brink, J.V.D.; Kandpal, H.C. Ab initio study of Bi-based half Heusler alloys as potential thermoelectric prospects. *arXiv* **2019**, arXiv:1904.02488.

[158] Yazdani-Kachoei, M.; Li, S.; Sun, W.; Allaei, S.M.V.; Di Marco, I. Role of volume change on the physics of thermoelectric half-Heusler compounds. *Phys. Rev. Mater.* **2023**, *7*, 104602.

[159] Fang, T.; Zheng, S.; Zhou, T.; Yan, L.; Zhang, P. Computational prediction of high thermoelectric performance in p-type half-Heusler compounds with low band effective mass.*PCCP* **2017**, *19*, 4411—4417.

[160] Mafe, A.S.; Shogo, O.E.; Bello, B.W.; Musari, A.A. Systematic study of stable palladium and nickel based half-Heusler compounds for thermoelectric generators. *Solid State Sci.* **2024**, *149*, 107451.

[161] Joshi, G., He, R., Engber, M., Samsonidze, G., Pantha, T., Dahal, E., Yang, J., Lan, Y., Kozinsky, B., Ren, Z. NbFeSb-based p-type half-Heuslers for power generation applications. *J. Am. Chem. Soc.* **2019** *12*, 4070—4076

[162] Kalita, D.; Limbu, N.; Ram, M.; Saxena, A. DFT study of structural, mechanical, thermodynamic, electronic, and thermoelectric properties of new PdTi Z (Z= Ge and Pb) half Heusler compounds. *Int. J. Quantum Chem.* **2022**, *122*, e26951.

[163] Cherifi, F.; Mostefa, Z.; Boukra, A.; Meghoufel, Z.F.; Bouattou, M.; Kadi Allah, F.; Terki, F. Thermoelectric Transport Parameters of p-Type RuVAs and RuNbAs Heusler Alloys. *Phys. Status Solidi B Basic Res.* **2020**, *257*, 2000271

[164] Bendahma, F.; Mana, M.; Terkhi, S.; Cherid, S.; Bestani, B.; Bentata, S. Investigation of high figure of merit in semiconductor XHfGe (X= Ni and Pd) half-Heusler alloys: Ab-initio study. *Comput. Condens. Matter* **2019**, *21*, e00407.

[165] Solola, G.T.; Bamgbose, M.K.; Adebambo, P.O.; Ayedun, F.; Adebayo, G.A. First-principles investigations of structural, electronic, vibrational, and thermoelectric properties of half-Heusler VYGe (Y= Rh, Co, Ir) compounds. *Comput. Condens. Matter* **2023**, *36*, e00827.

[166] Hong, D.; Zeng, W.; Xin, Z.; Liu, F.S.; Tang, B.; Liu, Q.J. First-principles calculations of structural, mechanical and electronic properties of TiNi-X (X= C, Si, Ge, Sn, Pb) alloys. *Int. J. Mod. Phys. B* **2019**, *33*, 1950167.

[167] Akinlami, J.O.; Odeyemi, O.O.; Omeike, M.O.; Adebayo, G.A. First principle calculations of the structural, elastic, electronic and transport properties of XRuAs (X = Ta and V). *Mater. Sci. Semicond.* **2022**, *148*, 106837.

[168] Rani, B.; Khandy, S.A.; Singh, J.; Verma, A.S.; Ali, A.M.; Dhiman, S.; Kaur, K. Electronic structure, elastic and transport properties of new Palladium-based Half-Heusler Materials for Thermoelectric Applications. *Mater. Today Commun.* **2023**, *2023*, 106461.

[169] Lazab, M.; Djebour, B.; Bouafia, H.; Bousmaha, M.; Sahli, B.; Boudia, K. Mechanical and dynamical stability, electronic and bonding properties of a new narrow-gap semiconductor YPdAs Half-Heusler: DFT and QTAIM study. *Mater. Sci. Semicond.* **2024**, *173*, 108160.

[170] Benallou, Y.; Amara, K.; Doumi, B.; Arbouche, O.; Zemouli, M.; Bekki, B.; Mokaddem, A. Structural stability, electronic structure, and novel transport properties with high thermoelectric performances of ZrIrX (X = As, Bi, and Sb). *J. Comput. Electron.* **2017**,
em 16, 1-–11.

[171] Nagata, Y.; Sodeyama, K.; Yashiro, S.; Sasaki, H.; Samata, H.; Uchida; T.; Lan, M. D. New intermetallic compounds found in Hf–Ni–Ge and Hf–Pt–Ge systems. *J. Alloys Compd.* **1998** *281(2)*, 112–116.

[172] Mallick, M. M.; Vitta, S. Thermoelectric properties of ultra-low thermal conductivity half-Heusler alloy. *AIP Conf. Proc.* **2016** *1731(1)*.

[173] Bende, D., Wagner, F. R., Sichevych, O., Grin, Y. Chemical bonding analysis as a guide for the preparation of new compounds: The case of VIrGe and HfPtGe. *Angewandte Chemie* **2016** *129(5)*, 1333–1338.

[174] Kuentzler, R.; Waterstrat, R. M. Electronic properties, superconductivity and stability of the ordered alloys of the Ti-Rh, Zr-Rh and Hf-Rh isoelectronic systems. *Solid State Commun.* **1988** *68(1)*, 85–91.

[175] Rajendran, A.; John, R. First principles study on electronic properties and mechanical stability of HfRhZ (Z= As and Sb) half Heusler alloys. *J. Cryst. Growth* **2022** *581*, 126468.

[176] Kangsabanik, J.; Alam, A. Bismuth based half-Heusler alloys with giant thermoelectric figures of merit. *J. Mater. Chem. A* **2017** *5(13)*, 6131–6139.

[177] Andrea, L.; Hug, G.; Chaput, L. Ab initio phonon properties of half-Heusler NiTiSn, NiZrSn and NiHfSn. *J. Condens. Matter Phys.* **2015** *27(42)*, 425401.

[178] Kimura, Y.; Zama, A. Thermoelectric properties of p-type half-Heusler compound HfPtSn and improvement for high-performance by Ir and Co additions. *Appl. Phys. Lett.* **2006** *89(17)*.

[179] Morkowski, J. A.; Szajek, A.; Chełkowska, G.; Bajorek, A.; Troć, R. Electronic structure and X-ray photoemission spectra of MPtSn (M= Ti, Zr, Hf). *Acta Phys. Pol. A* **2009** *115*, 935.

[180] Xiong, X.; Jiang, Q.; Wan, R.; Zhang, Z.; Lei, Y.; Tian, G. Computational prediction of high thermoelectric performance in MPtSn (M= Ti, Zr, and Hf) half-Heusler compounds by first-principle study. *Solid State Sci.* **2022** *127*, 106859.

[181] Grykałowska, A.; Nowak, B. High-resolution solid-state 119Sn and 195Pt NMR studies of MPtSn semiconductors (M= Ti, Zr, Hf, Th). *ssNMR* **2005** *27(4)*, 223–227.

[182] Xiong, X.; Wan, R.; Zhang, Z.; Lei, Y.; Tian, G. First-principle investigation on the thermoelectric properties of XCoGe (X= V, Nb, and Ta) half-Heusler compounds. *Mater. Sci. Semicond. Process.* **2022** *140*, 106387.

[183] Khan, W.; Gul, B.; Din, H. U.; Azam, S.; Asghar, H.; Aftab, S.; Ali, H. E. (2023). First principle study of strain tunable electronic and optical properties of half-Heusler alloys XCoGe (X= V, Nb, Ta). *J. Solid State Chem.*]bf 2023 *319*, 123827.

[184] Wang, Y.; Li, J.; Wang, J.; He, F.; Xu, X.; Liu, Y.; Yin, F. Prediction of NbXGe (X= Rh, Ir) half-Heusler semiconducting compounds with promising thermoelectric property using 18-electron rule. *Appl. Phys. Lett. A* **2022** *128*, 1–11.

[185] Hohl, H.; Ramirez, A. P.; Goldmann, C.; Ernst, G.; Wölfing, B.; Bucher, E. New compounds with MgAgAs-type structure: NbIrSn and NbIrSb. *J. Condens. Matter Phys.* **1998** *10(35)*, 7843.

[186] Springborg, M.; Sang, B.; Persson, M. L. Electronic and structural properties of two semi-Heusler alloys: NbIrSn and NbIrSb. *J. Condens. Matter Phys. 11(32)*, 6169.

[187] Xing, G.; Sun, J.; Li, Y.; Fan, X.; Zheng, W.; Singh, D. J. Electronic fitness function for screening semiconductors as thermoelectric materials. *Phys. Rev. Mater.* **2017** *1(6)*, 065405.

[188] Osafile, O. E.; Nenuwe, O. N. Lattice dynamics and thermodynamic responses of XNbSn half-heusler semiconductors: A first-principles approach. *J. Nig. Soc. Phys. Sci.* **2021** *3*, 121–130.

[189] Kaur, K.; Kumar, R. On the possibility of thermoelectricity in half Heusler XRuSb (X= V, Nb, Ta) materials: A first principles prospective. *J. Phys. Chem. Solids* **2017** *110*, 108–115.

[190] Serrano-Sánchez, F.; Luo, T.; Yu, J.; Xie, W.; Le, C.; Auffermann, G. *et al.* Thermoelectric properties of n-type half-Heusler NbCoSn with heavy-element Pt substitution. *J. Mater. Chem.* **2020** *8(29)*, 14822–14828.

[191] Kimura, Y.; Tamura, Y.; Kita, T. Thermoelectric properties of directionally solidified half-Heusler compound NbCoSn alloys. *Appl. Phys. Lett.* **2008** *92(1)*, 012105.

[192] Wafula, J. W.; Makokha, J. W.; Manyali, G. S. First-principles calculations to investigate structural, elastic, electronic and thermodynamic properties of NbCoSn and VRhSn Half-Heusler compounds. *Results Phys.* **2022** *43*, 106132.

[193] Joshi, G.; He, R.; Engber, M.; Samsonidze, G.; Pantha, T.; Dahal, E., *et al.* NbFeSb-based p-type half-Heuslers for power generation applications. *Energy Environ. Sci.* **2014** *7(12)*, 4070–4076.

[194] Yu, J.; Fu, C.; Liu, Y.; Xia, K.; Aydemir, U.; Chasapis, T. C.*et al.* Unique role of refractory Ta alloying in enhancing the figure of merit of NbFeSb thermoelectric materials. *Adv. Mater.* **2018** *8(1)*, 1701313.

[195] Zhang, J.; Hou, Z.; Zhang, C.; Chen, J.; Li, P.; Wen, Y. *et al.* Weak antilocalization effect and high-pressure transport properties of ScPdBi single crystal. *Appl. Phys. Lett.* **2019** *115(17)*, 172407.

[196] Narimani, M.; Nourbakhsh, Z Topological phase, electronic, magnetic and optical properties of ScPdBi compound with Gd, Np and Cm impurities. *J. Magn. Magn. Mater.* **2017** *434*, 62–67.

[197] Radjai, M., Bouhemadou, A.; Maouche, D. Structural, elastic, electronic and optical properties of the half-Heusler ScPtSb and YPtSb compounds under pressure. *arXiv preprint arXiv:2112.09940* **2021**.

[198] Haque, E.; Hossain, M. A. First-principles study of elastic, electronic, thermodynamic, and thermoelectric transport properties of TaCoSn. *Results Phys.* **2018** *10*, 458–465.

[199] Zakutayev, A., Zhang, X., Nagaraja, A., Yu, L., Lany, S., Mason, T. O., *et al.* Theoretical prediction and experimental realization of new stable inorganic materials using the inverse design approach. *J. Am. Chem. Soc.* **2013** *135(27)*, 10048–10054.

[200] Kaur, K.; Kumar, R. High temperature thermoelectric performance of p-type TaRhSn half Heusler compound: A computational assessment. *Ceram. Int.* **2017** *43(17)*, 15160–15166.

[201] Khaldi, A.; Benallou, Y.; Zemouli, M.; Amara, K.; El Keurti, M. First Principle Study and Optimal Doping for High Thermoelectric Performance of TaXSn Materials (X= Co, Ir and Rh). *J. Nano- Electron. Phys.* **2021** *13(1)*, 01011.

[202] Almaghbash, Z. A. A. R.; Arbouche, O.; Dahani, A.; Cherifi, A.; Belabbas, M.; Zenati, A. *et al.* Thermoelectric and piezoelectric properties in half-Heusler compounds TaXSn (X= Co, Rh and Ir) based on ab initio calculations. *Int. J. Thermophys.* **2021** *42*, 1–19.

[203] Saini, H. S.; Srivastava, S.; Kashyap, M. K. Enhanced figure of merit of TaIrGe Half-Heusler alloy for thermoelectric applications under the effect of isotropic strain. *J. Solid State Chem.* **2021** *303*, 122524.

[204] Wei, J.; Wang, G. Properties of half-Heusler compounds TaIrGe by using first-principles calculations. *Appl. Phys. A* **2017** *123*, 1–6.

[205] Kaur, K.; Kumar, R. Giant thermoelectric performance of novel TaIrSn Half Heusler compound. *Phys. Lett. A* **2017** *381(44)*, 3760–3765.

[206] Liu, J.; Cao, G.; Zhou, Z.; Liu, H. Screening potential topological insulators in half-Heusler compounds via compressed-sensing. *J. Phys. Condens. Matter* **2021** *33(32)*, 325501.

[207] de Oliveira, L. S.; de Oliveira Melquiades, M.; da Costa Pinto, C.; Triches, D. M.; de Souza, S. M. Phase transformations in a NiTiGe system induced by high energy milling. *J. Solid State Chem.* **2020** *281*, 121056.

[208] Kaur, K. TiPdSn: A half Heusler compound with high thermoelectric performance. *EPL* **2017** *117(4)*, 47002.

[209] Zheng, W.; Lu, Y.; Li, Y.; Wang, J.; Hou, Z.; Shao, X. Structural and thermoelectric properties of Zr-doped TiPdSn half-Heusler compound by first-principles calculations. *Chem. Phys. Lett.* **2020** *741*, 137055.

[210] Dasmahapatra, A.; Daga, L. E.; Karttunen, A. J.; Maschio, L.; Casassa, S. Key role of defects in thermoelectric performance of TiMSn (M= Ni, Pd, and Pt) half-heusler alloys. *J. Phys. Chem. C* **2020** *124(28)*, 14997–15006.

[211] Ashani, T. M.; Sunmonu, R. S.; Akinlami, J. O.; Adebayo, G. A. Predicting the band structure, transport properties, electronic fitness function and effective mass of PdTiSn indirect band-gap half-Heusler semiconductor. *Mater. Sci. Semicond.* **2021** *123*, 105548.

[212] Benndorf, C.; Eckert, H.; Pöttgen, R. 29 Si, 47 Ti, 49 Ti and 195 Pt solid state MAS NMR spectroscopic investigations of ternary silicides TPtSi, germanides TPtGe (T= Ti, Zr, Hf) and stannide TiPtSn. *Dalton Trans.* **2016** *45(19)*, 8215–8223.

[213] Ackerbauer, S. V.; Senyshyn, A.; Borrmann, H.; Burkhardt, U.; Ormeci, A.; Rosner, H. *et al.* (2012). Structural transformation with "negative volume expansion": Chemical bonding and physical behavior of TiGePt. *Chem. Eur. J.* **2012** *18(20)*, 6272–6283.

[214] Grykałowska, A.; Nowak, B. Nuclear spin-lattice relaxation in narrow gap semiconductors TiPtSn and ZrPtSn. *Intermetallics* **2007** *15(11)*, 1479–1482.

[215] Ma, J.; Hegde, V. I.; Munira, K.; Xie, Y.; Keshavarz, S.; Mildebrath, D. T. *et al.* Computational investigation of half-Heusler compounds for spintronics applications. *Phys. Rev. B* **2017** *95(2)*, 024411.

[216] Birkel, C. S.; Zeier, W. G.; Douglas, J. E.; Lettiere, B. R.; Mills, C. E.; Seward, G. *et al.* Rapid microwave preparation of thermoelectric TiNiSn and TiCoSb half-Heusler compounds. *Chem. Mater.* **2012** *24(13)*, 2558–2565.

[217] Xia, Y.; Ponnambalam, V.; Bhattacharya, S.; Pope, A. L.; Poon, S. J.; Tritt, T. M. Electrical transport properties of TiCoSb half-Heusler phases that exhibit high resistivity. *J. Phys. Condens. Matter* **2001** *13(1)*, 77.

[218] Kawaharada, Y.; Kurosaki, K.;; Muta, H.; Uno, M.; Yamanaka, S. High temperature thermoelectric properties of CoTiSb half-Heusler compounds. *J. Alloys Compd.* **2004** *384(1-2)*, 308–311.

[219] Ouardi, S.; Fecher, G. H.; Felser, C.; Schwall, M.; Naghavi, S. S.; Gloskovskii, A.*et al.* Electronic structure and optical, mechanical, and transport properties of the pure, electron-doped, and hole-doped Heusler compound CoTiSb. *Phys. Rev. B* **2012** *86(4)*, 045116.

[220] Surucu, G.; Isik, M.; Candan, A.; Wang, X.; Gullu, H. H. Investigation of structural, electronic, magnetic and lattice dynamical properties for XCoBi (X: Ti, Zr, Hf) Half-Heusler compounds. *Physica B Condens.* **2020** *587*, 412146.

[221] Umukoro, J. O.; Omagbemi, O. G.; Osafile, O. E. Effect of Spin-Orbit Coupling (SOC) On the Electronic and Thermoelectric Properties of Ticobi Half Heusler Alloy. *J. Phys. Chem. Res.* **2022**, 4(4).

[222] Jaishi, D. R.; Bati, S.; Sharma, N.; Karki, B.; Belbase, B. P.; Ghimire, M. P. Rhodium-based half-Heusler alloys as thermoelectric materials. *Phys. Chem. Chem. Phys.* **2022** *24(33)*, 19844–19852.

[223] Azin-Sanjabod, M. R.; Nedaee-Shakarab, B.; Azizian-Kalandaragh, Y.; Akbari, H. Comparison of electronic and thermoelectric properties of RhTiAs and RhTiSb in bulk and their [111] films. *Int. Nano Lett.* **2021** *11*, 125–139.

[224] Ahmad, R.; Gul, A.; Mehmood, N. Artificial neural networks and vector regression models for prediction of lattice constants of half-Heusler compounds. *MRX* **2019** *6(4)*, 046517.

[225] Benzoudji, F.; Abid, O. M.; Seddik, T.; Yakoubi, A.; Khenata, R.; Meradji, H. *et al.* Insight into the structural, elastic, electronic, thermoelectric, thermodynamic and optical properties of MRhSb (M= Ti, Zr, Hf) half-Heuslers from ab initio calculations. *Chinese J. Phys.* **2019** *59*, 434–448.

[226] Yan, F.; Zhang, X.; Yu, Y. G.; Yu, L.; Nagaraja, A.; Mason, T. O.; Zunger, A. Design and discovery of a novel half-Heusler transparent hole conductor made of all-metallic heavy elements. *Nat. Commun.* **2015** *6(1)*, 7308.

[227] Keshri, S. P.; Pati, S. K. d-Orbital-driven low lattice thermal conductivity in TiRhBi: A root for potential thermoelectric and microelectronic performance. *ACS Appl. Energy Mater.* **2022** *5(11)*, 13590–13599.

[228] Kaur, K.; Kumar, R. Ti based half Heusler compounds: A new on the screen with robustic thermoelectric performance. *J. Alloys Compd.* **2017** *727*, 1171–1177.

[229] Bamgbose, M. K. First-principles study of electronic structure and thermoelectric properties of p-type XIrSb (X= Ti, Zr and Hf) half-Heusler compounds. *Mater. Sci. Semicond. Process* **2021** *129*, 105792.

[230] Guo, S.; Anand, S.; Brod, M. K.; Zhang, Y.; Snyder, G. J. Conduction band engineering of half-Heusler thermoelectrics using orbital chemistry. *J. Mater. Chem. A* **2022** *10(6)*, 3051–3057.

[231] Brod, M. K.; Guo, S.; Zhang, Y.; Snyder, G. J. Explaining the electronic band structure of half-Heusler thermoelectric semiconductors for engineering high valley degeneracy. *MRS Bulletin* **2022** *47(6)*, 573–583.

[232] Asaad, M.; Buckman, J.; Smith, R. I.; Bos, J. W. G. Thermoelectric properties and high-temperature stability of the Ti 1- x V x CoSb 1- x Sn x half-Heusler alloys. *RSC Adv.* **2016** *6(61)*, 56511–56517.

[233] Hichour, M.; Rached, D.; Khenata, R.; Rabah, M.; Merabet, M.; Reshak, A. H. *et al.* Theoretical investigations of NiTiSn and CoVSn compounds. *J. Phys. Chem. Solids* **2012** *73(8)*, 975–981.

[234] Shi, H.; Ming, W.; Parker, D. S.; Du, M. H.; Singh, D. J. Prospective high thermoelectric performance of the heavily p-doped half-Heusler compound CoVSn. *Phys. Rev. B* **2017** *95(19)*, 195207.

[235] Hooshmand Zaferani, S.; Darebaghi, A.; Hong, S. J.; Vashaee, D.; Ghomashchi, R. Experimental realization of heavily p-doped half-Heusler CoVSn compound. *Energies*]bf 2020 *13(6)*, 1459.

[236] Abir, B.; Ahmoum, H.; Khamkhami, J. E.; Li, G.; Bardouni, T. E.; El Harouny, E. L.; Achahbar, A. First-principles study of the structural, electronic, optical, and thermoelectric properties of the RhVZ (Z= Si, Ge, Sn). *Micro Nano Struct.* **2022** *164*, 107162.

[237] Adebambo, P. O.; Agbaoye, R. O.; Bamgbose, M. K.; Ayedun, F.; Solola, G. T.; Adebayo, G. A. Assessing the structural, electronic, elastic and thermoelectric properties of PtTiSn and PdLaBi transition metal alloys from the first-principles prospective. *Mater. Sci. Semicond.* **2021** *129*, 105796.

[238] Tranås, R.; Løvvik, O. M.; Berland, K. Attaining Low Lattice Thermal Conductivity in Half-Heusler Sublattice Solid Solutions: Which Substitution Site Is Most Effective?. *Electron. Mater.* **2022** *3(1)*, 1–14.

[239] Lee, A.; Sarker, S.; Saal, J. E.; Ward, L.; Borg, C.; Mehta, A.; Wolverton, C. Machine learned synthesizability predictions aided by density functional theory. *Commun. Mater.* **2022** *3(1)*, 73.

[240] Gzyl, A. S.; Oliynyk, A. O.; Mar, A. Half-heusler structures with full-heusler counterparts: machine-learning predictions and experimental validation. *Cryst. Growth Des.* **2020** *20(10)*, 6469–6477.

[241] Eilers, F.; Grube, K.; Zocco, D. A.; Wolf, T.; Merz, M., Schweiss, P. *et al.* Quantum criticality in AFe2As2 with A= K, Rb, and Cs suppresses superconductivity. *arXiv preprint arXiv:1510.01857* **2015**.

[242] Huang, Y.; Hayashi, K.; Miyazaki, Y. Electron conduction mechanism of deficient half-Heusler VFeSb compound revealed by crystal and electronic structure analyses. *Chem. Mater.* **2020** *32(12)*, 5173–5181.

[243] El-Khouly, A.; Adam, A. M.; Novitskii, A.; Ibrahim, E. M. M.; Serhiienko, I.; Nafady, A. *et al.* Effects of spark plasma sintering on enhancing the thermoelectric performance of Hf–Ti doped VFeSb half-Heusler alloys. *J. Phys. Chem. Solids* **2021** *150*, 109848.

[244] Mostari, F.; Rahman, M. A.; Khatun, R. First principles study on the structural, elastic, electronic and optical properties of cubic half-Heusler alloy RuVAs under pressure. *Int. J. Mat. Math. Sci* **2020** *2(4)*, 51–63.

[245] Sharma, S. K.; Ahmed, S. S. Transport properties of RuV-based half-Heusler semiconductors for thermoelectric applications: a computational study. *J. Phys. Condens. Mat.* **2020** *32(40)*, 405501.

[246] Chibani, S.; Arbouche, O.; Zemouli, M.; Benallou, Y.; Amara, K.; Chami, N. *et al.* First-principles investigation of structural, mechanical, electronic, and thermoelectric properties of Half-Heusler compounds RuVX (X= As, P, and Sb). *Comput. Condens. Matter* **16**, e00312.

[247] Bencherif, K.; Yakoubi, A.; Della, N.; Miloud Abid, O.; Khachai, H.; Ahmed, R.; *et al.* First principles investigation of the elastic, optoelectronic and thermal properties of XRuSb:(X= V, Nb, Ta) semi-Heusler compounds using the mBJ exchange potential. *J. Electron. Mater.* **2016** *45*, 3479–3490.

[248] Mohan, L.; Sukhender, S.; Kumar, S.; Bhardwaj, S. R.; Verma, A. S. Structural, Electronic, Mechanical and Thermal Properties of CoVZ (Z= Si, Ge, Sn, Pb) half-Heusler Compounds. *East Eur. J. Phys.* **2020** *(4)*, 42–50.

[249] Hu, Y.; Wan, R.; Zhang, Z.; Guo, Z.; Tian, G. Predicting the thermoelectric performance of p-type VFeBi based on scattering mechanisms. *J. Electron. Mater.* **2023** *52(2)*, 980–988.

[250] Sarwan, M.; Shukoor, A.; Singh, S. A first principle study of structural, elastic, electronic and thermodynamic properties of Half-Heusler compounds; YNiPn (Pn= As, sb, and bi). *Solid State Sci.* **2021** *112*, 106507.

[251] Romaka, V. V.; Romaka, L.; Horyn, A.; Stadnyk, Y. Experimental and theoretical investigation of the Y–Ni–Sb and Tm–Ni–Sb systems. *J. Alloys Compd.* **2021** *855(1)*, 157334.

[252] Sharma, S.; Kumar, P. Tuning the thermoelectric properties of YNiBi half-Heusler alloy. *MRX* **2018** *5(4)*, 046528.

[253] Sharma, S.; Kumar, P. Understanding the transport properties of YNiBi half-Heusler alloy: An Ab-initio study. *AIP Conf. Proc* **2017** *1832*, 110048.

[254] Bende, D.; Grin, Y.; Wagner, F. R. Covalence and Ionicity in MgAgAs-Type Compounds. *Chem. Eur. J.* **2014** *20(31)*, 9702–9708.

[255] Gofryk, K.; Kaczorowski, D.; Plackowski, T.; Mucha, J.; Leithe-Jasper, A.; Schnelle, W.; Grin, Y. Magnetic, transport, and thermal properties of the half-Heusler compounds ErPdSb and YPdSb. *Phys. Rev. B* **2007** *75(22)*, 224426.

[256] Gnida, D.; Ciesielski, K.; Kaczorowski, D. Origin of the negative temperature coefficient of resistivity in the half-Heusler antimonides LuNiSb and YPdSb. *Phys. Rev. B* **2021** *103(17)*, 174206.

[257] Kumar, R.; Luo, S. S.; Du, F.; Su, H.; Zhang, J.; Cao, C.; Yuan, H. Q. Superconductivity in non-centrosymmetric ZrNiAl and HfRhSn-type compounds. *J. Phys.: Condens. Matter* **2022** *34(43)*, 435701.

[258] Saurabh, K.; Kumar, A.; Ghosh, P.; Singh, S. Low thermal conductivity and semimetallic behavior in some TiNiSi structure-type compounds. *Phys. Rev. Mater.* **2021** *5(8)*, 085406.

[259] Raghuvanshi, P. R.; Mondal, S.; Bhattacharya, A. A high throughput search for efficient thermoelectric half-Heusler compounds. *J. Mater. Chem. A* **2020** *8(47)*, 25187–25197.

[260] Hohl, H.; Ramirez, A. P.; Goldmann, C.; Ernst, G.; Wölfing, B.; Bucher, E. Efficient dopants for ZrNiSn-based thermoelectric materials. *J. Phys. Condens.* **1999** *11(7)*, 1697.

[261] Shen, Q.; Chen, L.; Goto, T.; Hirai, T.; Yang, J.; Meisner, G. P.; Uher, C. Effects of partial substitution of Ni by Pd on the thermoelectric properties of ZrNiSn-based half-Heusler compounds. *Appl. Phys. Lett.* **2001** *79(25)*, 4165–4167.

[262] Xie, H.; Wang, H.; Fu, C.; Liu, Y.; Snyder, G. J.; Zhao, X.; Zhu, T. The intrinsic disorder related alloy scattering in ZrNiSn half-Heusler thermoelectric materials. *Sci. Rep.* **2014** *4(1)*, 6888.

[263] Yang, J.; Meisner, G. P.; Chen, L. Strain field fluctuation effects on lattice thermal conductivity of ZrNiSn-based thermoelectric compounds. *Appl. Phys. Lett.* **2004** *85(7)*, 1140–1142.

[264] Huang, X. Y.; Xu, Z.; Chen, L. D. The thermoelectric performance of ZrNiSn/ZrO2 composites. *Solid State Sci.* **2004** *130(3-4)*, 181–185.

[265] Fiedler, G.; Kratzer, P. Ternary semiconductors NiZrSn and CoZrBi with half-Heusler structure: A first-principles study. *Phys. Rev. B* **2016** *94(7)*, 075203.

[266] Kawaharada, Y.; Uneda, H.; Muta, H.; Kurosaki, K.; Yamanaka, S. High temperature thermoelectric properties of NiZrSn half-Heusler compounds. *J. Alloys Compd.* **2004** *364(1-2)*, 59–63.

[267] Yousuf, S.; Bhat, T. M.; Singh, S.; Saleem, Z.; Mir, S. A.; Khandy, S. A. *et al.* Applicability of semi-classical Boltzmann transport theory in understanding the thermoelectric properties of ZrNiSn and ZrNiPb half-heuslers. *AIP Conf. Proc* **2019** *2115*, 030420.

[268] Mao, J.; Zhou, J.; Zhu, H.; Liu, Z.; Zhang, H.; He, R. *et al.* Thermoelectric properties of n-type ZrNiPb-based half-Heuslers. *Chem. Mater.* **2017** *29(2)*, 867–872.

[269] Rahnamaye Aliabad, H. A.; Nodehi, Z.; Maleki, B.; Abareshi, A. Electronical and thermoelectric properties of half-Heusler ZrNiPb under pressure in bulk and nanosheet structures for energy conversion. *Rare Met.* **2019** *38*, 1015–1023.

[270] Bhardwaj, A.; Jat, K. S.; Sagar, A. D.; Khovalyo, V. V.; Patnaik, S. Reduction in thermal conductivity of n-type ZrNiPb-based half–Heusler compounds via compositional engineering approach. *AIP Conf. Proc* **2019** *2115*, 030584.

[271] Jiang, Q.; Wan, R.; Zhang, Z.; Lei, Y.; Tian, G. High thermoelectric performance of half-Heusler ZrXPb (X= Ni, Pd, and Pt) compounds from first principle calculation. *J. Phys. Condens. Matter.* **2021** *33(46)*, 465501.

[272] Johnson, V.; Jeitschko, W. Ternary equiatomic transition metal silicides and germanides. *J. Solid State Chem.* **1972** *4(1)*, 123–130.

[273] Anissa, B.; Radouan, D.; Benaouda, B.; Omar, A. First-principles study of structural, electronic, thermodynamic, and thermoelectric properties of a new ternary half-Heusler alloy PdZrGe. *Chinese J. Phys.* **2018** *56(6)*, 2926–2936.

[274] Balmumcu, F. I.; Özdemir, E. G.; Merdan, Z. Structural, half-metallic, electronic, magnetic and pressure-induced elastic changes of PdVSi, PdVGe, PdVSn, and PdVSb alloys. *J. Mater. Sci.* **2023** *58(12)*, 5349–5361.

[275] Jeitschko, W. Transition metal stannides with MgAgAs and MnCu 2 Al type structure. *Metall. Mater. Trans.* **1970** *1*, 3159–3162.

[276] Ackerbauer, S. V.; Gumeniuk, R.; Prots, Y.; Borrmann, H.; Weitzer, F.; Leithe-Jasper, A. Crystal structures of zirconium-platinum-silicon (1: 1: 1), ZrPtSi, zirconium-platinum-germanium (1: 1: 1), ZrPtGe and titanium-platinum-silicon (1: 1: 1), TiPtSi. *ZKNSFT* **2010** *225(1)*, 7–9.

[277] Dai, C. K.; Song, Q. F.; Xie, L.; Liu, R. H.; Bai, S. Q.; Chen, L. D. Improving thermoelectric properties of ZrPtSn-based half-Heusler compound by Sb doping. *Rare Met.* **2021** *40(10)*, 2838–2846.

[278] Khandy, S. A.; Kaur, K.; Dhiman, S.; Singh, J.; Kumar, V. Exploring thermoelectric properties and stability of half-Heusler PtXSn (X= Zr, Hf) semiconductors: a first principle investigation. *Comput. Mater. Sci.* **2021** *188*, 110232.

[279] Yin, M.; Nash, P. Standard enthalpies of formation of selected XYZ half-Heusler compounds. *J. Chem. Thermodyn.* **2015** *91*, 1–7.

[280] Roy, A.; Bennett, J. W.; Rabe, K. M.; Vanderbilt, D. Half-Heusler semiconductors as piezoelectrics. *Phys. Rev. Lett.* **2012** *109(3)*, 037602.

[281] Kenjo, S.; Ogino, Y.; Mukai, K.; Bakr, M.; Yagi, J.; Konishi, S. Employing of ZrCo as a fuel source in a discharge-type fusion neutron source operated in self-sufficient mode. *Int. J. Hydrog. Energy.* **2022** *47(5)*, 3054–3062.

[282] Agosta, D. S.; Hightower, J. E.; Foster, K.; Leisure, R. G.; Gavra, Z. Elastic moduli of polycrystalline ZrCo as a function of temperature. *J. Alloys Compd.* **2002** *346(1-2)*, 1–5.

[283] Chauhan, N. S.; Bathula, S.; Vishwakarma, A.; Bhardwaj, R.; Johari, K. K.; Gahtori, B.; Dhar, A. Enhanced thermoelectric performance in p-type ZrCoSb based half-Heusler alloys employing nanostructuring and compositional modulation. *J. Materiomics* **2019** *5(1)*, 94–102.

[284] Yuan, B.; Wang, B.; Huang, L.; Lei, X.; Zhao, L.; Wang, C.; Zhang, Q. Effects of Sb substitution by Sn on the thermoelectric properties of ZrCoSb. *J. Electron. Mater.* **2017** *46*, 3076–3082.

[285] Chauhan, N. S.; Bhardwaj, A.; Senguttuvan, T. D.; Pant, R. P.; Mallik, R. C.; Misra, D. K. A synergistic combination of atomic scale structural engineering and panoscopic approach in p-type ZrCoSb-based half-Heusler thermoelectric materials for achieving high ZT. *J. Mater. Chem. C* **2016** *4(24)*, 5766–5778.

[286] Ibrahim, N.; Ahmed, R. A.; Adri, H.; Reisya, I. Electronic structures and thermoelectric properties of heavily doped n-type ZrCoBi from first principles calculations. *Mater. Today Commun.* **2022** *32*, 103908.

[287] Radouan, D.; Anissa, B.; Benaouda, B. Investigation on electronic and thermoelectric properties of (P, As, Sb) doped ZrCoBi. *East Eur. J. Phys.* **2021** *1*, 27–33.

[288] Khandy, S. A.; Chai, J. D. Strain engineering of electronic structure, phonon, and thermoelectric properties of p-type half-Heusler semiconductor. *J. Alloys Compd.* **2021** *850*, 156615.

[289] Tobola, J.; Jodin, L.; Pecheur, P.; Venturini, G. Unusual electron structure and electron transport properties of some disordered half-Heusler phases. *J. Alloys Compd.* **2004** *383(1-2)*, 328–333.

[290] Dey, A.; Sharma, R.; Dar, S. A. An extensive investigation of structural, electronic, thermoelectric and optical properties of bi-based half-Huesler alloys by first principles calculations. *Mater. Today Commun.* **2020** *25*, 101647.

[291] Yazdani-Kachoei, M.; Jalali-Asadabadi, S. Topological analysis of electron density in half-Heusler ZrXBi (X= Co, Rh) compounds: A density functional theory study accompanied by Bader's quantum theory of atoms in molecules. *J. Alloys Compd.* **2020** *828*, 154287.

[292] Zhang M.; Wei, J.; Wang, G. Thermoelectric and topological properties of half-Heusler compounds ZrIrX (As, Sb, Bi). *Phys. Lett. A* **2018** *382(9)*, 673–678.

[293] Seidov, F. M.; Kerimova, E. M.; Mustafaeva, S. N.; Veliev, R. K.; Magerramov, A. B. Investigation of TITe-FeTe system and electrical properties of TIFeTe sub 2; Issledovanie sistemy TITe-FeTe i elektricheskie svoystva TiFeTe *Fizika (Baku)* **2000** *6*.

[294] Granovsky, M. S.; Arias, D. Intermetallic phases in the iron-rich region of the ZrFe phase diagram. *J. Nucl. Mater.* **1996** *229*, 29–35.

[295] Keshri, S. P.; Medhi, A. Intrinsically high thermoelectric figure of merit of half-Heusler ZrRuTe. *J. Condens. Matter Phys.* **2020** *32(42)*, 425701.

[296] Abdon, R. L.; Hughbanks, T. Stabilization of Metal-Rich Compounds by Polar-Intermetallic Bonding. Synthesis, Structure, and Bonding in Hf5MTe3 (M= Fe, Co). *J. Am. Chem. Soc.* **1999** *117(40)*, 10035–10040.